Post-tensioned Timber Frame Structures

Report

Author(s):
Wanninger, Flavio

Publication date:
2015-11

Permanent link:
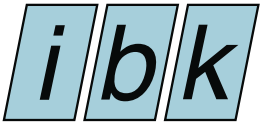https://doi.org/10.3929/ethz-a-010563008

Rights / license:
In Copyright - Non-Commercial Use Permitted

Originally published in:
IBK Bericht 364

ibk

Institut für Baustatik und Konstruktion, ETH Zürich

Post-tensioned timber frame structures

Flavio Wanninger

POST-TENSIONED TIMBER FRAME STRUCTURES

Flavio Wanninger

Institute of Structural Engineering

ETH Zurich

Zurich

November 2015

Foreword

In the past decades, precast concrete frames were developed using tendons to connect columns and beams. These systems showed favourable seismic behaviour, being able to avoid residual deformations after an earthquake. A similar low-damage rocking system for timber was developed in New Zealand at the University of Canterbury. The rocking timber system has been named Pres-Lam and it covers both seismic resistant frames and walls. The use of post-tensioned timber structures has been studied at the Institute of Structural Engineering at the ETH in Zurich in the frame of a research project in cooperation with the industrial partner Häring & Co. AG. As a result, an innovative post-tensioned timber frame was developed using glued laminated timber made of spruce and local strengthening of the beam-column timber joint with hardwood (ash). The developed post-tensioned timber frame with hardwood has successfully been implemented in the ETH House of Natural Resources (www.honr.ethz.ch), a research and demonstration office building for sustainable construction using hardwood.

The present research report was written as a PhD thesis (ETH Dissertation Nr. 22815) by Flavio Wanninger and shows the results of a comprehensive experimental and numerical analysis on the structural behaviour of post-tensioned timber frame, in particular with focus on the moment-rotation-behaviour of the developed post-tensioned beam-column timber joint using hardwood and the long-term behaviour of the system. The results of the experimental and numerical investigations provide reliable data for the development and validation of calculation models for the design of post-tensioned timber frames with hardwood for vertical and horizontal loads and taking into account the long-term behaviour. The objective of the research project is the development and implementation of post-tensioned timber frame structures into the practice and fits well into the overall research strategy of the institute on the development of innovative solutions for timber structures.

I would like to thank Flavio Wanninger for his careful experimental and theoretical contribution and personal high commitment in the development of fundamental data and design models for post-tensioned timber frames with hardwood and in the implementation of the developed technology in the ETH House of Natural Resources. Further, I would like to gratefully acknowledge the support by the industrial partner Häring & Co. AG, the Swiss Commission for Technology and Innovation (CTI) and the Climate-KIC's Building Technologies Accelerator programme.

Zurich, October 2015

Andrea Frangi

Abstract

Simple and economical moment-resisting connections are difficult to realize in timber engineering. These kinds of connections are often built using steel elements and are therefore expensive. A solution may be provided with post-tensioned timber joints. A research program was launched in 2004 at the University of Canterbury, New Zealand, with the aim to adapt post-tensioned connections for timber. Post-tensioned timber joints have also been studied at the Institute of Structural Engineering at the ETH in Zurich. An innovative post-tensioned beam-column timber joint has been developed using glued laminated timber with local hardwood reinforcement. No further steel elements are required for the moment-resisting timber joint, only a single straight tendon is placed in a cavity in the middle of the beam. The developed joint is characterised by a high degree of pre-fabrication and easy assembly on site. The system shows great potential for timber frame structures and multi-storey buildings. This thesis investigates the structural behaviour of the post-tensioned timber connection that was developed at the ETH in Zurich.

Robust design criteria and analytical models are fundamental for a successful market implementation of the proposed system. A simplified analytical model was developed in order to predict the structural behaviour of the post-tensioned timber connection. The model is based solely on the stiffness properties of the column and the geometrical properties of the joint. The model predictions are in good agreement with the experimental results for tendon forces over 500 kN or initial compression stresses corresponding to 2 MPa. In case of lower tendon forces, however, the model predicts a too stiff behaviour.

The moment-rotation-behaviour of a post-tensioned beam-column timber joint was analysed extensively with a series of static bending tests. The timber joint was loaded at the end of the beams in order to apply a moment to the connection. The tests were conducted with various tendon forces, from 300 kN up to 700 kN. The bending tests were performed with a controlled load level so that no failure perpendicular to the grain in the column occurred. The maximal allowable vertical load to be applied was estimated using the analytical model. A final bending test was conducted in order to study the failure mode of the post-tensioned timber joint. The vertical load on the beams was increased until the tendon elongation got so high that the test had to be aborted for safety reasons. The tests showed a self-centering behaviour of the proposed joint which was able to withstand all applied load cases without any severe damage.

A post-tensioned timber frame was analysed with a series of pushover-tests. The frame was loaded horizontally while the displacement was recorded. The tests were conducted with various tendon forces, from 300 kN up to 700 kN to determine the influence of the tendon force on the horizontal stiffness of the frame. All tests were performed with a controlled load level, which was estimated using the analytical model. The frame showed a self-centering behaviour without any noticeable damage. The pushover-curves were in the expected range of the model predictions. Moreover, the analytical model was able to predict the structural behaviour of

the connections accurately. This could be verified by analysing the position of several LEDs attached to the connections.

A numerical model using OpenSees was developed in order to obtain a second tool to predict the structural behaviour of the proposed system. The model could verify the results obtained from the analytical approach and is therefore able to predict the behaviour of post-tensioned timber connections well. In addition to the analytical model, the OpenSees model shows a reduction in stiffness as the tendon force gets smaller, i.e. the numerical model can also be used for low tendon forces. However, the numerical model requires more input parameters than the analytical model which may be difficult to estimate accurately. Nevertheless, the numerical model provides a second independent tool which can be used for the design of post-tensioned timber structures.

Tests regarding the long-term behaviour of post-tensioned timber connections have been performed for the duration of two years up to date and will continue for at least one more year. The aim of these tests is to estimate the loss in tendon force that has to be expected during the life-time of a structure. Several post-tensioned beam and beam-column timber specimens exposed to controlled and uncontrolled environmental conditions and loaded only with the axial prestressing force have been monitored. The force in the tendon is measured together with the strains in the specimens as well as the temperature and relative humidity in the testing environment. The tests showed that the specimens in the uncontrolled environment suffered more losses than the ones in the controlled environment. The additional losses are due to mechano-sorptive strains, which occur in loaded specimens in combination with a change in moisture content. Furthermore, creep tests were performed on small glulam timber blocks loaded in compression. The estimated creep coefficients parallel and perpendicular to the grain are used to calculate the tendon force losses with an analytical model for the larger post-tensioned specimens. The model is also used to estimate the benefit of reinforcing the column with hardwood in the connection region. Based on the model predictions and the extrapolated tendon force losses of the post-tensioned specimens a 30% loss in tendon force should be accounted for in the design process.

The moment-rotation behaviour of the post-tensioned timber connection was implemented in an OpenSees model using a tri-linear rotational spring in order to design a post-tensioned timber structure. The design process showed that neither the gravity loads nor the seismic load are the controlling design criteria. The design is rather controlled by the lateral deformations due to wind. Based on this finding it is recommended to focus further research in increasing the connection stiffness or add additional structural elements before continuing with investigations on the seismic design.

Kurzfassung

Die Umsetzung von wirtschaftlich biegesteifen Verbindungen ist im Holzbau schwer zu realisieren. Diese Art von Verbindungen benötigen oft Stahlelemente und sind daher teuer. Ein Lösungsansatz kann die Verwendung von vorgespannten Holzverbindungen sein. Ein Forschungsprogramm wurde im Jahr 2004 an der Universität von Canterbury gestartet, um die Entwicklung von duktilen vorgespannten Verbindungen für Holztragwerke voranzutreiben. Diese vorgespannten Holzrahmen können auf der Baustelle schnell montiert werden und sind daher auch aus wirtschaftlicher Sicht interessant. Am Institut für Baustatik und Konstruktion der ETH Zürich wurde in Zusammenarbeit mit der Firma Häring & Co. AG der Prototyp einer neuartigen vorgespannten Holzrahmenkonstruktion entwickelt. Diese Arbeit befasst sich mit dem an der ETH entwickelten System.

Für eine erfolgreiche Markteinführung des vorgeschlagenen Systems benötig es Bemessungsgrundlagen, welche von Ingenieuren in der Praxis angewendet werden können. Ein einfaches Berechnungsmodell wurde entwickelt, um das Tragverhalten der vorgespannten Holzverbindung vorherzusagen. Das Modell basiert auf Federn und benötigt lediglich die Steifigkeitseigenschaften der Stütze sowie die geometrischen Eigenschaften des Anschlusses als Eingabeparameter. Die Modellvorhersagen stimmen gut mit den experimentellen Ergebnissen überein, allerding lediglich für Vorspannkräfte über 500 kN, was einer initialen Druckspannung von 2 MPa entspricht. Das Modell überschätzt die Steifigkeiten des Anschlusses bei kleineren Vorspannkräften.

Das Momenten-Rotationsverhalten eines vorgespannten Knotens wurde ausgiebig mit einer Reihe von statischen Versuchen analysiert. Die Trägerenden wurden vertikal belastet um ein Moment in der Verbindung zu erzeugen. Die Versuche wurden unter verschiedenen Vorspannkräften von 300 kN bis zu 700 kN durchgeführt. Die Biegeversuche wurden unter einem kontrollierten Lastniveau durchgeführt, so dass kein Versagen im Knotenbereich eintreten konnte. Die maximal zulässige Last wurde mit dem analytischen Modell berechnet. Ein letzter Belastungsversuch wurde durchgeführt, um ein Versagen des vorgespannten Knotens herbeizuführen. Die vertikale Belastung wurde erhöht, bis der Zuwachs in der Vorspannkraft so hoch wurde, dass der Versuch aus Sicherheitsüberlegungen abgebrochen werden musste. Die Versuche zeigten ein selbstzentrierendes Verhalten des Knoten, welcher sämtliche Lastfälle ohne nennenswerte Schäden überstand.

Weitere Versuche wurden an einem vorgespannten Rahmen vorgenommen, welcher horizontal belastet wurde (Pushover-Versuche). Die Versuche wurden ebenfalls mit verschiedenen Vorspannkräften von 300 kN bis zu 700 kN durchgeführt, um zu prüfen, wie die Vorspannkraft die horizontale Steifigkeit des Rahmens beeinflusst. Alle Versuche wurden mit einem kontrollierten Belastungsniveau durchgeführt, welches unter Verwendung des analytischen Modells berechnet wurde. Der Rahmen zeigte ein selbstzentrierendes Verhalten ohne grosse Schäden bei dem kontrollierten Lastniveau. Das Verhalten des Rahmens konnte gut mit dem analytischen Modell

vorgehrgesagt werden. Darüber hinaus war das analytische Modell in der Lage, das strukturelle Verhalten der Anschlüsse vorherzusagen, welches durch die Analyse der Position mehrerer LEDs an den einzelnen Anschlüssen verifiziert werden konnte.

Ein numerisches Modell wurde entwickelt um eine zweite unabhängige Alternative für die Vorhersage des strukturellen Verhaltens von vorgespannten Knoten zur Verfügung zu stellen. Dieses numerische Modell konnte mit den experimentellen Ergebnissen verifiziert werden und stimmt daher auch mit dem analytischen Modell weitgehend überein. Zudem ist das numerische Modell, im Gegensatz zum analytischen Modell, in der Lage, das Knotenverhalten bei niedrigen Vorspannkräften vorherzusagen. Es benötigt jedoch mehr Eingabeparameter als beim analytischen Ansatz, wie beispielsweise die Querdehnzahlen, dessen korrekte Ermittlung schwierig ist. Dennoch stellt das numerische Modell ein zweites Bemessungswerkzeug dar, welches für die Modellierung von vorgespannten Holzrahmen verwendet werden kann.

Um die Spannkraftverluste für Holzrahmenkonstruktionen zu schätzen, wurden Versuche an vorgespannten Verbindungen und Trägern durchgeführt. Die Versuche liefen bis dato für zwei Jahre und werden noch für mindestens ein Jahr fortgeführt. Mehrere vorgespannte Träger und Knoten wurden in kontrollierten und unkontrollierten Umweltbedingungen geprüft, wobei die Vorspannkraft kontinuierlich gemessen wurde. Die Versuche zeigten, dass die Körper in den unkontrollierten Bedingungen grössere Spannkraftverluste aufweisen als die Körper in den kontrollierten Bedingungen. Der Unterschied konnte mit dem Auftreten von mechano-sorptiven Dehnungen erklärt werden, welche bei belasteten Proben auftreten, welche gleichzeitig eine Feuchteänderung erfahren. Parallel wurden Kriechversuche an kleinen BSH-Elementen durchgeführt um die Kriechzahlen zu bestimmen. Diese wurden für ein analytisches Modell verwendet um die Spannkraftverluste zu berechnen. Auf der Grundlage der Modellvorhersagen und den extrapolierten Verlusten der vorgespannten Proben sollten 30% Spannkraftverlust für die Bemessung berücksichtigt werden.

Das mit dem analytischen Modell ermittelte Momenten-Rotationsverhalten des Anschlusses wurde in ein OpenSees-Modell implementiert. Dazu wurde der Anschluss mit einer tri-linearen Rotationsfeder modelliert. Dieses Modell wurde für die überschlägige Bemessung eines fiktiven Gebäudes verwendet. Diese Bemessung zeigt, dass weder die Schwerlasten noch die Erdbebenlasten massgebend sind, sondern die horizontalen Verformungen unter Windbeanspruchung. Zukünftige Forschungsvorhaben sollten sich daher auf die Aussteifung des Systems konzentrieren bevor das Verhalten unter Erdbeben genauer untersucht wird.

Contents

Chapter 1

Introduction

1.1 A simple beam to column connection as motivation

Timber buildings are often smaller constructions compared to buildings made of concrete or steel. Moreover, design codes often limit the height of timber buildings in several countries due to reasons concerning fire safety [1]–[3].

The growing concern regarding global warming and the drastically increasing amount of CO_2-emissions [4] requires methods to reduce the global emission of greenhouse gases while increasing the storage capacity for carbon dioxide. Timber buildings can fulfil both requirements since they can be constructed using less energy compared to buildings made of concrete [5] and also act as a storage for carbon dioxide.

More timber buildings should therefore be constructed, rather than buildings using concrete or steel as main construction material. In order to compete with structures made of concrete or steel, timber structures have to be safe, economical, quickly assembled and flexible. Timber frame structures can fulfil the mentioned requirements. A main disadvantage are the complicated connections between beams and columns, which are often bolted and reinforced with screws. These connections are able to resist a bending moment [6]. However, the beams are often designed as simply supported and the bending moments are neglected [7].

A system that has been developed in New Zealand at the University of Canterbury is suitable for timber frames. The system uses the post-tensioning technique to provide for moment resistance and quick assembly [8].

The system developed in New Zealand has been adapted at ETH Zurich to fit the European market [9]. The result is the post-tensioned timber connection as shown in Figures 1.1(a) and 1.1(b).

<center>(a)   (b)</center>
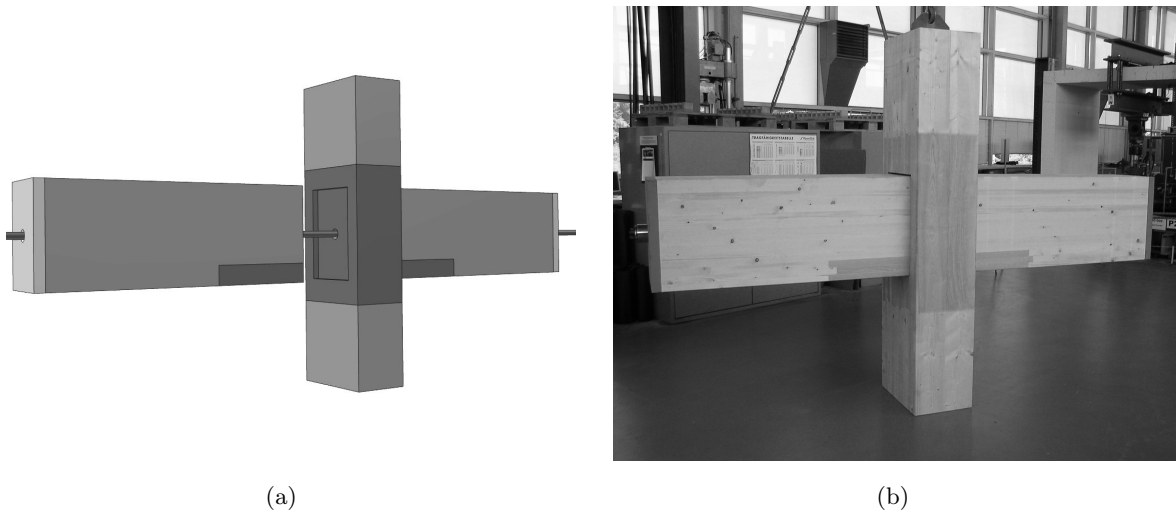
Figure 1.1: 1.1(a): Visualisation of the post-tensioned timber connection developed at ETH Zurich 1.1(b): Picture of the actual post-tensioned timber specimen [9]

1.2 Research objective and thesis outline

This thesis investigates the structural behaviour of the post-tensioned timber connection that was developed at ETH Zurich. Within this research project, several tests and analytical as well as numerical investigations were conducted. The following list gives an overview of the work described within this thesis:

1. Development of a simple analytical model

2. Tests on a post-tensioned timber connection under gravity loads

3. Tests on a post-tensioned timber frame under horizontal loads

4. Verification of the analytical model with a finite element model

5. Estimation of the long-term losses in tendon force

6. Design of a post-tensioned timber structure

7. Conclusions and outlook for further research

A short literature review can be found in Chapter 2. The literature review focuses on earlier attempts to prestress timber and shows how the post-tensioned timber connections were adapted from the concrete industry. The chapter ends with an overview of the first buildings constructed with post-tensioned timber frames with a load-bearing function.

Chapter 3 introduces an analytical model which is based on springs and therefore easily accessible for practicing engineers. The model parameters are introduced and all equations are derived within this chapter. The model can be used for gravity loads or horizontal loads. The model showed good predictions for the moment-rotation behaviour in the connection area. Moreover,

the model allows estimating the position of the neutral axis, takes the tendon elongation into account and is able to calculate the stresses based on linear-elastic analysis. The only input parameter needed for the model is the modulus of subgrade reaction (spring constant). It is suggested to calculate the modulus of subgrade reaction solely as a function of the Young's modulus perpendicular to the grain of the column and the geometrical properties of the joint. This recommendation is based on the assumption that the column is much softer than the beam so that the latter can be modelled as a rigid body.

The first extensive test series was conducted on a post-tensioned timber connection, i.e. two beams and a column. The specimen was loaded under gravity loads with different tendon forces. An overview of the tests, conclusions and comparison with the analytical approach can be found in Chapter 4.

The tests on a post-tensioned frame specimen are described in Chapter 5. An identical frame was used to build the "ETH House of Natural Resources". The frame was tested in the lab under horizontal loading. The pushover-curve for the tests was recorded and compared to the analytical solution.

A numerical model is introduced in Chapter 6. The model can be used to simulate the conducted tests but also to check the accuracy of the analytical approach. Furthermore, the model can be used for future efforts (e.g. modifications of the connection).

Tests regarding the long-term behaviour of post-tensioned timber frames have been ongoing at ETH since 2012. The aim of this experimental campaign is to estimate the loss in tendon force for the proposed post-tensioned timber connection. The most important conclusions and the extrapolated losses will be discussed in Chapter 7.

Chapter 8 gives a short introduction on the design of a post-tensioned timber structure. A building which is similar to the "ETH House of Natural Resources" will be designed for gravity and horizontal loads.

The last two chapters include a summary of the research's most important findings and an outlook for further work on the subject.

Chapter 2

State of the art

2.1 Early attempts of prestressing timber

Several studies have analysed the effects of applying a prestressing force on timber beams. Lantos [10] used a monowire cable for prestressing with the aim to reinforce low-grade wood. The result was fewer variable failure loads with only a modest increase in strength. Peterson [11] attempted to increase strength and stiffness by using a prestressed high-strength steel strip bonded to the beam tensile surface, with moderate success. Reinforcing glulam beams with bonded prestressed FRP laminates in the tension zone has recently been proposed as a mean of utilizing low-quality timber by improving its structural performance [12]–[14].

Stress-laminated deck plates are typically used in bridge decks. A prestressing force is applied perpendicular to the grain and increases the shear friction between the individual pieces of timber [15]. Several applications can be found in literature published since the 1980s [16], [17]. More recently, a prestressed LVL-concrete composite beam was constructed and tested by Deam et al. [18]. The prestressing tendons had little effect on stiffness or strength, but they did reduce the deflection from the permanent load, particularly when the tendons were draped.

2.2 The PRESSS - System

The origin of connecting prefabricated elements with an unbonded tendon can be found in concrete structures. In the past decades precast concrete frames were developed using tendons to connect columns and beams [19]–[21] within the framework of a program to investigate the performance of precast concrete buildings called the "Precast Seismic Structural Systems Research Program" (PRESSS). Different connection types were used and tested for the developed precast concrete frames. One of these connections was realised with unbonded tendons. This system showed favourable seismic behaviour, being able to avoid residual deformations and experience only minor damage after an earthquake.

These precast concrete connections can be designed using a procedure that is called the "monolithic beam analogy" [22], [23].
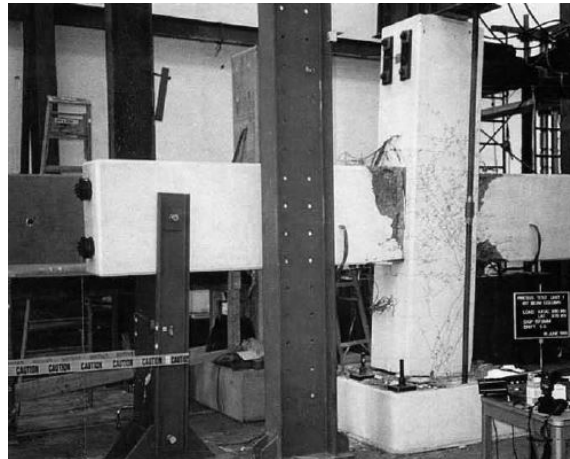
Figure 2.1: Post-tensioned beam-column connection made of precast concrete elements [20]

2.3 Post-tensioned timber structures using unbonded tendons

2.3.1 Pres-Lam®

A system for post-tensioned timber connections was introduced in New Zealand at the University of Canterbury, which is an adoption of the PRESSS-system for timber constructions. The developed system - called Pres-Lam® - uses laminated veneer lumber (LVL) as an alternative to concrete [24] for post-tensioned frame and wall structures. Preliminary tests on a post-tensioned beam-column joint showed a favourable seismic behaviour. Energy dissipation is easily possible by adding dissipators or by yielding of mild steel within the specimen as indicated in Figure 2.2, making the system suitable for areas with high seismic activity.
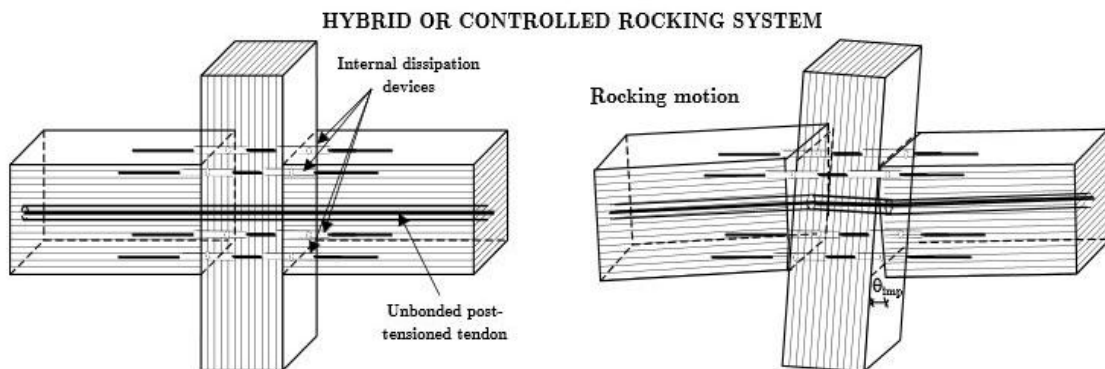
Figure 2.2: Drawing of a post-tensioned beam-column connection with internal dissipators made of LVL, developed at the University of Canterbury [24]

Based on these preliminary tests and their promising results, further experiments were performed [25]. A post-tensioned beam-column connection as well as a post-tensioned wall to foundation connection were tested under horizontal loading. The Pres-Lam® system showed no damage in the elements, a flag-shaped hysteresis curve and negligible residual deformations in the system

after the tests. The results from these experiments indicated a good seismic performance of the proposed system made with LVL [26].

Further work concentrated on the behaviour of post-tensioned beam-column connections. A simplified analytical model for the section analysis was introduced [27] which is based on the "monolithic beam analogy". A design framework was published, dealing with the local connection behaviour as well as the global frame response under seismic loading [28].

More tests were performed on beam-column specimens [29] and on the frame of a building scaled to 2/3 of its actual size (Figure 2.3) [30], which was later constructed with post-tensioned timber walls [31].

Figure 2.3: Tests performed on a scaled post-tensioned timber frame building [30]

Additional testing referred to the connection stiffness [32], advanced damping systems [33] and the benefit of the proposed system regarding costs and construction time [34].

During the development of the post-tensioned timber frames in New Zealand, code provisions [35] as well as simplified design proposals for post-tensioned timber frames were published [36]. Another research area focuses on the interaction between post-tensioned timber frames and the floor diaphragms [37], [38].

2.3.2 Post-tensioned timber beams and frames for gravity loads

Next to the system developed to resist earthquakes, some ongoing research in New Zealand has been focussing on post-tensioned timber beams made of LVL box beams (Figure 2.4), using straight and draped tendon configurations [39]. The load-carrying capacity could be increased up to 50% (serviceability state) and a numerical as well as an analytical model were introduced [40].

The research continued with developing frames for gravity loads [40]. Attention was given to the connection stiffness of the gravity frames and the modelling.

The "modified monolithic beam analogy" for frames under vertical loads was introduced and validated with tests. Design guidelines are therefore available for engineers for the developed post-tensioned gravity beams and frames [41].
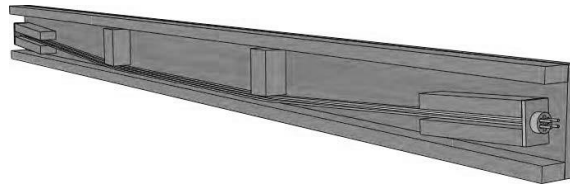
Figure 2.4: Post-tensioned LVL timber box beam with a draped tendon [40]

2.3.3 Long-term behaviour

Like in post-tensioned structures made of concrete, post-tensioned timber structures suffer from losses in tendon force over time. Many investigations were carried out on the relaxation of the pre-stressing force. Sarisley and Accorsi [42] tested a prototype stress-laminated timber-bridge deck. They found that loss of prestress force can be minimized by using disk springs on the tensioning rods, which reduces the effective stiffness of the prestressing system. Quenneville and Van Dalen [43] performed 10-month experimental tests on groups of laminated specimens that were stressed in compression perpendicular to the grain. Prestressing tendons can potentially reduce creep-induced deformations by balancing a portion of the long-term imposed load, and provide increased strength for long-span timber beams. Unbonded prestressing tendons have been used in the past to reduce the deflections of sawn timber beams [44]. Most recently, Fragiacomo and Davies [45], [46] performed experimental tests using LVL beam and frame specimens (Figure 2.5). They extrapolated the losses to 50 years, whereas the expected loss for the beam specimens was estimated to 6-10% and the loss for the frame specimens were estimated to 27-39%.
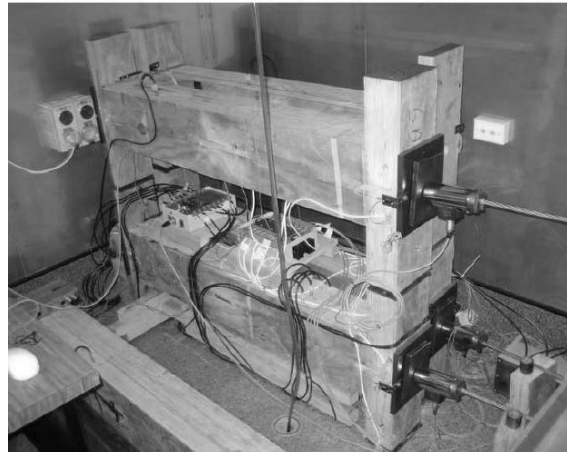
Figure 2.5: LVL specimens for long-term tests [45]

2.3.4 Structures with unbonded post-tensioned timber elements

A timber bridge for pedestrians in Murau, Austria, uses a tendon to stabilize the heavily stressed bottom flange of the structure (Figure 2.6(a)). The wooden bridge spans 47 m, is equipped with two large shear walls at the supports which allow a 24 m long gap in the middle of the bridge

to remain open [47], [48].

The "Swiss Re Centre for Global Dialogue" was built with post-tensioned timber girders made of glulam (Figure 2.6(b)). Since there are no columns in the façade, the beams cantilever 13 m. The beams are post-tensioned in order to reduce the deflections due to snow load [48].

(a)   (b)

Figure 2.6: 2.6(a): Bridge for pedestrians in Murau, Austria [49] 2.6(b): The "Swiss Re Centre for Global Dialogue" with post-tensioned timber beams [50]

Some buildings were already constructed with post-tensioned timber frames or walls as a structural element for the horizontal loads, vertical loads or the combination of these loads. The presented buildings herein are all based on the Pres-Lam® technology developed at the University of Canterbury (see previous Section 2.3), except for the building that was constructed in Zurich.

The first building constructed with a post-tensioned timber solution is the "Nelson Marlborough Institute of Technology Building " (NMIT), situated in Nelson, New Zealand (Figure 2.7(a)). The building is equipped with post-tensioned shear walls made of LVL to withstand earthquakes [51]. The same system was used to build the "Carterton Events Center " [52], [53], shown in Figure 2.7(b).

The first building constructed with a post-tensioned timber frame is situated on the campus of the Massey's college of creative arts in Wellington, New Zealand, and is called the "Te Ara Hihiko "-building [54]. The building was built with post-tensioned timber frames made of laminated veneer lumber as well as post-tensioned shear walls (see Figure 2.8(a)).

Another post-tensioned timber frame made of laminated veneer lumber was built in Christchurch, New Zealand, to construct the "Merritt building " [55]. The three-storey building was constructed with a frame including energy-dissipators in order to account for the seismic loads (Figure 2.8(b)).

The "St Elmo Courts " rebuilt in Christchurch [56] is a frame structure which is post-tensioned in two directions rather than only one. The frame is a hybrid, using precast concrete columns and LVL beams as shown in Figure 2.8(c).
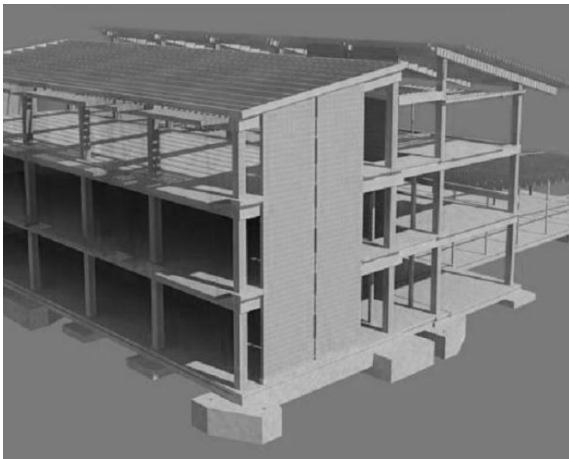
(a)   (b)

Figure 2.7: Buildings with post-tensioned timber walls 2.7(a): Visualisation of the "Nelson Marlborough Institute of Technology Building " [51] 2.7(b): "Carterton Events Center " [53]

In Europe, the only building with a post-tensioned timber frame is the "ETH House of Natural Resources" in Zurich, Switzerland and was designed based on the findings introduced in this document. The building was constructed with a two-storey timber frame made of glulam (Figure 2.8(d)). The frame was designed to resist vertical as well as lateral loads. No additional structural elements are required. The frame used in this building is the first post-tensioned timber frame that is prestressed in two directions. The columns are made of ash (hardwood), while the beams are made of spruce and ash.

(a)   (b)
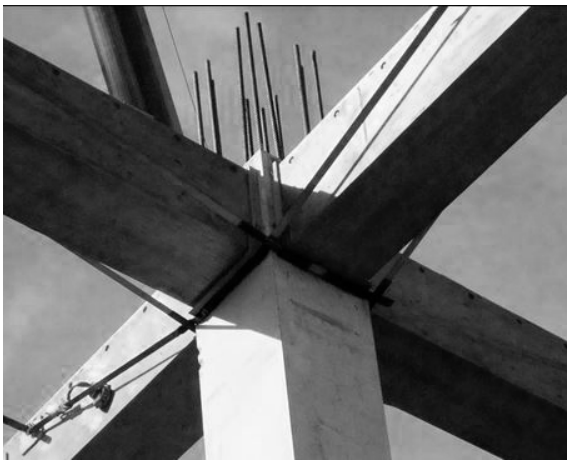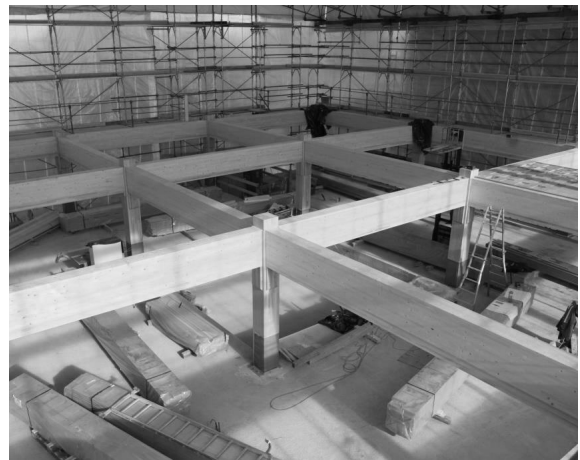
(c)   (d)

Figure 2.8: Buildings with post-tensioned timber frames 2.8(a): The "Te Ara Hihiko " - building [54] 2.8(b): The "Merritt building " [55] 2.8(c): Connection of the "St Elmo Courts " [56] 2.8(d): The "ETH House of Natural Resources" on the campus site of ETH in Zurich

Chapter 3

Analytical model

3.1 Simplified spring model

An analytical model to describe the behaviour of the post-tensioned timber connection is presented in this chapter. The model is based on a foundation, which is bedded on springs. This model is commonly known as a Winkler-foundation (Figure 3.1(a)) [57], [58].

Hereby, the Winkler foundation is used as analogy model, where a foundation is bedded on springs. In the case of the post-tensioned timber connection the springs replace the softer column (Figure 3.1(b)). The springs only bear compressive forces, which allow a gap to open between the column and the beam as soon as decompression occurs. The beam is modelled as a rigid body since it is much stiffer than the column.

<div align="center">(a)   (b)</div>
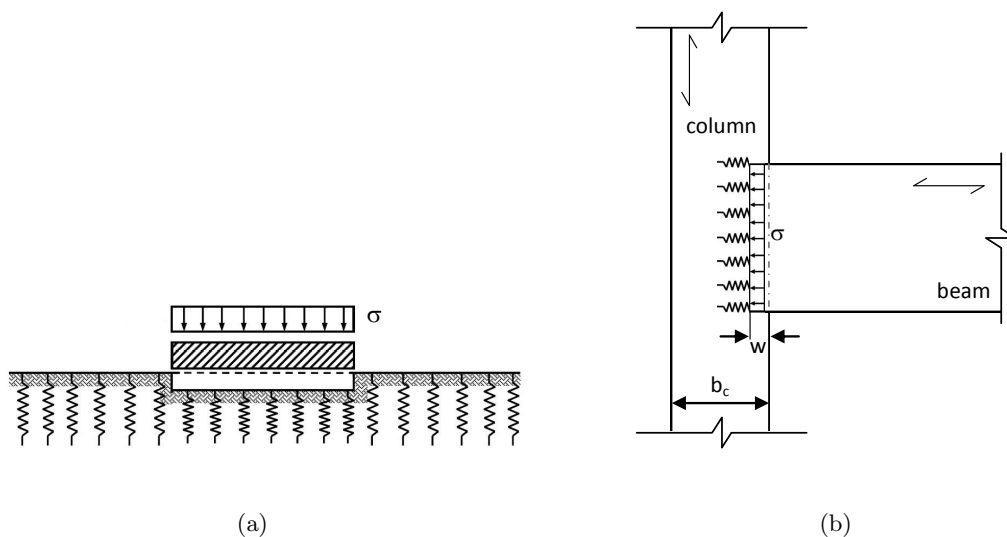
Figure 3.1: 3.1(a): Foundation on elastic bedding [59] 3.1(b): Beam-column connection with foundation on elastic bedding analogy

The analogy seems reasonable, since the beam, with a Young's modulus of 11'000-15'000 MPa [60], [61] parallel to the grain is much stiffer than the column, with a Young's modulus of ap-

proximately 800-1'400 MPa [62], [63] perpendicular to the grain. It is therefore assumed that the beam behaves like a rigid body since it is much stiffer than the column.

This assumption leads to a model called the trapezoidal stress method [57]. The model allows deriving the stresses under a foundation from the equilibrium conditions. An additional condition is the non-existence of tensile strength between foundation and the soil underneath. This condition is directly applicable to the herein presented connection. If tensile stresses occur, a gap will start to open in the connection interface.

Only one parameter is needed to model the column, the spring constant, or - since the springs are spread over an area - the modulus of subgrade reaction, which is the ratio of the stresses to the displacement:

$$c = \frac{\sigma}{w} \tag{3.1}$$

3.2 Modulus of subgrade reaction

The modulus of subgrade reaction is the only parameter needed for the model to describe the properties of the column. An easy and straightforward approach is to take half of the column into account (making use of the symmetry) and assuming a rigid beam. This approach has already been introduced by the author [64], [65] and leads to the expression:

$$c = \frac{\sigma}{w} = \frac{\sigma}{\frac{\sigma \cdot b_c}{E_{90} \cdot 2}} = \frac{2 \cdot E_{90}}{b_c} \tag{3.2}$$

Is assumed that $E_{90} = E_{c,90}$, which only leads to a small error [66] that is considered negligible regarding all the simplifications made by the analytical model. Equation (3.2) leads to good results, if the Young's modulus perpendicular to the grain is chosen according to the EN 338 [62]. However, if larger values for E_{90} from tests are considered [63], the equation above could lead to an overestimation of the modulus of subgrade reaction.

The modulus of subgrade reaction was estimated experimentally by the author with compression tests [67]. Smaller test specimens, representing the beam and the column, were used for the campaign as indicated in Figures 3.2(a) and 3.2(b).

The compression tests on small block specimens showed that a stress distribution in the column may be taken into account in order to estimate the modulus of subgrade reaction more accurately. If it is assumed, that the stresses are distributed according to Figure 3.3 [68]. An additional parameter Δ is introduced, to describe a certain distribution of the stresses in the column. If nothing else is stated in the analysis within this thesis, the parameter Δ is set to zero, i.e. no stress distribution is taken into account.

The average stresses in the connection (at a depth $b_c/4$ according to Figure 3.3) can be calculated as follows:
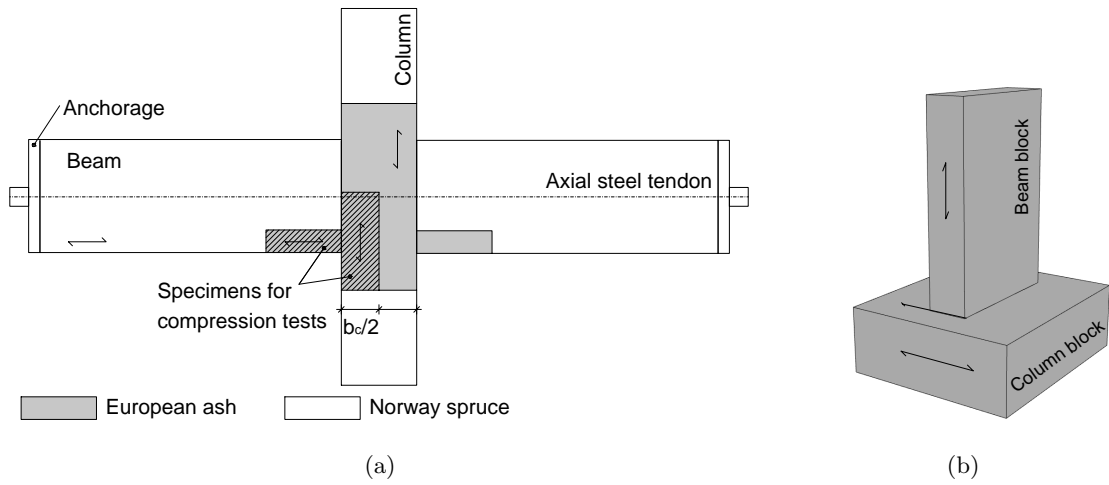
Figure 3.2: 3.1(a): Post-tensioned timber connection with tests specimens for compression tests marked with cross line pattern 3.1(b): Specimens for compression tests [67]
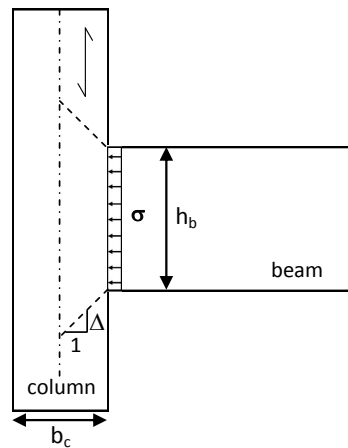
Figure 3.3: Stress distribution in the column

$$\sigma_m = \frac{P}{b_b \cdot (h_b + \Delta \cdot b_c/2)} \tag{3.3}$$

The modulus of subgrade reaction can be calculated as follows for the case with the stress distribution in the column:

$$c = \frac{\sigma_m}{w} = \frac{h_b}{h_b + \Delta \cdot b_c/2} \cdot \frac{2 \cdot E_{90}}{b_c} \tag{3.4}$$

The modulus of subgrade reaction is a function of the Young's modulus perpendicular to the grain and the geometry if the load distribution is neglected. All these values are available to an engineer, making the suggested model easy to use.

However, if the configuration of the connection is altered, it is strongly recommended to perform compression tests in order to verify the modulus of subgrade reaction. Good results were obtained by evaluating compression tests on smaller specimens with a coupled springs approach or Boussinesq's solution [67].

3.3   Equations for stresses, rotation and neutral axis depth

The tendon force presses the beam against the column. In addition to the normal force a moment acts on the interface as soon as the beam is loaded, which may lead to a gap opening between the beam and the column. Three states need to be considered; once for the state before decompression (full contact between beam and column), once for the state after decompression (gap opening) and for the state, where the gap reaches the tendon.

3.3.1   Before decompression

In a first state, the whole cross section is under compression. The neutral axis depth x is therefore equal to the height of the beam h_b.
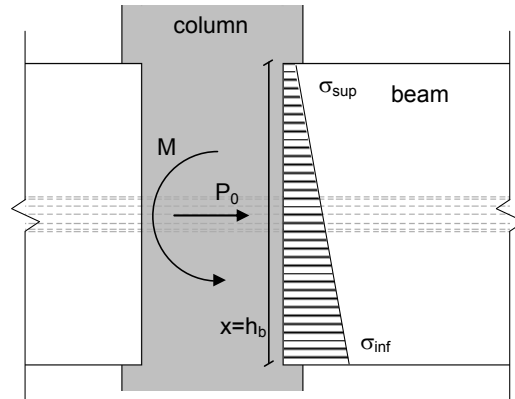
Figure 3.4: Interface before decompression

The balance of forces and the equilibrium of moments lead to the Equations (3.5) to (3.8).

$$x = h_b \tag{3.5}$$

$$\sigma_{inf} = \frac{P_0}{A_b} + \frac{M}{W_b} = \frac{P_0}{b_b \cdot h_b} + \frac{M}{\frac{b_b \cdot h_b^2}{6}} \tag{3.6}$$

$$\sigma_{sup} = \frac{P_0}{A_b} - \frac{M}{W_b} = \frac{P_0}{b_b \cdot h_b} - \frac{M}{\frac{b_b \cdot h_b^2}{6}} \tag{3.7}$$

$$\theta = \frac{\sigma_{inf} - \sigma_{sup}}{c} \cdot \frac{1}{x} \tag{3.8}$$

An expression for the moment can be derived by putting Equations (3.5) to (3.7) into Equation (3.8):

$$M = c \cdot \frac{b_b \cdot h_b^3}{12} \cdot \theta = c \cdot I_b \cdot \theta \tag{3.9}$$

All these equations are valid until decompression occurs. At the moment of decompression the stresses at the top edge of the interface are equal to zero ($\sigma_{sup} = 0$) and a gap will start to open. The moment at this point is called moment of decompression and can be calculated by setting Equation (3.7) equal to zero:

$$M_{dec} = P_0 \cdot \frac{h_b}{6} \tag{3.10}$$

3.3.2   After decompression

In this state only a part of the cross section is under compression as shown in Figure 3.5. The rest of the cross section has no stresses at all, since there is no tensile strength at the interface between column and beam. This also means that a gap will start to open, as soon as decompression sets in.

Like in the previous section, the following equations are derived from the balance of forces and the equilibrium of moments.
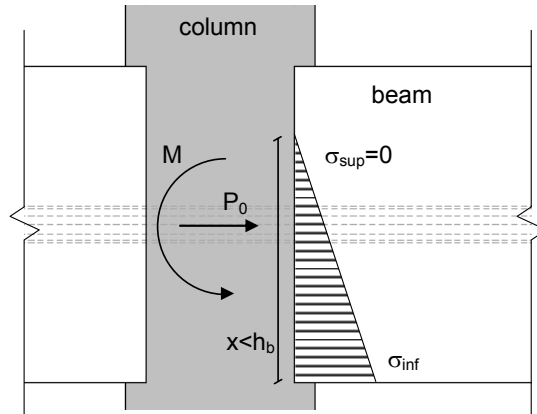
Figure 3.5: Interface after decompression

$$x = 3 \cdot \left(\frac{h_b}{2} - \frac{M}{P_0} \right) \tag{3.11}$$

$$\sigma_{inf} = \frac{2 \cdot P_0}{3 \cdot b_b \cdot \left(\frac{h_b}{2} - \frac{M}{P_0}\right)} \tag{3.12}$$

$$\sigma_{sup} = 0 \tag{3.13}$$

$$\theta = \frac{\sigma_{inf}}{c} \cdot \frac{1}{x} \tag{3.14}$$

An expression for the moment can be derived by putting Equations (3.11) and (3.12) into Equation (3.14):

$$M = P_0 \cdot \left(\frac{h_b}{2} - \sqrt{\frac{2}{9} \cdot \frac{P_0}{b_b \cdot c \cdot \theta}}\right) \tag{3.15}$$

3.3.3 Gap reaches the tendon

As the neutral axis depth x gets smaller, the gap gets larger. If the gap reaches the tendon and is still getting larger, the tendon will get elongated eventually. This elongation increases the force in the tendon, which has to be taken into account during the analysis.
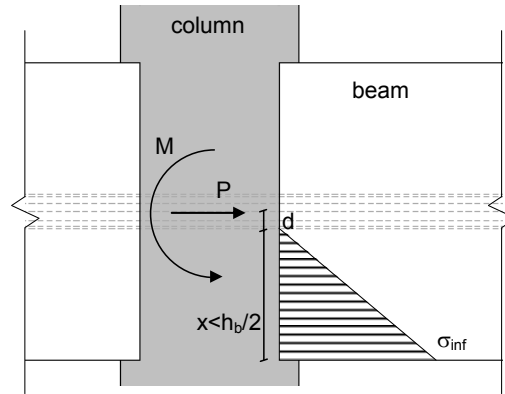
Figure 3.6: Interface after tendon elongation

Equations (3.11) to (3.14) remain valid, only the force in the tendon is not constant any more. The variable P_0 has to be replaced with a variable P. In order to calculate the new force in the tendon P, the elongation of it has to be estimated first. The elongation is:

$$\Delta L_p = \theta \cdot d \tag{3.16}$$

With d being the distance between the tendon and the edge of the gap. The increase in tendon force is then:

$$\Delta P = A_p \cdot E_p \cdot \frac{\Delta L_p}{L_p} \tag{3.17}$$

This value can be added to initial tendon force:

$$P = P_0 + \Delta P = P_0 + A_p \cdot E_p \cdot \frac{\theta \cdot d}{L_p} = P_0 + A_p \cdot E_p \cdot \frac{\theta \cdot (h_b/2 - x)}{L_p} \tag{3.18}$$

With the force in the tendon as an unknown parameter, the solution has to be determined iteratively by using Equations (3.11) to (3.14) and (3.18).

3.3.4 Shear deformations

In a case where both beams are loaded symmetrically, the resulting force R in the interface is at the same position as shown in Figure 3.7(a). This means that the behaviour in the column can be described only with the Young's modulus perpendicular to the grain E_{90}, since the column is being compressed from both sides equally.

(a)   (b)
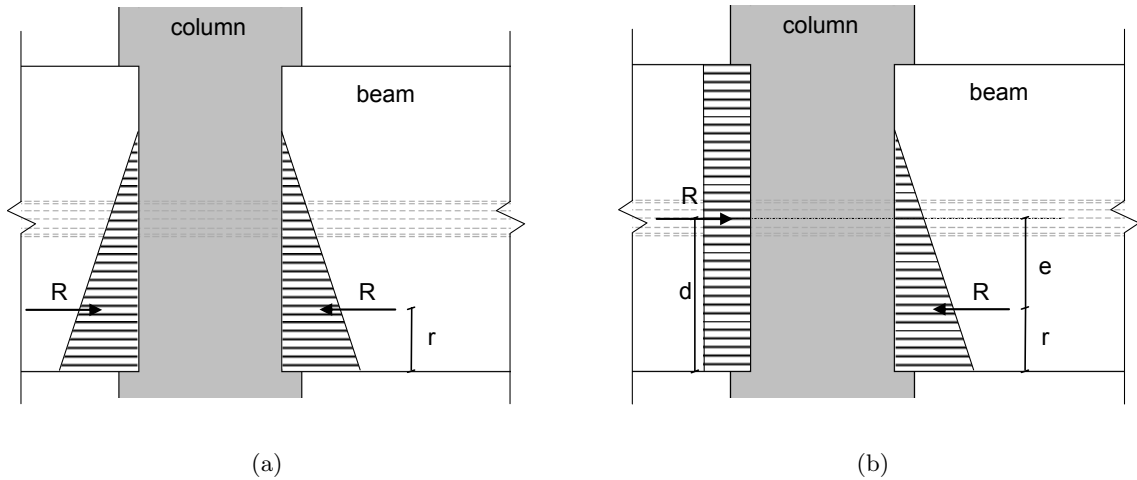
Figure 3.7: 3.7(a): Resulting force R for symmetrical load case 3.7(b): Resulting force R for asymmetrical load case

If only one beam is loaded, the structural behaviour is slightly different. At the interface between the column and the unloaded beam, the resulting force is in the middle of the cross section $(d = h/2)$, since no moment is applied and the only force acting on the interface is the tendon force. For the loaded beam the resulting force is moving towards the lower edge of the beam as the load increases. Its position is defined with r, which is the distance from the bottom of the beam to the resulting force R as shown in Figure 3.7(b).

Since the resulting forces are in different positions, a shear deformation occurs and increases

the rotation in the connection. However, the shear angle γ does not correspond precisely to the increase in rotation. The shear angle is generally defined as a function of the cross section area of the column A_c, the shear modulus G_c and the resulting force R:

$$\gamma = \frac{R}{G_c \cdot A_c} \tag{3.19}$$
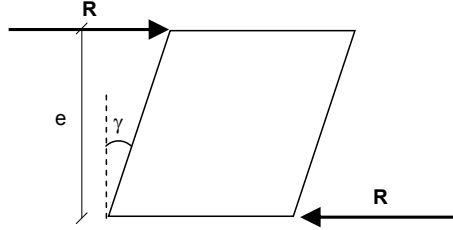
Figure 3.8: Definition shear angle

The first two parameters are absolute terms; therefore the shear angle can only change with altering resulting force. This approach is unfortunately not directly applicable for the post-tensioned timber connection, since the resulting force corresponds to the tendon force at all times. This would mean that the shear angle is constant until the gap reaches the tendon and elongates it.

The variation of the shear angle γ is described as a function of the eccentricity e of the resulting forces R. The position of the resulting force for the loaded beam has to be calculated in order to estimate the eccentricity e of the resulting forces R. For a trapezoidal stress distribution (before decompression) the distance between the resulting force and the lower edge of the beam is:

$$r = h_b - \frac{\sigma_{sup} \cdot h_b^2/2 + (\sigma_{inf} - \sigma_{sup}) \cdot h_b^2/3}{\sigma_{sup} \cdot h_b + (\sigma_{inf} - \sigma_{sup}) \cdot h_b/2} \tag{3.20}$$

and for a triangular shaped stress distribution (after decompression):

$$r = x/3 \tag{3.21}$$

The eccentricity between the two resulting forces is then:

$$e = d - r \tag{3.22}$$

with d being the position of the tendon measured from the lower edge of the beam. In the interface between column and beam (see Figure 3.9), the shear deformation is concentrated over a height e (dashed lines), between the two resulting forces. The rest of the column, however, will also be deformed, i.e. the shear deformation will occur over the total height h_b.
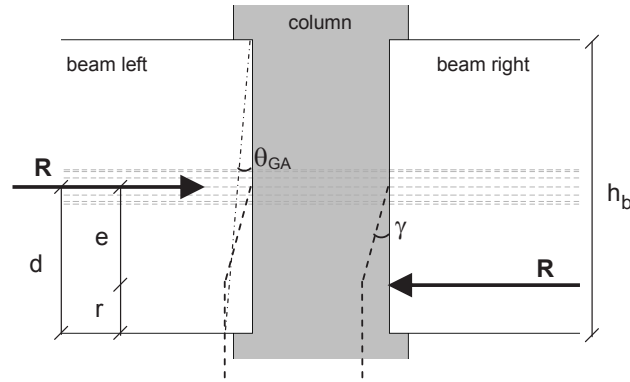
Figure 3.9: Shear deformation column

In order to estimate the rotation due to shear deformation, the latter is re-distributed over the entire height h_b. The deformed shape as shown in Figure 3.9 (dash-dotted lines) is assumed. With this assumption an expression for the increase in rotation can be derived:

$$\theta_{GA} \cdot h_b = \gamma \cdot e \tag{3.23}$$

$$\theta_{GA} = \frac{\gamma \cdot e}{h_b} = \frac{R}{G_c \cdot A_c} \cdot \frac{e}{h_b} = \frac{P}{G_c \cdot A_c} \cdot \frac{e}{h_b} = \frac{M}{G_c \cdot A_c \cdot h_b} \tag{3.24}$$

The rotation due to shear deformation (θ_{GA}) has to be added to the rotation calculated according to Equation (3.8) or Equation (3.14), respectively. This is only necessary for the tests with asymmetrical and combined loading, namely where one beam is loaded with a different moment compared to the other beam.

3.3.5   Compression failure

Failure can occur in the column, since it is loaded perpendicular to the grain. The spring model is purely elastic, grain crushing can only be taken into account by changing the spring stiffness c. A reduction of the spring stiffness leads to a softer column and therefore to an increase in rotation. This procedure is chosen to compare the model with the tests where high stresses perpendicular to the grain occurred.

The reduction of the spring constant was chosen arbitrarily. A bilinear stress-strain curve was generated to calculate the modified spring constant c_{mod}. This procedure allows implementing the modification in the model in a very pragmatic way. The reduction of the spring constant leads to larger displacements in the column and therefore to larger rotations, as can be seen in Equations (3.8) and (3.14), respectively.

3.4   Horizontal loads and pushover curve

The proposed analytical model can also be used to compare the results obtained from the pushover-tests. The model assumes that the beams are rigid, therefore a simplified system as shown in Figure 3.10 is introduced for the calculations. Since the beams are not being taken into account, the system can be reduced to the columns themselves. The connection behaviour can be determined by using the analytical model.
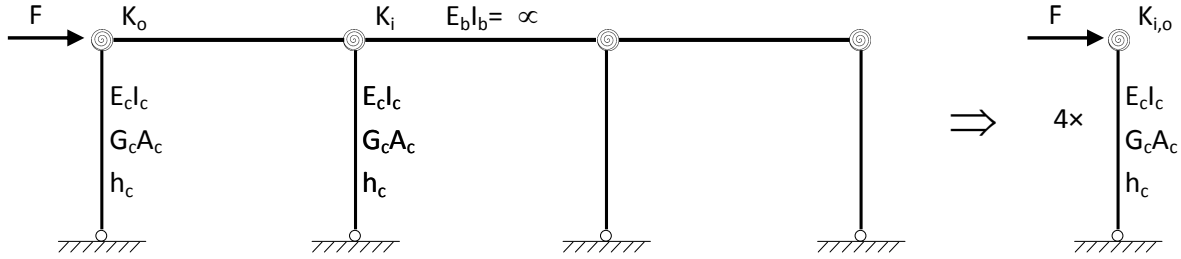
Figure 3.10: Simplified system for analytical calculation of the pushover-curve

In order to compare the pushover-tests with the analytical solution, the equations for the latter need to be re-written. The stiffness of a single connection is defined as:

$$K = \frac{M}{\theta_{tot}} = \frac{M}{\theta + \theta_{GA}} \tag{3.25}$$

Using the Equation (3.25) and (3.9) (for the case before decompression) as well as Equation (3.24), the following expression can be derived:

$$K = \frac{M}{\frac{12 \cdot M}{c \cdot b_b \cdot h_b^3} + \frac{M}{G_c \cdot A_c \cdot h_b}} = \frac{G_c \cdot A_c \cdot c \cdot b_b \cdot h_b^3}{c \cdot b_b \cdot h_b^2 + 12 \cdot G_c \cdot A_c} \tag{3.26}$$

A differentiation between the inner and outer columns is necessary, since the latter contain the anchorages for the tendon. This means that on one side the resulting force will always be in the middle of the connection, i.e. at the position of the tendon. For the inner column, the resulting force in one beam will move upwards while the resulting force in the other beam shifts downwards. This leads to different rotations due to shear and therefore to a different stiffness for the inner and outer columns.

Furthermore, since the inner columns have two interfaces, the rotation due to compression can be divided in half:

$$K = \frac{M}{\frac{12 \cdot M}{c \cdot b_b \cdot h_b^3} \cdot \frac{1}{2} + \frac{M}{G_c \cdot A_c \cdot h_b}} = \frac{G_c \cdot A_c \cdot c \cdot b_b \cdot h_b^3}{c \cdot b_b \cdot h_b^2 + 6 \cdot G_c \cdot A_c} \tag{3.27}$$

This differentiation allows to model the frame with a single spring at the beam-column interface for the outer columns (K_o) and the inner columns (K_i).

The horizontal displacement for the simplified system can then be calculated with:

$$u = \frac{M \cdot h_c^2}{3 \cdot E_c \cdot I_c} + \frac{M}{G_c \cdot A_c} + \frac{M \cdot h_c}{K} = \frac{F \cdot h_c^3}{3 \cdot E_c \cdot I_c} + \frac{F \cdot h_c}{G_c \cdot A_c} + \frac{F \cdot h_c^2}{K} \qquad (3.28)$$

The first term is the displacement due to bending in the columns, the second due to shear deformations of the columns, the last term is due to the rotation in the connections.

One compatibility condition is also being introduced; the horizontal displacement at the top of each column is equal for all columns.

3.4.1 Ultimate limit state

If the tendon elongation is neglected, an analytical solution for an ultimate limit state can be derived. The maximal moments for the connections correspond to the stage when the eccentricity between the resulting forces is equal to the height of the beam (inner column):

$$M_{max,i} = P_0 \cdot h_b \qquad (3.29)$$

For the outer column the moment can be calculated with half of the height of the beam, i.e. the distance between the position of the tendon and the edge of the beam:

$$M_{max,o} = P_0 \cdot \frac{h_b}{2} \qquad (3.30)$$

This leads to the following expression for the applicable horizontal load:

$$F_{max,hor} = \frac{2 \cdot M_{max,i} + 2 \cdot M_{max,o}}{h_c} = \frac{3 \cdot P_0 \cdot h_b}{h_c} \qquad (3.31)$$

The Equations (3.29)-(3.31) assume that failure will occur in the connection area. The bending and shear strength of the beams and the columns still have to be checked in order to prevent failure in those elements.

Chapter 4

Connection tests

This chapter is a summary of the tests performed on a post-tensioned timber connection under gravity loads. A more detailed test report is available [69], where drawings, specifications on the test equipment and the test evaluation of all performed tests can be found.

4.1   Material and test setup

The test specimen consists of two beams and a column. All three elements are made of glulam, whereas the beams are made of Norway spruce (*picea abies*) except for three lamellae, which are made of European ash (*fraxinus excelsior*). The column is also a hybrid made of Norway spruce and European ash. Figure 4.1 shows the specimen whereas all ash elements are shaded in grey. The hardwood is used in areas where high stresses perpendicular to the grain occur, namely in the connection between the column and the beam. The values for strength and stiffness of the materials are summarised in Table 4.1.
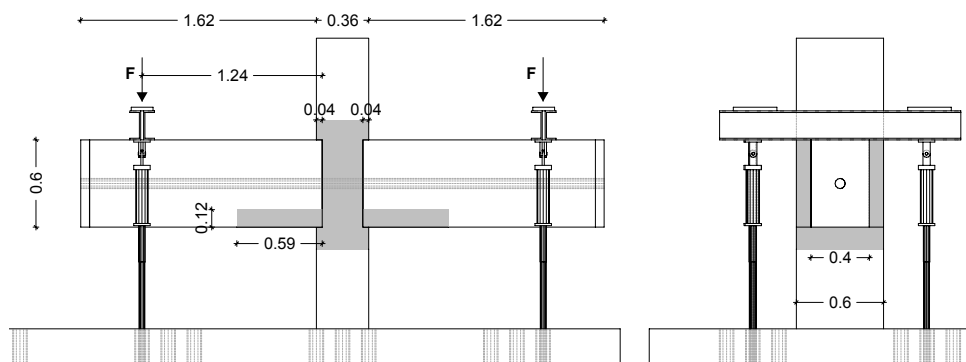
Figure 4.1: Specimen and load application, all dimensions in [m]

A tendon is attached at the outer sides of both beams. A thick steel plate is necessary at the end of the beams for the load transmission from the tendon to the beams.

The shear force between beams and column is transferred via friction. By cutting a small

Table 4.1: Strength and stiffness properties in [MPa] for strength grade GL24h (beams) [60] and D40 (columns) [62]

Property	Strength grade	
	GL24h	D40
$f_{c,0,k}$	22	26
$f_{c,90,k}$	3	8.3
E_0	11000	13000
E_{90}	300	860
G	500	810

opening into the column a support was created for safety reasons in case the friction would not be sufficient. The properties of the tendon are summarised in Table 4.2.

Table 4.2: Tendon properties according to [70]

Property	Y1770 4-06
A_p	600 mm^2
L_p	4200 mm
E_p	197000 Mpa
$f_{p,k}$	1770 MPa

A rigid steel frame was built for the tests (see Figure 4.2) in order to constrain the specimen. A force is applied by two cylinders on both sides of the specimen. The cylinders are connected to the same hydraulic pump, but can be controlled separately, so that several load cases can be investigated.
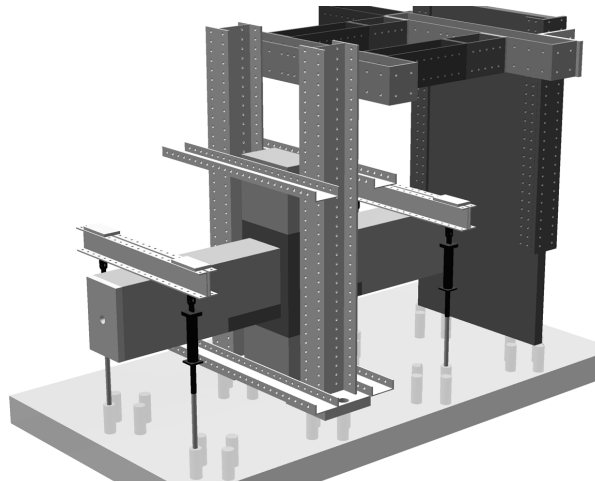
Figure 4.2: CAD drawing of the test setup (without tendon)

4.2 Instrumentation

To investigate the structural behaviour of the post-tensioned timber connection several types of measuring devices were used:

- Linear voltage displacement transducers (LVDTs)

- Inclinometers

- Pressure sensors

- Load cell

All abbreviations and information regarding range are summarized in Table 4.3.

Table 4.3: Measuring Equipment

Description	Abbreviation	Range
LVDT interface	WRV1...	± 5 mm
LVDT deflection	Durch L, Durch R	± 25 mm
Inclinometer	IL1 IL2 IR1 IR2	± 5 °
Pressure sensor	FSR	0.2-20N
Load cell	KMD	1250kN

The LVDTs record the displacements between the column and the beams. The rotation of the connection (or the beam) can be calculated from the recorded values. One LVDT is also attached at the bottom of each beam to measure its deflection (*DurchL* and *DurchR* in Figure 4.3).
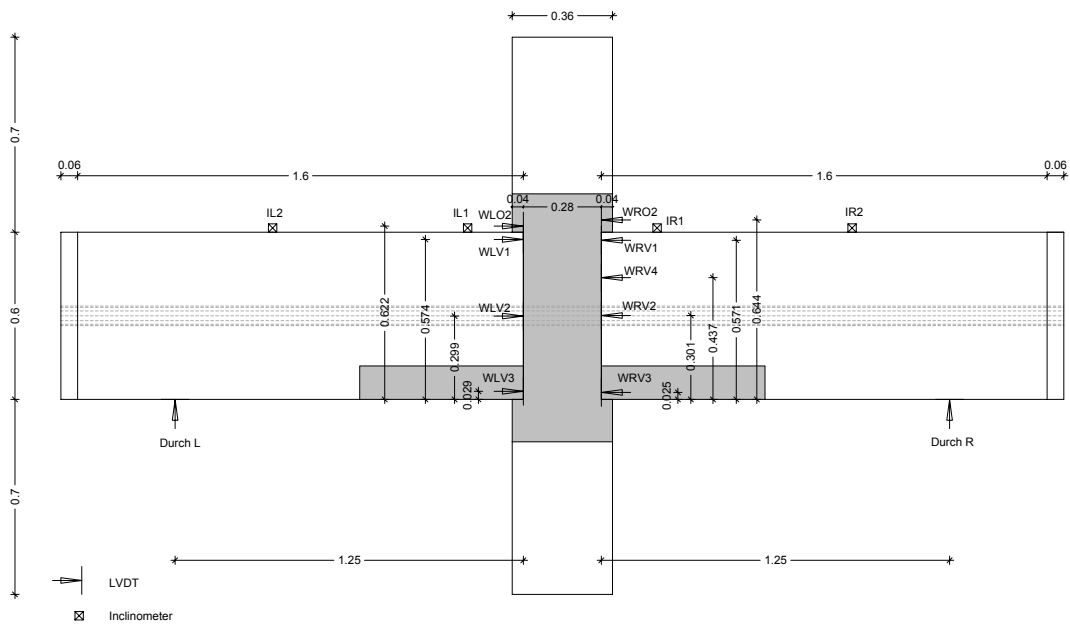
Figure 4.3: Instrumentation: LVDTs and inclinometers, all dimensions in [m]

Two inclinometers are positioned on top of each beam. With this equipment the inclination of the beams can be measured directly. The rotation in the connection can be calculated from these values if the inclination of the beam is subtracted. There are therefore two ways to calculate the rotation, which leads to more reliable results.

Two pressure sensors of the type FSR 400 are used to estimate the moment of decompression. As soon as the moment of decompression is reached, the sensor will measure no more pressure. The pressure sensors are only attached on the right beam. One of these pressure sensors is shown in Figure 4.4.

Figure 4.4: FSR pressure sensor at the connection interface

The pressure sensor is positioned right under the top edge of the beam and is connected to an adjustable screw. The screw is necessary to create a clearly defined contact area. If the pressure is zero, the point of decompression has been reached and a gap will start to open between the beam and the column interface.

A load cell is positioned between the tendon and the anchorage. The load cell measures the force in the tendon in addition to the tendon force obtained from the oil pressure.

4.3   Testing program

A total of 22 tests were performed at the ETH Zurich. The tests one to twelve are preliminary tests, which were performed to calibrate the measuring equipment and will not be discussed herein. Test 19 is not considered due to an error in the hydraulic system. The tests were performed with different post-tensioning forces and different kinds of load applications. The maximal applied load varies from test to test.

Three different load applications were performed:

- (B) Both beams are loaded and unloaded at the same time (symmetric loading).

- (O) Load is applied on one beam, the second beam remains un-loaded (asymmetric loading).

- (C) Combined load application. One beam is pre-loaded to a certain, constant value, the second beam is then loaded and unloaded to different (higher) values (asymmetric loading).

By applying the load only on one beam, a load combination is generated, which is closer to a horizontal load on a post-tensioned timber frame (earthquake, wind loads), since shear deformations occur in the connection area. All the tests, except test 22, consist of the three parts:

- 1. Symmetrical loading (B), 3-4 loading and unloading cycles which end at t = 1700 s in Figure 4.5.

- 2. Asymmetrical loading, right beam under constant load. At t = 1700 s, the left beam is loaded to 40 kN, unloaded and reloaded again up to 70 kN while the right beam remains unloaded (O). This procedure is repeated with different loads levels on the right beam (C).

- 3. Asymmetrical loading, left beam under constant load. At t = 2700 s, the right beam is loaded to 40 kN, unloaded and reloaded again up to 70 kN while the left beam remains unloaded (O). This procedure is repeated with different loads levels on the left beam (C).
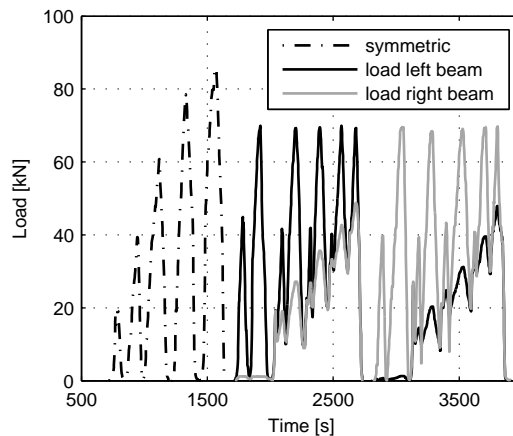
Figure 4.5: Load-time diagram for a typical test

It can be noticed that the loads are not exactly constant. Since one beam is loaded more than the other one, the beam with the heavier load is being pulled down, the beam with less load tends to move upwards, but is restrained by the cylinders. Therefore the load in the cylinders increases slightly.

The analysis often refers to a load level (for example 80 kN). This values always corresponds to the peak value of a load cycle, i.e. in the test shown in Figure 4.5 the value 80 kN would correspond to the peak at 1600 s.

An overview of all performed tests is given in Table 4.4 including applied tendon force, load application and the maximal applied load on the beam.

<div align="center">

Table 4.4: Performed tests

Test No.	Tendon force [kN]	Load application	Applied load [kN]
13	518	B,C,O	80
14	416	B,C,O	60
15	612	B,C,O	80
16	325	B,C,O	50
17	683	B,C,O	70
18	560	B,C,O	80
20	462	B,C,O	75
21	554	B,C,O	90
22	557	B	157

</div>

4.4 Experimental analysis - equations

4.4.1 Structural behaviour

While pre-stressing the tendon, the beams are being pressed against the column. This leads to an initial compression at the beam-column interface, which can be measured with the LVDTs. From these values, a mean initial value for the compression can be estimated. Figure 4.6 shows the measured compression, i.e. the position of an LVDT, at the interface between the beam and the column (circles) as well as the interpolated values (lines). At the load level F = 0 kN (tendon force is applied without any load on the beam), the measurements show a uniform horizontal displacement of approximately -0.3 mm.

If the vertical load is applied on the beams, the interface starts rotating which leads to decompression and to an opening of a gap in the upper connection area as shown in Figure 4.7. This rotation can also be seen in Figure 4.6, where the recorded horizontal displacements from the LVDTs increase during a test with increasing load F. Therefore, the rotation corresponds to the slope of the interpolated lines.
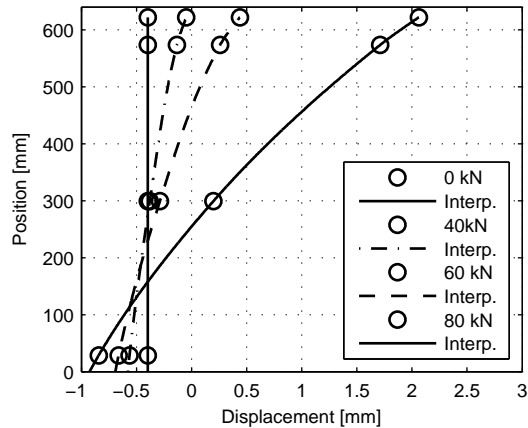
Figure 4.6: Horizontal displacement at the beam-column interface. Position = height of the beam measured from the bottom. Load levels = load F on the beam
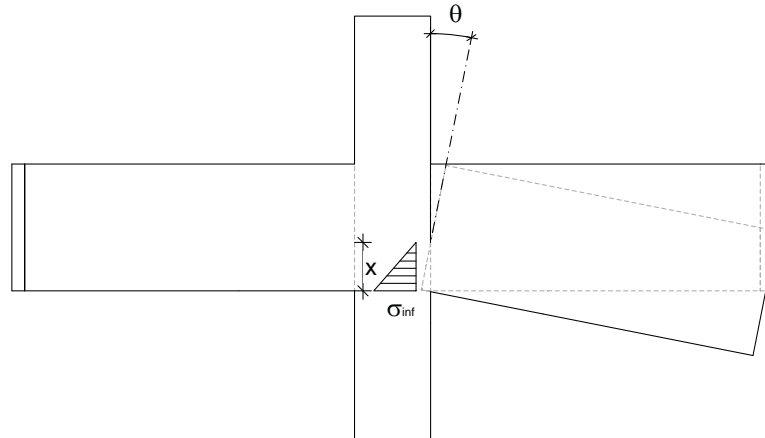
Figure 4.7: Definition of the rotation θ, maximal compressive stress σ_{inf} and neutral axis depth x

4.4.2 Key variables

Rotation and neutral axis depth

The rotation θ, as mentioned in the previous subsection, can be calculated with the LVTDs and corresponds to the slope of the interpolation functions between the single LVTDs (Figure 4.6). Furthermore, four inclinometers are attached on the beams, which allow to measure the rotation directly, after the elastic rotation is subtracted from the measured results. This procedure was only used to verify the rotations calculated from the LVTDs.

The neutral axis depth x can also be estimated using the slope of the interpolation functions of the LVDTs. The height is equal to the value, where the interpolation function intersects with the value 0 mm for the displacement. In Figure 4.6 the height of the compressive zone is equal to 600 mm for the load cases F = 0 kN and F = 40 kN. For the load F = 60 kN, the neutral axis depth is 450 mm, for the load F= 80 kN approximately 260 mm.

The rotation and the neutral axis depth can be calculated as follows :

$$w_{WLO} = \theta \cdot (621 - x) = \theta \cdot 621 - \theta \cdot x = \theta \cdot 621 - w_{inf} \tag{4.1}$$

$$w_{WL1} = \theta \cdot (572 - x) = \theta \cdot 572 - \theta \cdot x = \theta \cdot 572 - w_{inf} \tag{4.2}$$

$$w_{WL2} = \theta \cdot (300 - x) = \theta \cdot 300 - \theta \cdot x = \theta \cdot 300 - w_{inf} \tag{4.3}$$

The numbers correspond to the position of the LVDTs, measured in mm from the bottom of the beam. The values w_{WLO}, w_{WL1} and w_{WL2} are the mean measured deformation for each set of LVDTs (back and front). The value w_{inf} corresponds to the calculated displacement at the lower edge of the interface based on linear-elastic theory. It is assumed, that the interpolation function is linear. The sensors at the lower edge of the beam are not taken into account, since they are in the compression zone, where the deformations will most likely not be linear (plastic deformation in the column). With two unknown values θ and x and three equations (respectively four for the right beam) the problem can be solved.
The value for x is calculated from w_{inf} by a back substitution:

$$w_{inf} = x \cdot \theta \rightarrow x = \frac{w_{inf}}{\theta} \tag{4.4}$$

Moment

In order to understand the behaviour of the connection, a rotational spring can be chosen as a simplified model. A rotational spring is defined with a moment-rotation relationship. Thus, all results in the following sections will be presented as a function of the moment acting on the interface rather than the applied force F. The moment can be calculated, by multiplying the applied force F with the distance between the load application and the beam-column interface L_F.

$$M = F \cdot L_F \tag{4.5}$$

Tendon force

The tendon force is measured with a load cell, placed between the anchorage of the tendon and the steel plate. The force in the tendon can also be calculated with the oil pressure in the hydraulic system.

Maximal stresses in the column

The stresses in the column (perpendicular to the grain) are the controlling design criterion and should be estimated accurately. With the equilibrium of forces and an assumption for the stress distribution (linear-elastic) according to Figure 4.7, it is possible to calculate the maximal stresses in the interface.

$$\sigma_{inf} = \frac{2 \cdot P}{x \cdot b_b} \tag{4.6}$$

Equation (4.6) is only valid after decompression. Until decompression the following expression has to be used in order to calculate the maximal stresses in the column:

$$\sigma_{inf} = \frac{P}{A_b} + \frac{M}{W_b} \tag{4.7}$$

4.5 Experimental analysis - test evaluation

The experimental campaign includes a total of 22 tests with different tendon forces and load levels. Four representative tests are presented herein:

- Test with a high tendon force

- Test with an intermediate tendon force

- Test with a low tendon force

- Test with high load level (loading up to failure)

The dependency of the tendon force on the structural behaviour of the connection is an important factor, since a loss in tendon force has to be expected in post-tensioned timber structures (see also Chapter 7 for further details regarding tendon force losses). The forces are chosen according to the initial stress on the beam-column interface. A tendon force of 680 kN results in an initial stress of 2.8 MPa, a force of 550 kN leads to a stress of 2.3 MPa and the low tendon force of 450 kN to 1.9 MPa initial stress. These values correspond to load levels which are assumed to be sensible for practical applications. The load level is defined as the ratio between the stress acting on the column and its strength perpendicular to the grain $f_{c,90,mean}$. Assuming an initial stress fo 2.8 MPa, a strength class D40 [62] and a ratio between mean value and characteristic value according to JCSS [71] the load ratio can be calculated:

$$\frac{\sigma}{f_{c,90,mean}} = \frac{2.8}{8.3 \cdot 1.197} = 0.28 \tag{4.8}$$

The load ratio for an intermediate and low tendon force is 0.23 and 0.19, respectively.

4.5.1 Test with a high tendon force

Initial compression

The initial compression can be estimated by plotting the displacements between the beam and the column during pre-stressing of the system, as shown in Figures 4.8(a) and 4.8(b). The plots show a linear increase in displacement for tendon forces P over 100 kN. The beams are being pressed into the column nearly uniformly.

(a)   (b)
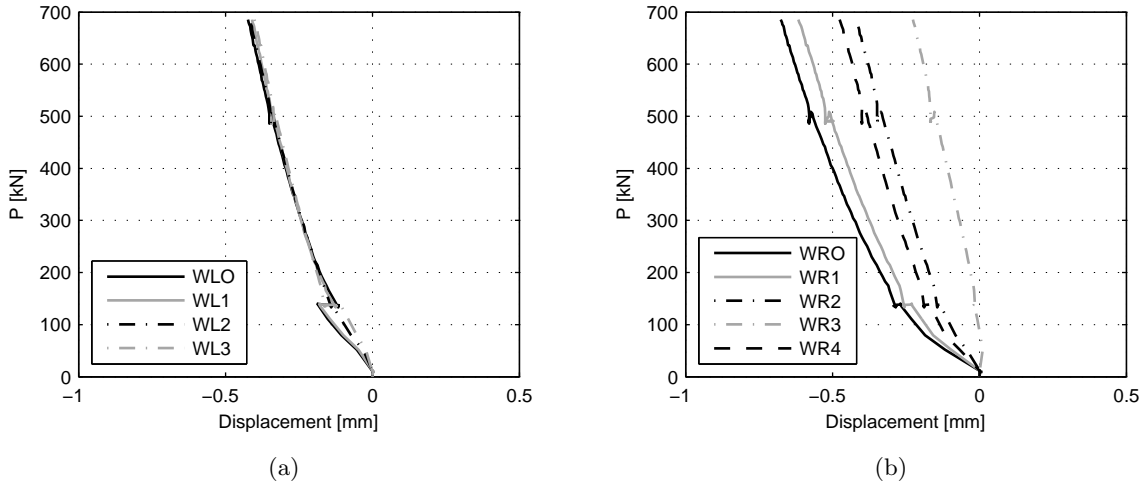
Figure 4.8: 4.8(a): Initial compression for a tendon force P of 680 kN at the left interface 4.8(b): Initial compression for a tendon force P of 680 kN at the right interface

The average value of the initial compression for the left beam can be estimated with:

$$w_{comp,left} = 0.35 \text{ mm} \tag{4.9}$$

For the right beam this value is slightly higher:

$$w_{comp,right} = 0.41 \text{ mm} \tag{4.10}$$

These values are approximations, also since the LVDTs measure the initial compression at the outer perimeter of the beam.

Evaluation symmetrical load case

Figure 4.9 shows plots off all the key variables as a function of the rotation θ. According to the results in the moment-rotation diagram (Figure 4.9(a)), the two connections (i.e. the left and the right interface) behave nearly identical.

The tendon force remains constant during the test (Figure 4.9(b)). No elongation of the tendon was observed, which means that the gap did not reach the position of the tendon.

The neutral axis depth is constant at a value of 600 mm up to a rotation of 1.5 mrad (Figure 4.9(c)). Then it starts to decrease, which means that at a rotation of 1.5 mrad the moment of decompression is reached. During the test a feeler gauge was used to check from which point on a gap has opened. A gap was noticed at a load of 55 kN, which corresponds to a moment of 68 kNm. The circle in the diagram shows the moment of decompression according to the pressure sensor (FSR), which correlates very well with the estimated moment of decompression. The stresses (Figure 4.9(d)) increase up to 7 MPa, which is still in the expected elastic range of the column.
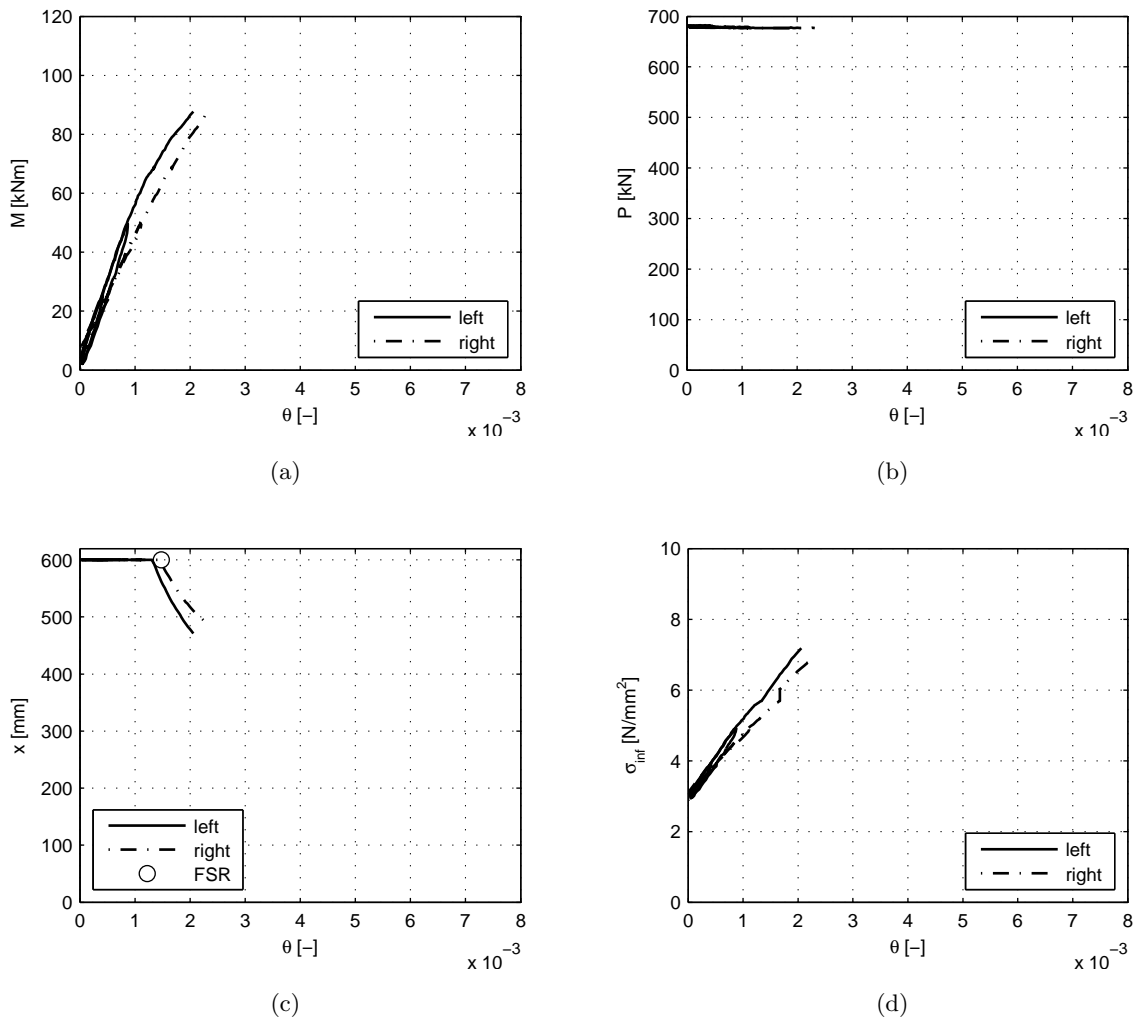
Figure 4.9: Evaluation of the symmetrical load case with high tendon force 4.9(a): Moment-rotation behaviour 4.9(b): Tendon force 4.9(c): Neutral axis depth 4.9(d): Stresses at the interface

Evaluation asymmetrical load case

It is noticeable from the moment-rotation-diagram (Figure 4.10(a) and 4.10(b)), that the initial stiffness of the connection deteriorates with decreasing load on the other beam. This effect is due to shear deformations in the column, which only occur during asymmetrical loading. The

connection stiffness is highest if both beams are loaded simultaneous (symmetric load case) since
no shear deformations occur.

(a)   (b)
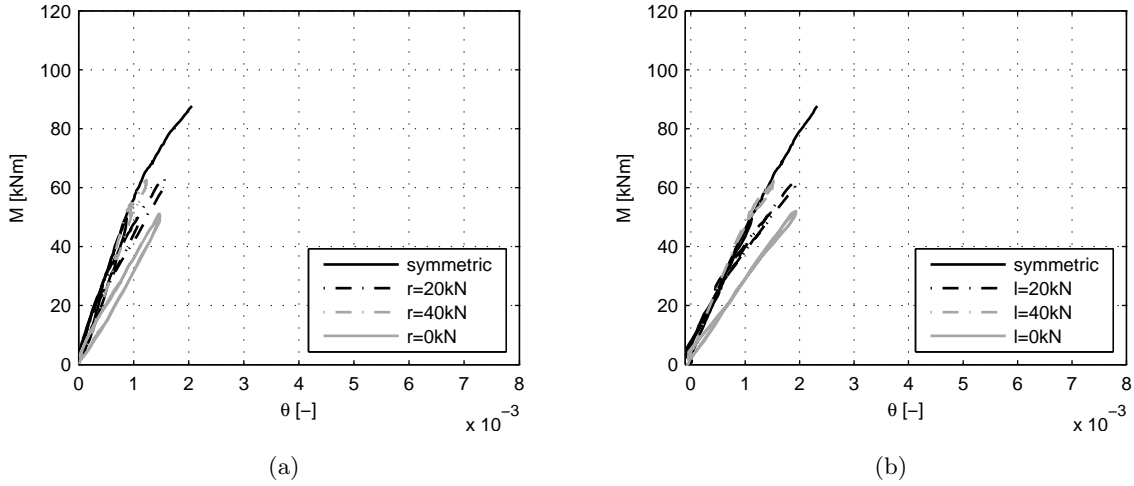
Figure 4.10: 4.10(a): Test evaluation for a high tendon force with a constant load on the right beam
4.10(b): Test evaluation for a high tendon force with constant load on the a left beam

4.5.2   Test with an intermediate tendon force

Initial compression

The initial compression for both beams can be estimated with the displacements measured at
the beam-column interface while applying the tendon force. The plots for both interfaces are
shown in Figure 4.11.

(a)   (b)
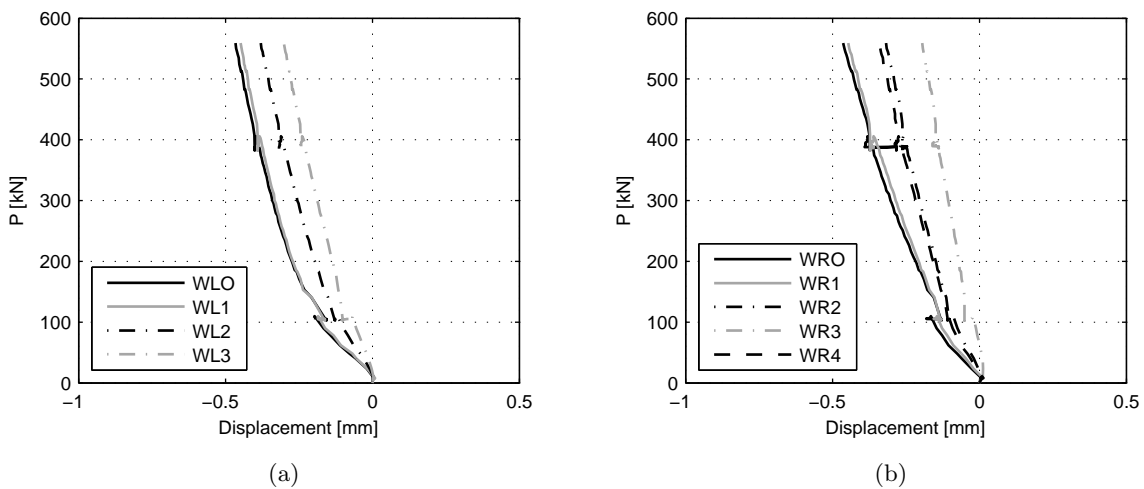
Figure 4.11: 4.11(b): Initial compression for a tendon force of 550 kN at the left interface 4.11(a):
Initial compression for a tendon force of 550 kN at the right interface

$$w_{comp,left} = 0.32 \text{ mm} \tag{4.11}$$

$$w_{comp,right} = 0.3 \text{ mm} \tag{4.12}$$

Evaluation symmetrical load case

Figure 4.12 shows plots off all the key variables as a function of the rotation θ.
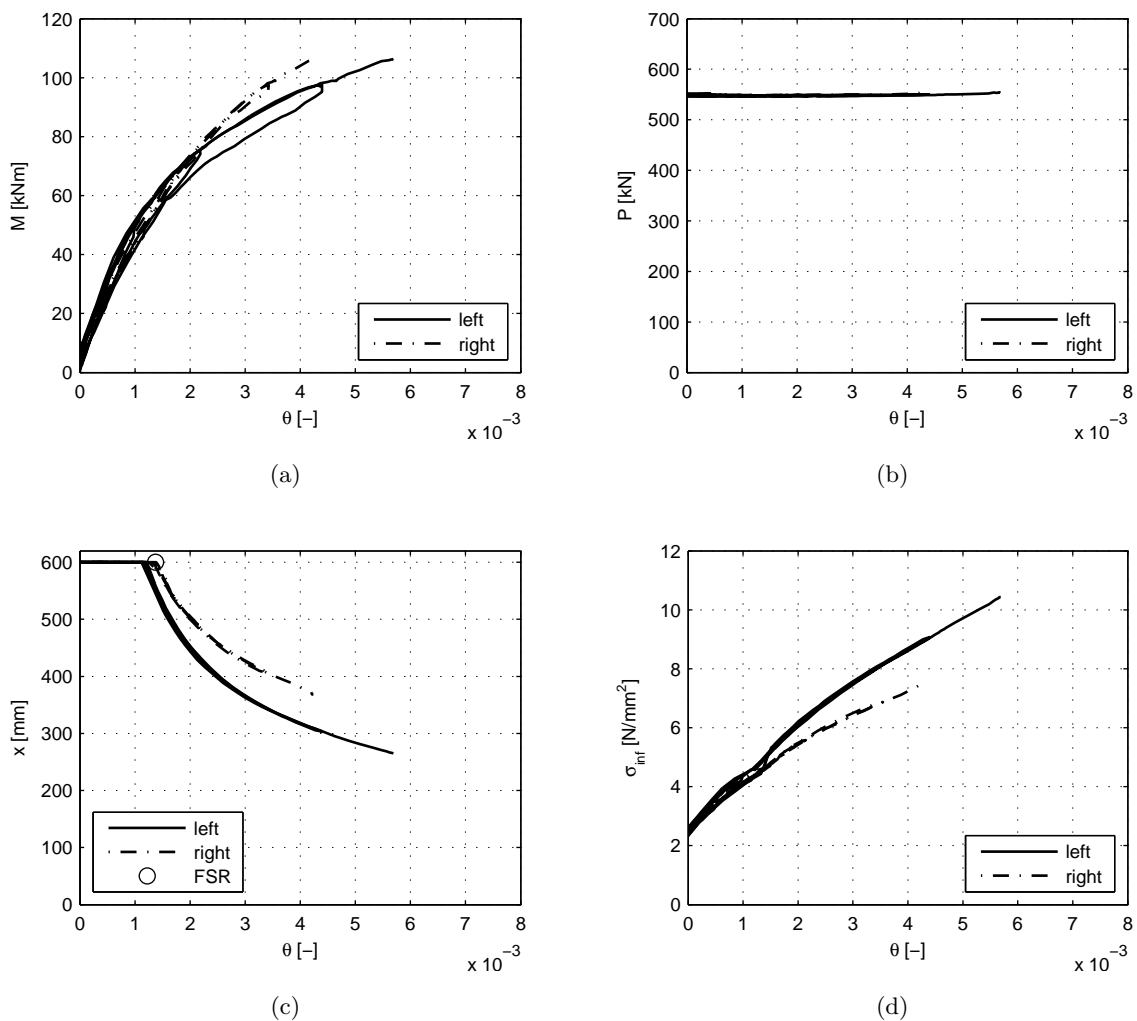
Figure 4.12: Evaluation of the symmetrical load case with intermediate tendon force 4.12(a): Moment-rotation behaviour 4.12(b): Tendon force 4.12(c): Neutral axis depth 4.12(d): Stresses at the interface

The moment-rotation diagram in Figure 4.12(a) shows, that the two connections behave similarly until the moment in the interface reaches a value of approximately 80 kNm. The two sides behave differently after that; the right connection shows a stiffer behaviour, whereas the left connection

is softer.

The tendon force remains constant during the test (Figure 4.12(b)) up to a rotation of 5 mrad, where a slight increase is noticeable.

The neutral axis depth is constant at a value of 600 mm, up to a rotation of 1.1 mrad as can be seen in Figure 4.12(c). Then it starts to decrease, which means that the moment of decompression is approximately 50 kNm at a rotation of 1.1 mrad. With a feeler gauge a gap could be noticed at a load of 48 kN, which corresponds to a moment of 60 kNm. The circle in the diagram shows the moment of decompression according to the pressure sensor (FSR) for the right interface. The comparison shows, that the decompression happens later than estimated with the LVDTs.

The stresses reach nearly 11 MPa, which is outside the estimated elastic range (Figure 4.12(d)). However, no plastic deformations could be observed after the test.

Evaluation asymmetrical load case

Also with an intermediate tendon force, the initial stiffness of the connection reduces with with decreasing load on the other beam due to the shear deformations in the column as can be seen in Figures 4.13(a) and 4.13(b).

(a)   (b)
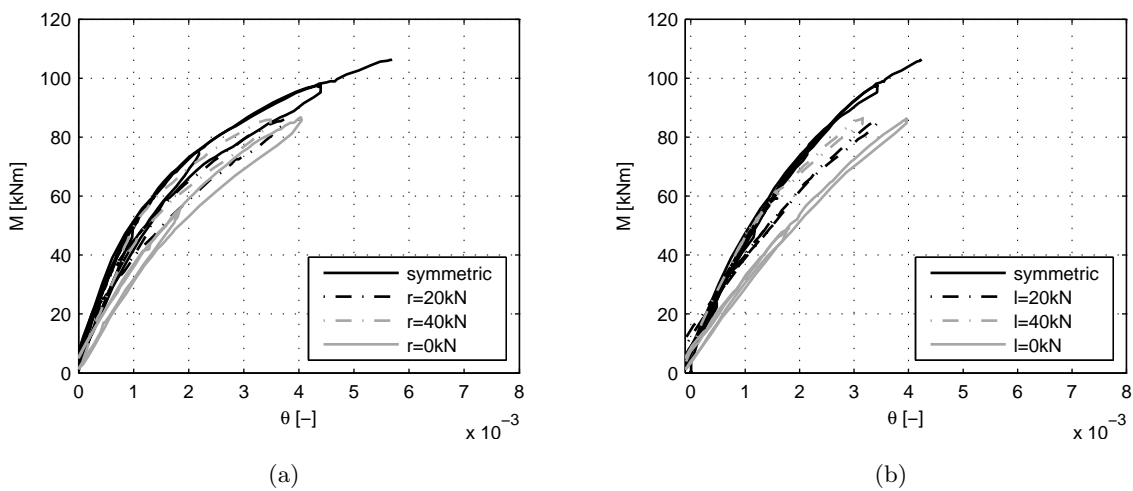
Figure 4.13: 4.13(a): Test evaluation for an intermediate tendon force with a constant load on the right beam 4.13(b): Test evaluation for an intermediate tendon force with a constant load on the left beam

4.5.3   Test with low tendon force

Initial compression

The initial compression is estimated for both interfaces separately with the LVDTs mounted on the beam column interface (Figure 4.14).
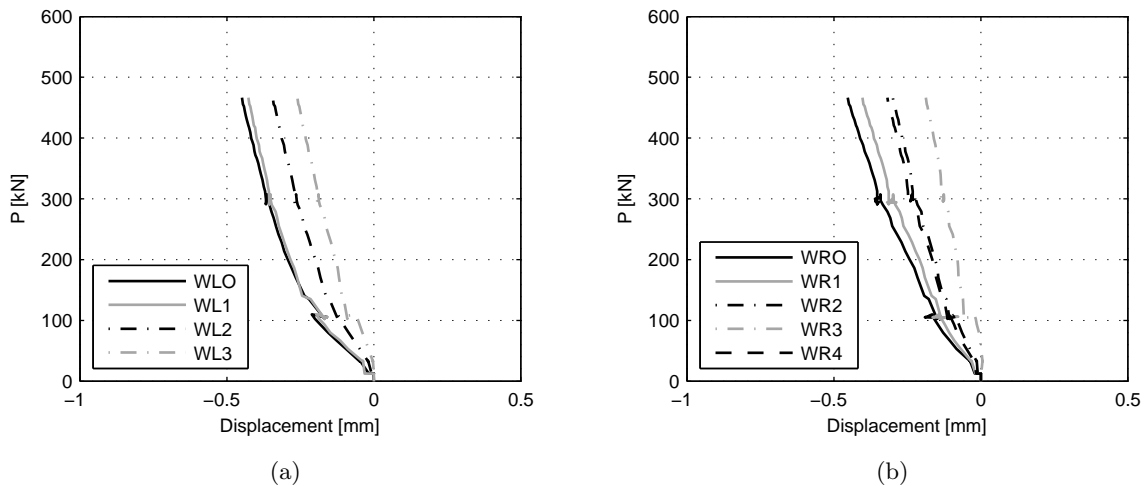
Figure 4.14: 4.14(b): Initial compression for a tendon force of 450 kN at the left interface 4.14(a): Initial compression for a tendon force of 450 kN at the right interface

The values for the two interfaces are:

$$w_{comp,left} = 0.27 \text{ mm} \tag{4.13}$$

$$w_{comp,right} = 0.28 \text{ mm} \tag{4.14}$$

Evaluation symmetric load case

Figure 4.15 shows plots off all the key variables as a function of the rotation θ.

The moment-rotation diagram shows that the two connections behave similar until the moment in the interface reaches a value of approximately 60 kNm (Figure 4.15(a)). The two sides behave differently after that; the right connection shows a stiffer behaviour, whereas the left connection softens with increasing moment. This phenomenon could be observed best for low tendon forces [69] and got smaller as the tendon forces increased.

The tendon force remains constant during the test as seen in Figure 4.15(b). The beginning of an increase is noticeable at a rotation of 4 mrad.

The neutral axis depth is constant at a value of 600 mm up to a rotation of 1.0 mrad (Figure 4.15(c)). Then it starts to decrease, which means that the moment of decompression is at 1.0 mrad. With the feeler a gap was noticed at a load of 32 kN, which corresponds to a moment
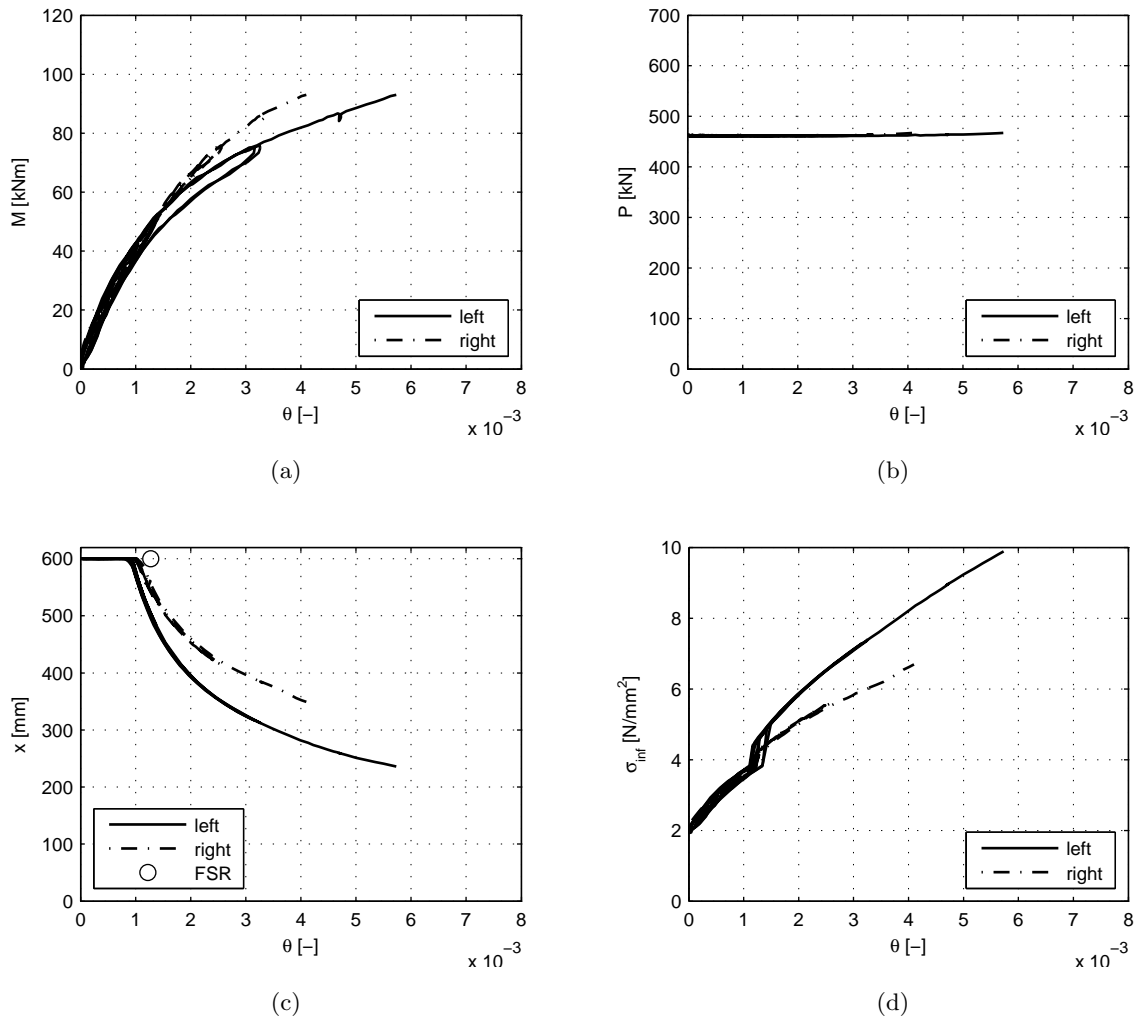
Figure 4.15: Evaluation symmetric load case with low tendon force 4.15(a): Moment-rotation behaviour 4.15(b): Tendon force 4.15(c): Neutral axis depth 4.15(d): Stresses at the interface

of 40 kNm. The circle in the diagram shows the moment of decompression according to the pressure sensor for the right interface (FSR).
The stresses reach 10 MPa (Figure 4.15(d)), which is slightly above the elastic range regarding the codes [62].

Evaluation asymmetrical load case

It can be seen from the moment-rotation-diagram (Figure 4.16(a) and 4.16(b)), that the initial stiffness of the connection reduces with decreasing load on the other beam due to the shear deformations and the resulting additional rotation.
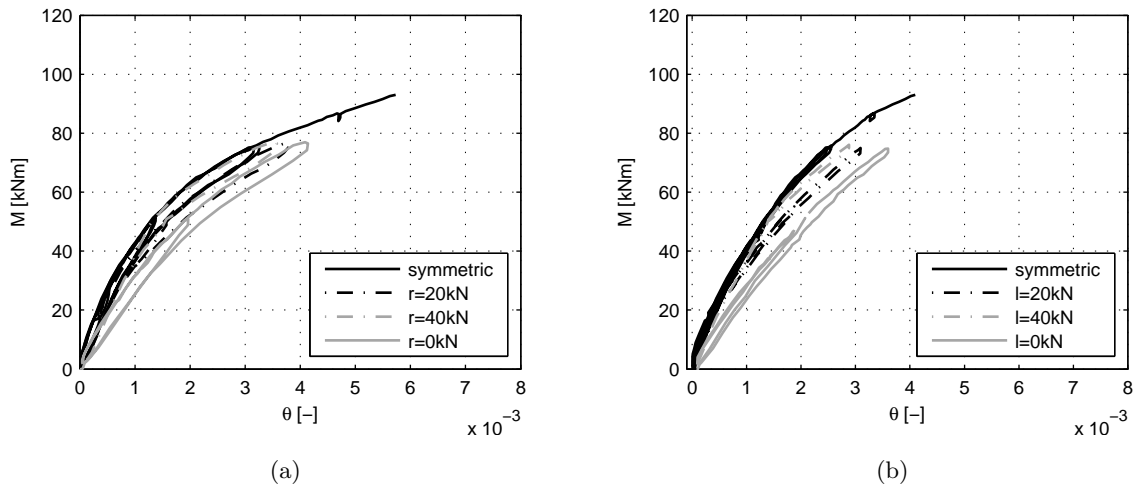
Figure 4.16: 4.16(a): Test evaluation for an intermediate tendon force with a constant load on the right beam 4.16(b): Test evaluation for an intermediate tendon force with a constant load on the left beam

4.5.4 Test with a high load level

Rotation

The rotations during test 22 reached very large values compared to all other tests due to the high load level (test up to failure). The LVDTs at the beam-column interface had to be re-adjusted and some of them reached the limit of their measuring range. This was not noticed during the test, which means that the rotations can not be estimated from the LVDTs. Therefore, the rotations for test 22 are estimated from the inclinometers.

Evaluation

Figure 4.17 shows plots off all the key variables as a function of the rotation θ.
The two beams seem to show a hysteretic behaviour in the moment-rotation-diagram (different loading and unloading path as can be seen in Figure 4.17(a)). Since nearly no plastic deformations occurred during the test, only little energy was dissipated. Some of the hysteretic behaviour can be attributed to a loss in post-tensioning force during the test, whereas the rest of the hysteretic behaviour is due to energy absorption in the column. Due to elongation of the tendon, the post-tensioning force increases, which also leads to an increase in oil pressure in the hydraulic system. This leads to an increase in loss of hydraulic fluids since some leakage occurs in the valves, so that the pressure and therefore the tendon force are deteriorating. The tendon force at the beginning of the test is 557 kN, at the end 510 kN.
The tendon force increases at a rotation of 6 mrad (Figure 4.17(b)). The gap reaches the position of the tendon and therefore elongates it as the load is increased. This elongation leads to an increase in the tendon force. The force climbs up to 750 kN, where the test was stopped in order to prevent the tendon from failing.
The neutral axis depth is constant at a value of 600 mm up to a rotation of 1.2 mrad as seen
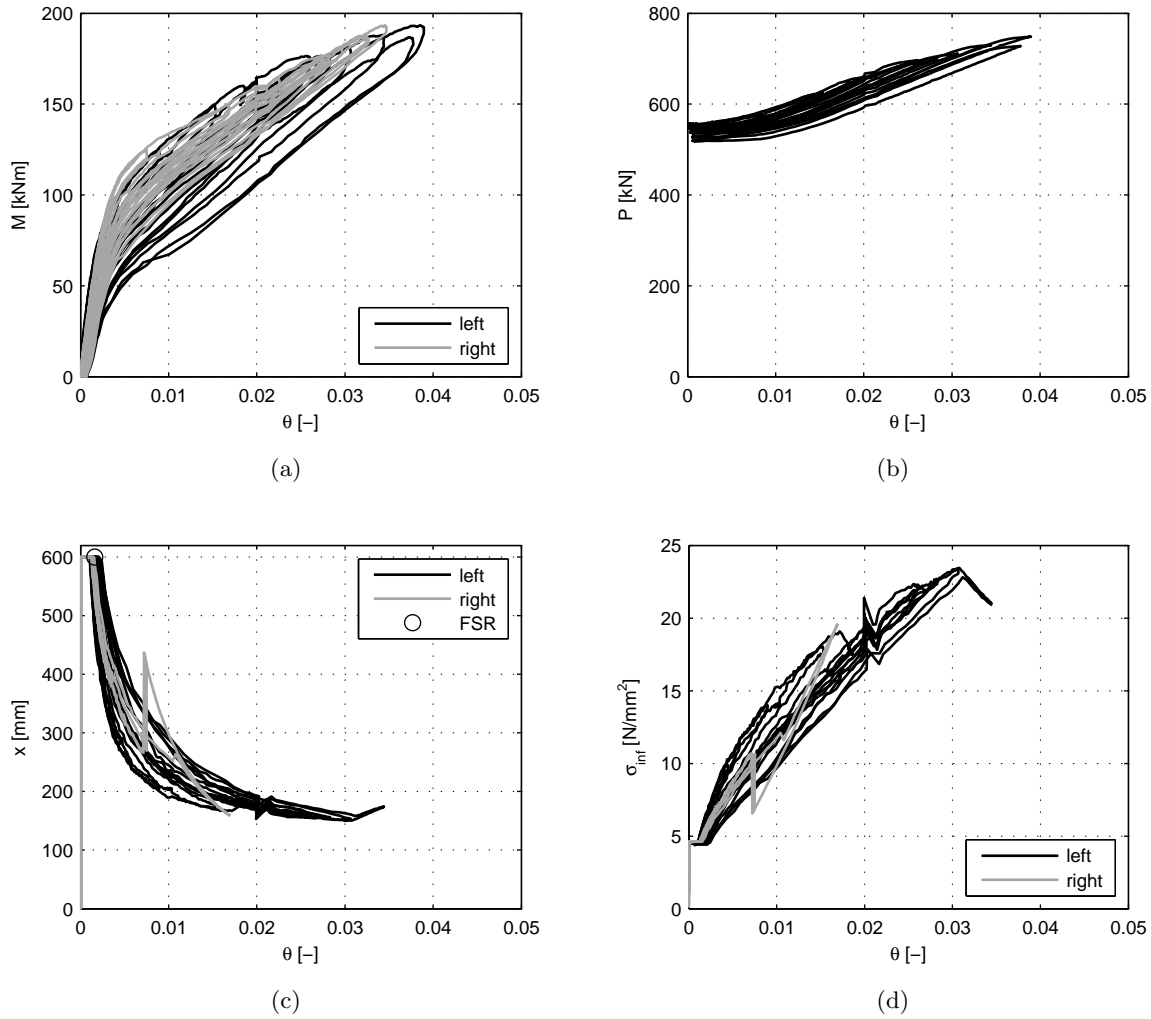
Figure 4.17: Evaluation of the symmetrical load case with high load level 4.17(a): Moment-rotation behaviour 4.17(b): Tendon force 4.17(c): Neutral axis depth 4.17(d): Stresses at the interface

in Figure 4.17(c). Then it starts to decrease, which means that the moment of decompression is approximately 50 kNm at a rotation of 1.2 mrad. The compression zone gets smaller than 300 mm, which means that the gap reaches the position of the tendon. This observation could also be made by evaluating the tendon force. For the right beam the range of altered data is noticeable; a discontinuity develops at approximately 20 mrad. Furthermore, the left beam shows an incorrect behaviour concerning the neutral axis depth x, which starts to increase from a rotation of 30 mrad, which is physically not possible. This phenomena is due to the error in the LVDTs (out of range).

The stresses exceed 20 MPa (Figure 4.17(d)), which is not in the expected elastic range any more. The plastic deformations measured after the test are very small though, each beam had residual deformations of 2 mm. Large leaps are noticeable for both interfaces. For the left interface it is due to the fact that of some LVDTs were out of range, at the right interface it is due to the alteration of the data, which is very sensitive regarding the stresses.

4.6 Comparison tests and analytical model

The model introduced in Chapter 3 is applied with the following parameters:

- Young's modulus perpendicular to the grain $E_{90} = 860$ MPa

- Shear modulus $G_c = 810$ MPa

- Load distribution factor $\Delta = 0$

4.6.1 Test with a high tendon force

Figure 4.18 shows the test results and the model prediction for a test with a high tendon force of 680 kN.
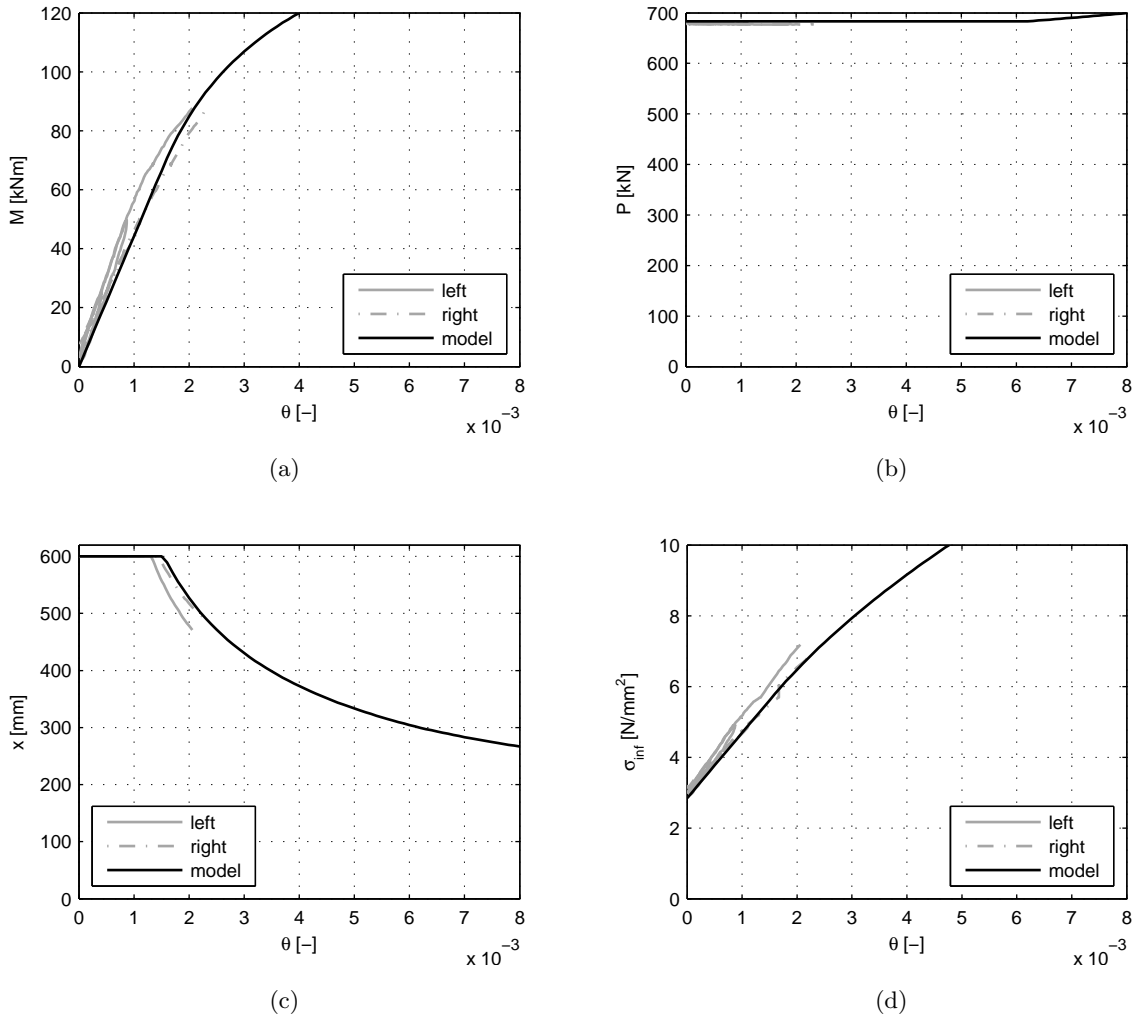
Figure 4.18: Test results and analytical model prediction for the load case with a high tendon force 4.18(a): Moment-rotation behaviour 4.18(b): Tendon force 4.18(c): Neutral axis depth 4.18(d): Stresses at the interface

All key variables can be predicted accurately, especially for the right interface, i.e. the moment-rotation behaviour (Figure 4.18(a)) the tendon force (Figure 4.18(b)), the neutral axis depth (Figure 4.18(c)) and the stresses (Figure 4.18(d)).

Figure 4.19 shows the test results and the analytical prediction for the asymmetrical load case. The moment-rotation behaviour fits for the right interface (Figure 4.19(b)), whereas the left interface is predicted too soft (Figure 4.19(b)).

<center>(a)   (b)</center>
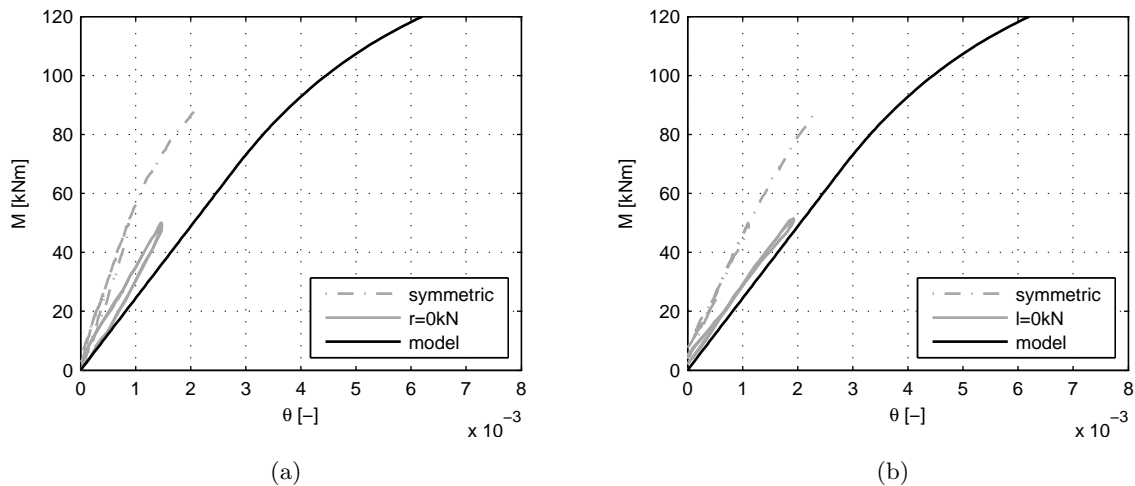
Figure 4.19: Test results and analytical model prediction for a high tendon force 4.19(a): Constant load on the right beam 4.19(b): Constant load on the left beam

4.6.2   Test with an intermediate tendon force

Figure 4.20 shows the test results and the model prediction for a test with an intermediate tendon force of 550 kN.

The analytical solution matches the test results reasonably well. The initial stiffness according to the model compared to the test results is overestimated slightly (Figure 4.20(a)). However, the analytical solution seems to match the stiffer behaviour of the right interface better than the softer behaviour from the left interface. The tendon force matches the model, even the slight increase beginning at a rotation of 5 mrad could be predicted as can be seen in Figure 4.20(b). The neutral axis depth and the moment of decompression are predicted accurately as shown in Figure 4.20(c). The stresses are also modelled well for both interfaces, whereas the model prediction lies between the values experienced by the two interfaces (Figure 4.20(d)).

Figure 4.21 shows the test results and the analytical prediction for the asymmetric load case. The moment-rotation behaviour is well predicted for both interfaces, whereas the initial stiffness is predicted to low.
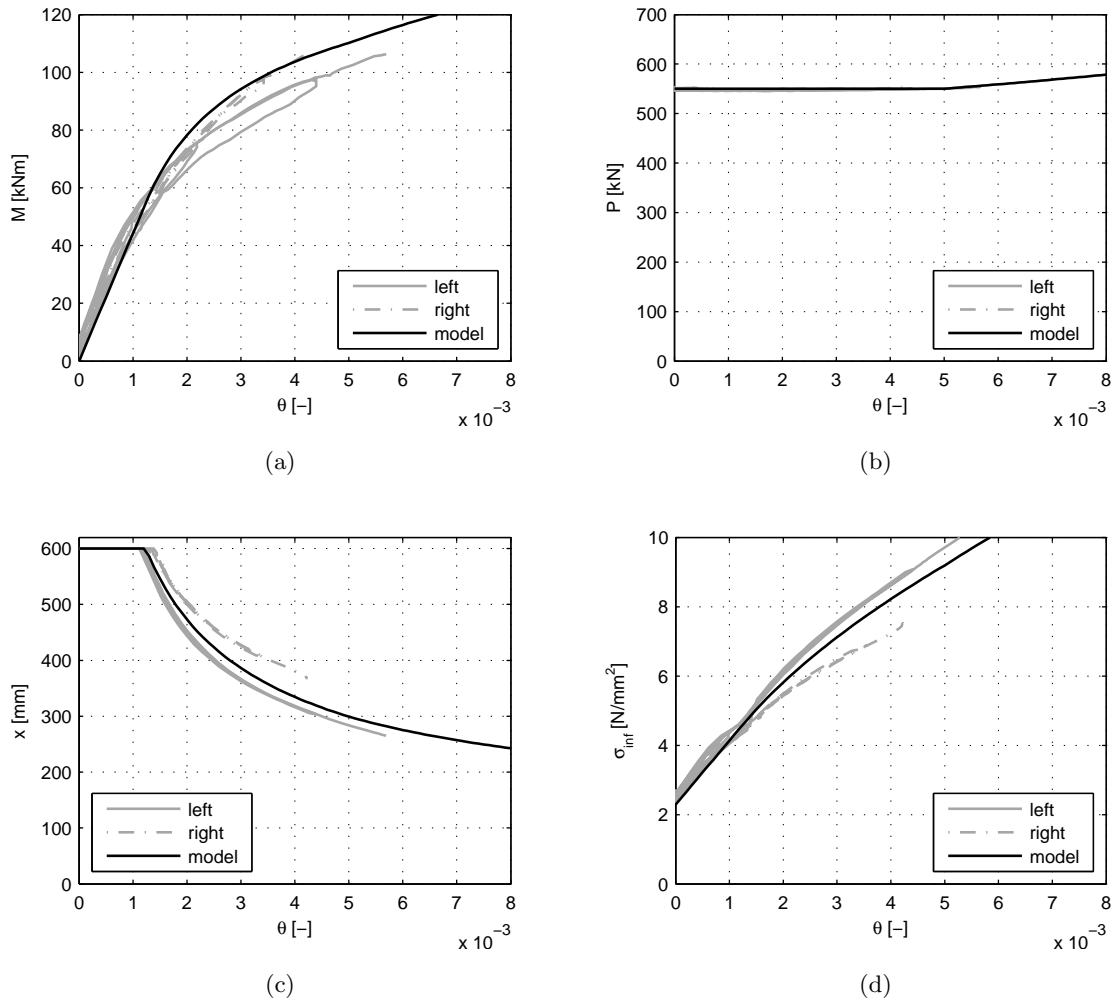
Figure 4.20: Test results and analytical model prediction for the load case with an intermediate tendon force 4.20(a): Moment-rotation 4.20(b): Tendon force 4.20(c): Neutral axis depth 4.20(d): Stresses
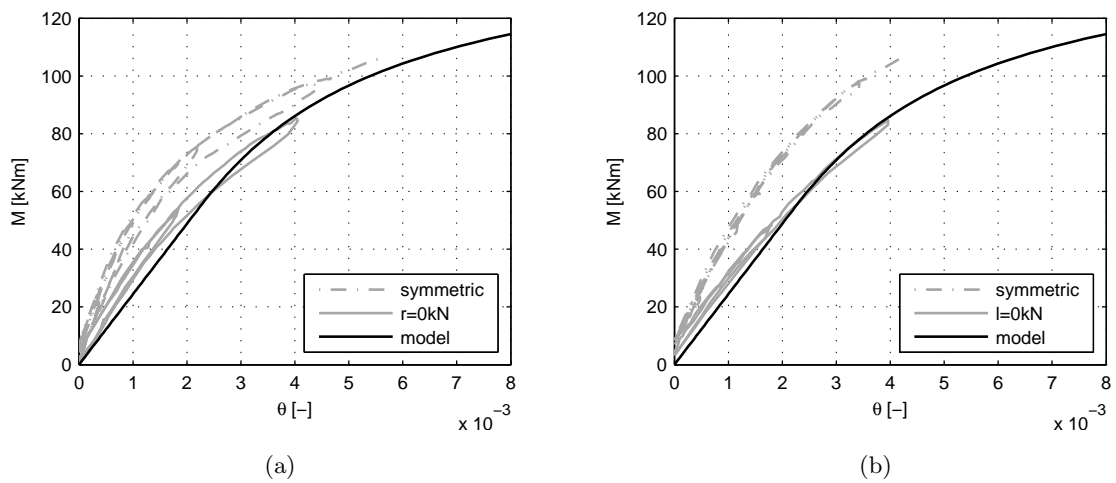
Figure 4.21: Test results and analytical model prediction for an intermediate tendon force 4.21(a): Constant load on the right beam 4.21(b): Constant load on the left beam

4.6.3 Test with a low tendon force

Figure 4.22 shows the test results and the model prediction for a test with a low tendon force of 450 kN.
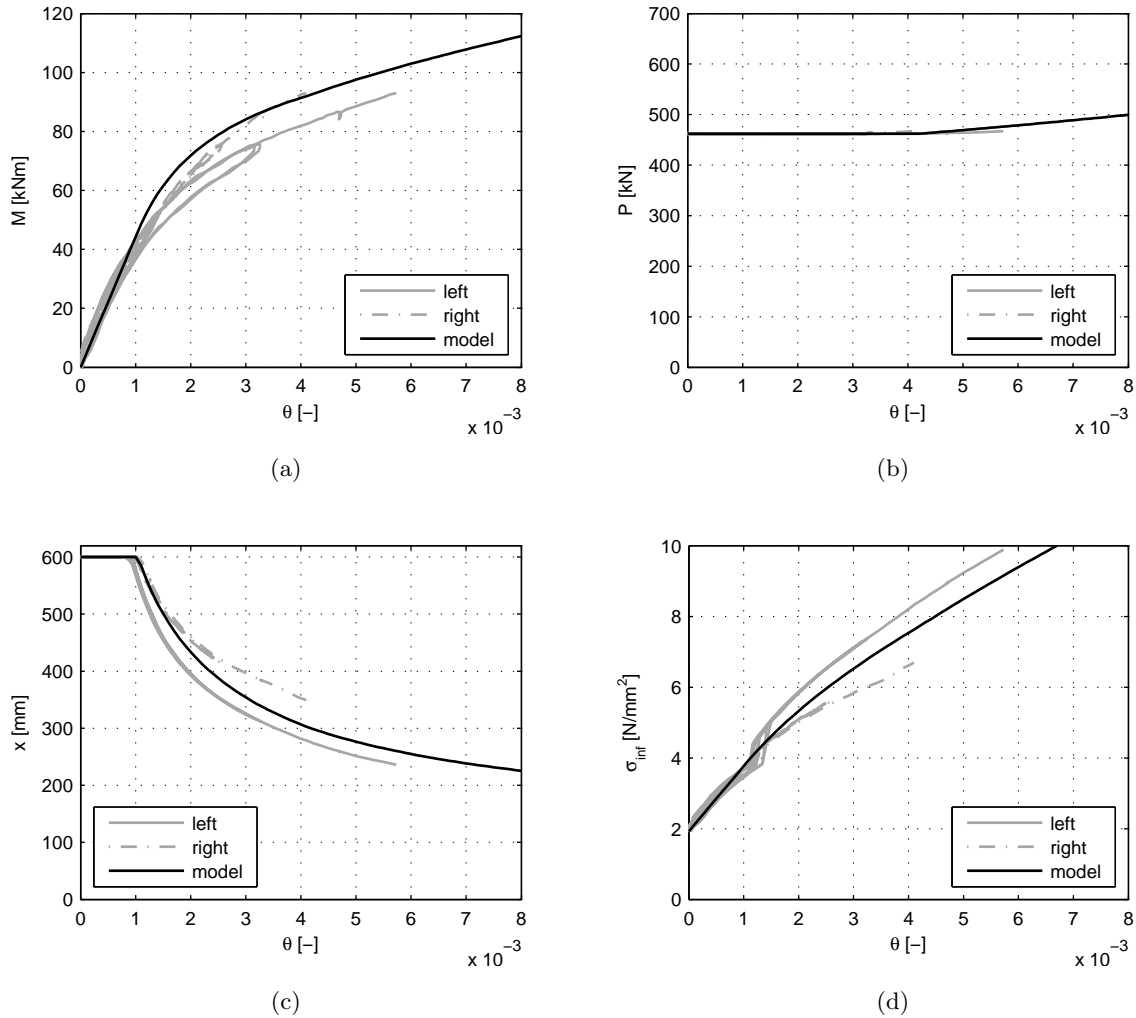
Figure 4.22: Test results and analytical model prediction for the load case with a low tendon force 4.22(a): Moment-rotation behaviour 4.22(b): Tendon force 4.22(c): Neutral axis depth 4.22(d): Stresses at the interface

The analytical solution matches the test results reasonably well. The initial stiffness from the model and the test results are nearly identical as can be seen in Figure 4.22(a). However, the model shows a stiffer behaviour than the tests for moments higher than 40 kNm. This means that the design would be on the unsafe side for moments larger than 40-50 kNm. Here to, the analytical solution seems to match the stiffer behaviour of the right interface better than the softer behaviour of the left interface. The tendon force as well as its increase is predicted well (Figure 4.22(b)). The neutral axis depth (Figure 4.22(c)) calculated by the model lies between the test results obtained from the two interfaces. However, the moment of decompression is determined accurately, as are the stresses (Figure 4.22(d)).

Figure 4.23 shows the analytical and experimental results for the asymmetrical load case. The moment-rotation behaviour is predicted accurately for both interfaces (Figures 4.23(a) and 4.23(b)). The model estimates a too high stiffness for larger moments in the left interface, which was already observed for the symmetric load case.

(a)   (b)
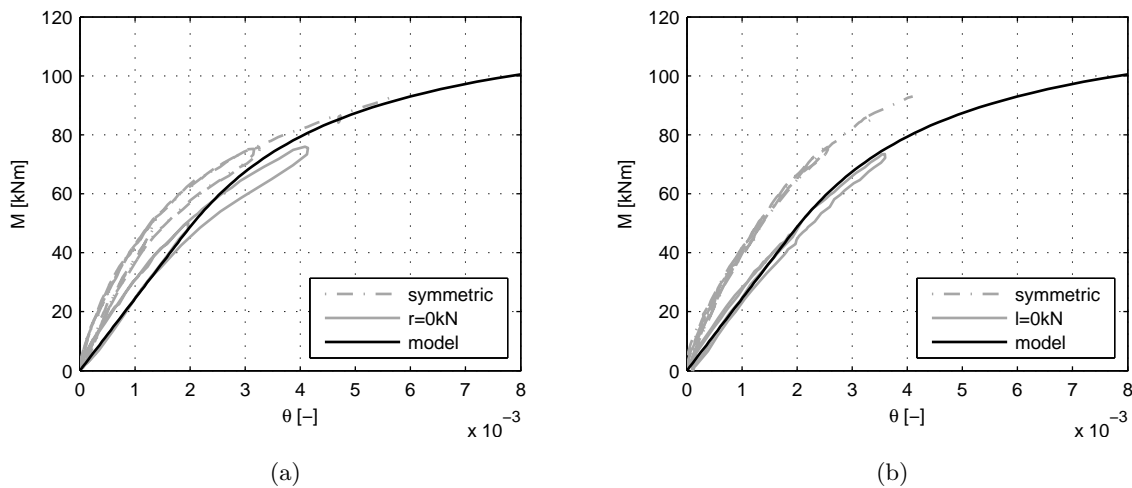
Figure 4.23: Test results and analytical model prediction for a low tendon force 4.23(a): Constant load on the right beam 4.23(b): Constant load on the left beam

4.6.4   Test with a high load level

Figure 4.24 shows the comparison between the results from the analytical model and from the test with the higher load level, where an increase of tendon force occurred as the gap reaches the tendon.

The model fits reasonably well to the test data. The modelled behaviour is rather stiff compared to the tests, as can be seen in Figure 4.24(a) particularly for higher moments. This is mainly due to the fact that the model does not take any grain crushing in the column into account, which occurs during the tests (a residual deformation of 2 mm was measured under the beams, which corresponds to an additional rotation of 1.6 mrad). For the case where tendon elongation occurs, the differences between the model and the test become noticeable (Figure 4.24(b)). On the one hand, the model takes the elongation of the tendon into account thus an increase in the tendon force is visible in the test as well as in the model. On the other hand, the increase according to the model is higher than during the test. Therefore, the model describes a stiffer structural behaviour of the beam-column connection than the actual behaviour of the connection, as can be seen in the moment-rotation diagram. The neutral axis depth was predicted well, even for larger rotations (Figure 4.24(c)). The stresses are also in coherence with the test results (Figure 4.24(c)) but exceed the elastic range.

One possible reason for the difference between the model and the tests is that the model does not take the plastic deformations of timber subjected to compression perpendicular to the grain into
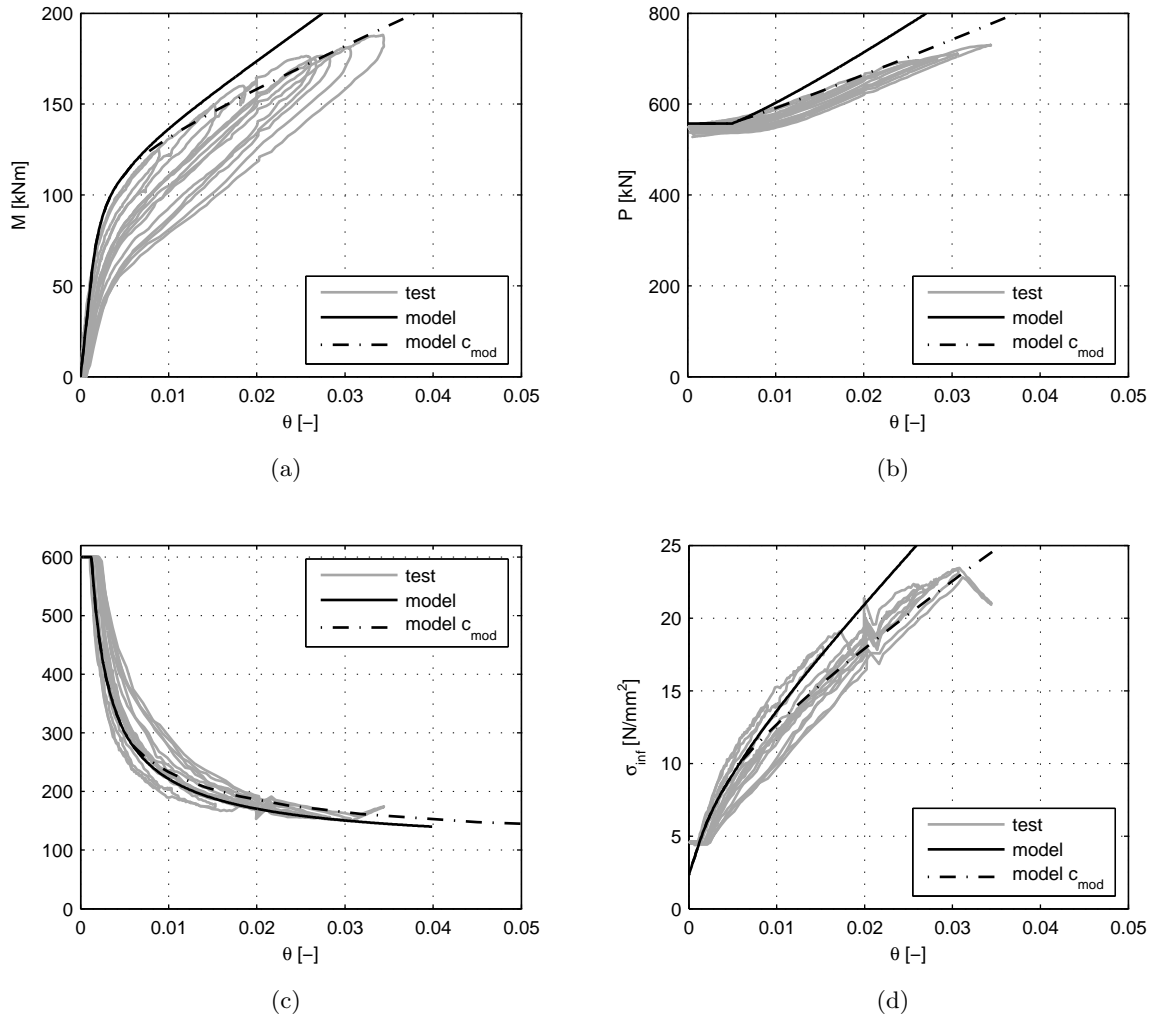
Figure 4.24: Test results and analytical model prediction for a load case with high loads 4.24(a): Moment-rotation behaviour 4.24(b): Tendon force 4.24(c): Neutral axis depth 4.24(d): Stresses at the interface

account. However, plastic deformations were observed during the test (a residual deformation of 2 mm was measured under the beams, which corresponds to an additional rotation of 1.6 mrad). A further possible reason is that the tendon may have some space to move, since the hole in the specimen is larger than the tendon itself. The stresses reach values far above the elastic range of the column, therefore a softening behaviour should be taken into account.

Figure 4.24 also shows the results obtained with the modified spring coefficient c_{mod}. The spring constant is reduced as soon as the maximal stresses in the interface reach a value of 10 MPa, i.e. the original value for the spring c is used if the stresses are smaller than 10 MPa whereas the modified value c_{mod} is used for stresses over 10 MPa. The value for c_{mod} was set to 3.8 N/mm^3 whereas the modulus of subgrade reaction c up to 10 MPa is 6.1 N/mm^3, calculated according to Equation (3.2).

4.7 Experimental analysis - discussion

4.7.1 Initial stiffness

The initial stiffness K_I is defined as the stiffness up to the moment when decompression sets in (see Figure 4.25). This stiffness can be calculated with a secant between a Moment of 1 kNm and the moment of decompression for the first load cycle with $M > M_{dec}$:

$$K_I = \frac{M_{dec} - 1kNm}{\theta_{M_{dec}} - \theta_{M=1kNm}} \tag{4.15}$$
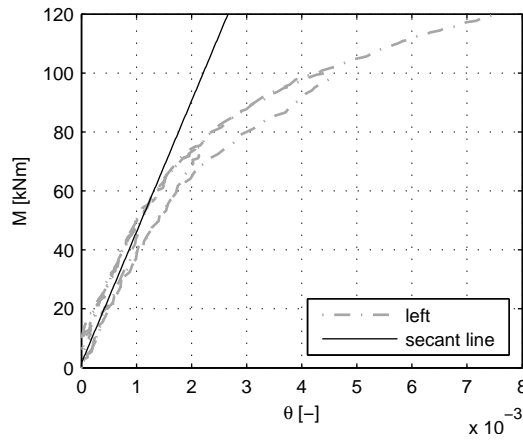
Figure 4.25: Definition initial stiffness

Table 4.5 shows the values for the initial stiffness for all tests.

Table 4.5: Initial stiffnesses for all tests

Test No.	M_{dec} [kNm]	$K_{I,left}$ [kNm/rad]	$K_{I,right}$ [kNm/rad]	K_I [kNm/rad]
No. 13	51.8	39941	34448	37195
No. 14	41.6	35441	33678	34560
No. 15	61.2	46817	40236	43527
No. 16	32.5	28427	34813	31620
No. 17	68.3	50339	40359	45349
No. 18	56.0	43934	35361	39648
No. 20	46.2	39010	38783	38897
No. 21	55.4	44325	39011	41668
No. 22	55.7	44502	35434	39968

Analytically, the stiffness can be modelled by using a rotational spring. Based on Hooke's law the rotational spring is defined as:

$$M = \kappa \cdot \theta \tag{4.16}$$

Whereas κ is the spring constant [kNm/rad]. By combining Equation (4.16) with Equation (3.9), a new expression can be derived for the spring constant:

$$M = \kappa \cdot \theta = c \cdot \frac{b_b \cdot h_b^3}{12} \cdot \theta = c \cdot I_b \cdot \theta \tag{4.17}$$

The spring constant is a function of the moment of inertia of the beam and the modulus of subgrade reaction. According to Equation (4.17), the tendon force does not influence the stiffness (note that the modulus of subgrade reaction is only a function of the geometry and the elastic properties of the column). However, the values obtained from the tests listed in Table 4.5 and plotted in Figure 4.26 as a function of the tendon force show that the stiffness is strongly dependent on the tendon force.
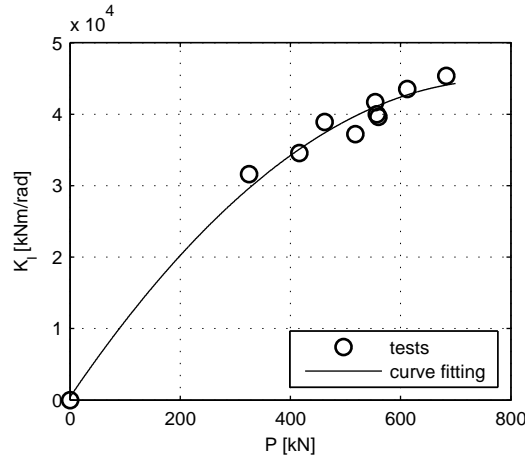
Figure 4.26: Influence of the tendon force on the stiffness with fitted curve

The data points (test results) can be approximated by a curve, while assuming that the stiffness of the connection is equal to zero, if no tendon force is applied. The slope of the curve seems to decrease with increasing tendon force, leading to the assumption that the curve converges to an ultimate value.

This would also correspond to Equation (4.17), which suggests that only one value exists for the stiffness, which is independent from the post-tensioning force. This value can be interpreted as the maximal stiffness that can be achieved with the assumed material properties:

$$K_{I,max} = c \cdot \frac{b_b \cdot h_b^3}{12} = 6.14 \cdot \frac{400 \cdot 600^3}{12} = 44208 \text{ kNm/rad} \tag{4.18}$$

This value could be achieved during the tests with the highest tendon force (680 kN). The evaluation shows that for small tendon forces it is not possible to activate the calculated stiffness according to Equation (4.18). A factor $K_I/K_{I,max}$ is introduced (see Table 4.6), which divides

the experimentally obtained stiffness by the theoretical stiffness and therefore indicates, how much of the maximally possible stiffness was activated.

Table 4.6: Stiffness and activation of stiffness

Test No.	P [kN]	M_{dec} [kNm]	K_I [kNm/rad]	f_P
No. 13	518	51.8	37195	0.84
No. 14	416	41.6	34560	0.78
No. 15	612	61.2	43527	0.98
No. 16	325	32.5	31620	0.72
No. 17	683	68.3	45349	1.03
No. 18	560	56.0	39648	0.90
No. 20	462	46.2	38897	0.88
No. 21	554	55.4	41668	0.94
No. 22	557	55.7	39968	0.90

With smaller tendon forces, less stiffness is activated, since the beam is not being pressed tightly against the column. However, the value increases rapidly from P=325 kN to P=518 kN. Therefore, the cases with lower tendon forces need to bis discussed more in depth. The analytical model uses the theoretical stiffness from Equation (4.18), which means that the model can only predict tests with a higher tendon force accurately.

In order to obtain 80% of the calculated stiffness, the force in the tendon would need to be approximately 400 kN. This would correspond to an initial stress of 2.1 MPa (see Figure 4.27). This procedure allows the definition of a lower limit for the tendon force, which can be considered as the minimal force needed for a post-tensioned timber connection including the losses in tendon force.
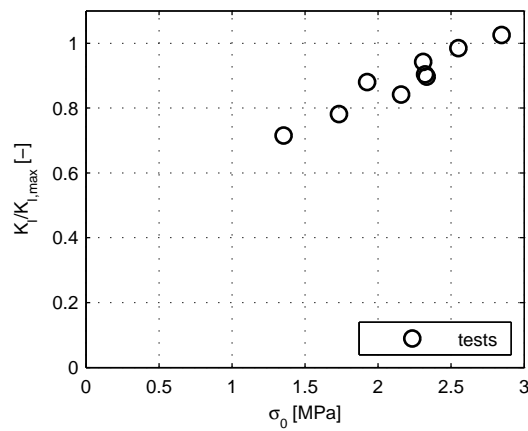
Figure 4.27: Obtained stiffness normalized with maximal stiffness for different initial stresses due to pre-stressing

4.7.2   Defining the level of post-tensioning

The lower limit was already introduced in the previous subsection. If an optimal post-tensioning force has to be defined, the upper limit for the tendon force has to be estimated as well. To do so, the decisive criterion for design has to be defined. For the connection the following two criteria could control the design:

- Compression perpendicular to the grain

- Tendon force

All tests indicated however, that the maximal stress perpendicular to the grain controls the design. The major problem is, that the strength values for timber perpendicular to the grain are very small (see Table 4.1). During the tests, stresses up to 15 Mpa were achieved without observing any grain crushing in the column at all. Moreover, if grain crushing occurs, there will be no failure in the classical sense.
The strength can be increased by taking a load distribution in the column into account. Assuming a load distribution of 1:1 (see [68] and also Figure 3.3) the value can be increased with:

$$f_{c,90,k} = 1.5 \cdot 8.6 = 13 \text{ MPa} \tag{4.19}$$

This value is also in agreement with the compression tests that were performed in order to estimate the modulus of subgrade reaction [67].

With the analytical model (Equations (3.12) and (3.15)) it is possible to calculate the occurring rotation when the stresses in the column correspond to its strength:

$$\theta_{max} = \frac{f_{c,90,k}^2 \cdot b_b}{2 \cdot P_0 \cdot c} \tag{4.20}$$

The allowable rotation decreases with increasing tendon force. Consequently, the load bearing capacity decreases as well.
For a given rotation the moment in the connection increases with increasing tendon force, which stands in contradiction to the allowable rotation. The maximal moment can be calculated with Equations (3.15) and (4.20):

$$M_{max} = P_0 \cdot \left(\frac{h_b}{2} - \sqrt{\frac{2}{9} \cdot \frac{P_0}{b_b \cdot c \cdot \theta_{max}}} \right) = P_0 \cdot \left(\frac{h_b}{2} - P_0 \cdot \frac{2}{3} \cdot \frac{1}{b_b \cdot f_{c,90,k}} \right) \tag{4.21}$$

Both, Equations (4.20) and (4.21), depend on the tendon force. Since they stand in contradiction there should be a value for the tendon force, where the moment curve and the rotation curve intersect. This value can be found by plotting the two equations against the tendon force (Figure 4.28).
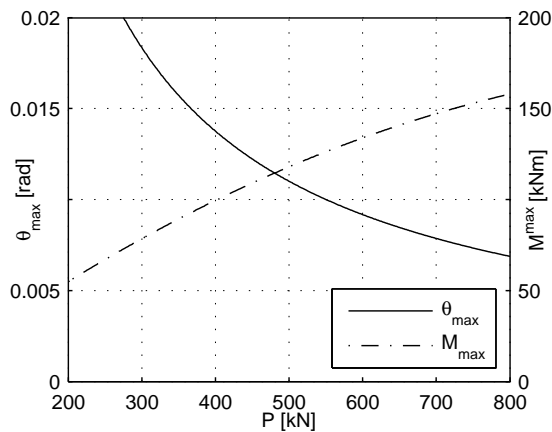
Figure 4.28: Optimal tendon force

4.7.3 Controlling parameters

The parameters controlling the design of a post-tensioned timber connection are the compression perpendicular to the grain of the column and the tendon force. The beam is not taken into account, since the span between the columns governs the design of the beam (the moment in the beam is a function of the span squared and the deflections are a function of the span to the power of four). If the two parameters are examined, the following observations can be made:

- The strength perpendicular to the grain is the most important factor, since it is squared in Equation (4.20).

- The allowable rotation also depends on the tendon force, but only as a linear function. This can easily be derived by rewriting Equation (3.18).

Increasing the maximal rotation is possible by increasing the width of the column and beam, or by increasing the strength of the column. This could be achieved by adding some reinforcement or using a different material, like laminated veneer lumber (LVL) made of beech, which is being investigated in an ongoing research project at ETH Zurich [72].

4.7.4 Position of the tendon

The position of the tendon has an influence on the structural behaviour of the connection as well. After decompression, when the gap has reached the position of the tendon, the latter begins to elongate which leads to an increase in stiffness as opposed to the case without tendon elongation (Figure 4.29).

Based on this observation it would be more favourable to change the position of the tendon when designing frames with post-tensioned timber connections for gravity loads, i.e. the tendon should be placed in the upper part of the beam, so that the elongation of the tendon already begins at a lower load level.

In contradiction to that, the tendon may not be exposed during a fire. The gap should therefore not have reached the tendon under the reduced load level during the duration of a fire. This
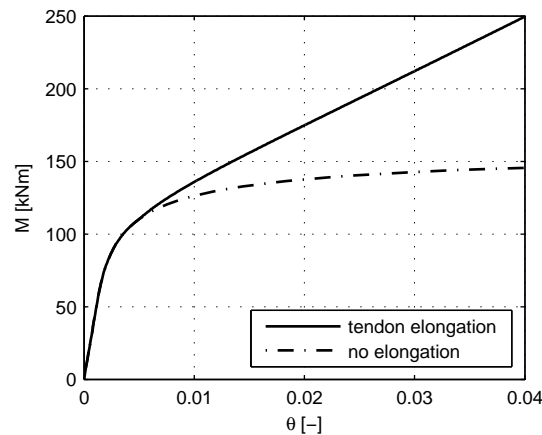
Figure 4.29: Moment-rotation behaviour with and without considering tendon elongation (from analytical model)

automatically means that the tendon should not be placed too close to the upper or lower edge of the beam.

4.7.5   Ash reinforcement

To check whether the ash reinforcement in the column is beneficial, a model prediction for a specimen with a column made of spruce was calculated. The dimension of the specimen is the same as for the actually tested specimen, with a column made of ash. The properties for the spruce column are summarised in Table 4.1. The comparison is shown in Figure 4.30. The reinforcement of the column with ash shows a much stiffer behaviour compared to the specimen with the column made of spruce. The stiffness up to the moment of decompression increases by a factor of approximately 3, as can easily be calculated with Equation (3.9).
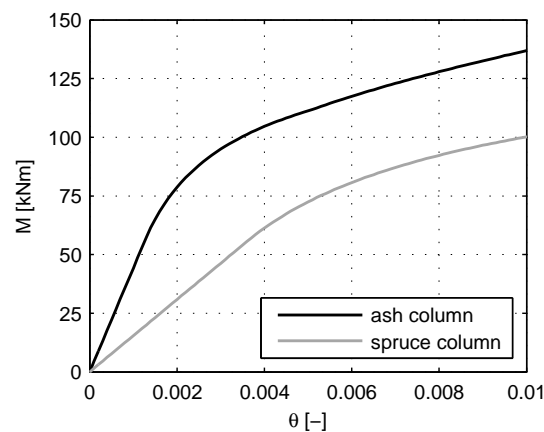
Figure 4.30: Comparison between the model prediction with an ash column and the model prediction for a connection with a column made of spruce

Moreover, the reinforcement with ash is also beneficial regarding the strength of the column, which increases from 3 MPa (spruce) to 8.3 MPa (ash).

Chapter 5

Pushover tests

In order to study the behaviour of post-tensioned timber structures under horizontal loading and to additionally validate the developed spring model for horizontal loads, a three bay post-tensioned timber frame has been investigated by performing several pushover-tests. The post-tensioned timber frame was subjected to horizontal loading up to 300 kN. The tests were performed with tendon forces varying from 200 to 700 kN. The tests showed that the connections at the outer columns differ from the connections at the inner ones and they also showed a favourable self-centering behaviour of the post-tensioned timber frame. The results obtained from the tests are compared with the results obtained from an analytical model, which has already been introduced in Chapter 3.

In addition to the pushover tests, some dynamic excitations were investigated as well, i.e. several tests with an impulse hammer were performed. These tests will only be mentioned briefly, since they were preliminary tests for the on-site investigations during the construction of the "ETH House of Natural Resources"[73]. An impulse hammer excitation will be discussed briefly, since the damping of the structure is needed for the preliminary seismic design described in Chapter 8.

5.1 Specimen and test setup

5.1.1 Specimen

The frame consists of three beams and four columns all made of glulam as shown in Figure 5.1. The glulam beams are made of Norway spruce (*picea abies*) except for the four lamellae at the beam-column interface, which are made of European ash (*fraxinus excelsior*). The columns are made entirely of European ash.

The dimensions of the beams are 6.12×0.72×0.28 m and the columns are 3.54×0.38×0.38 m. The hardwood (European ash) is required in areas, where high stresses perpendicular to the grain occur, namely in the connection between the column and the beam. The additional supports under the beam are for safety reasons and for the construction phase, where the tendon force is not yet applied to the specimen and the beams are therefore not connected to the columns.
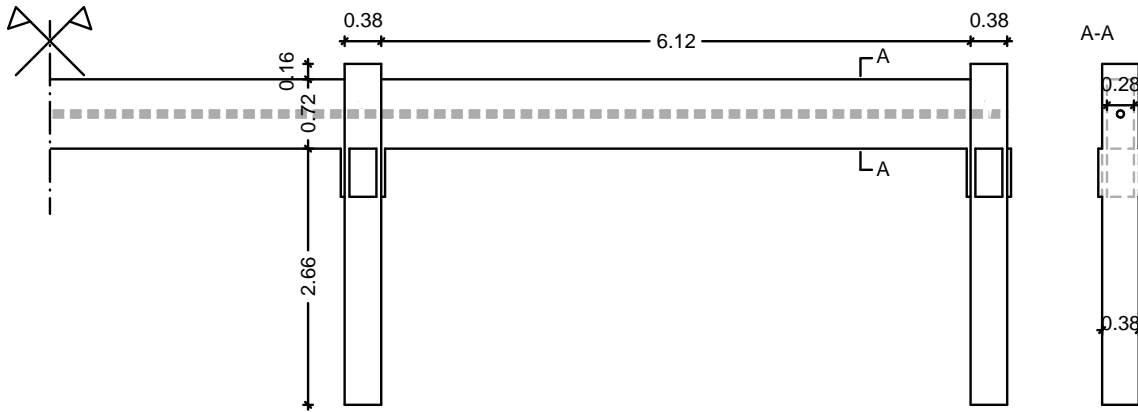
Figure 5.1: Test specimen with all dimensions in [m]

The assumed values for strength and stiffness of the materials are summarised in Table 5.1. The properties of the tendon are summarised in Table 5.2. The frame specimen is similar to the frame used in the design of the "ETH House of Natural Resources"[73].

A tendon is attached at either side of the frame. A thick steel plate is necessary at the end of the specimen for the load transmission from the tendon to the frame.

The shear forces between the beams and the columns are transferred via friction, whereas the supports are designed to be able to bear the shear forces in case the tendon force would drop unexpectedly.

Table 5.1: Strength and stiffness properties in [MPa] for strength grade GL24h [60] (beams) and D40 [62] (columns)

Abbreviation	Strength grade	
	GL24h	D40
$f_{c,0,k}$	22	26
$f_{c,90,k}$	3	8.3
E_0	11000	13000
E_{90}	300	860
G	500	810

Table 5.2: Tendon properties according to [70].

Abbreviation	Y1770 4-06
A_p	600 mm^2
L_p	4200 mm
E_p	197000 Mpa
$f_{p,k}$	1770 MPa

5.1.2 Test setup

All tests were performed at ETH Zurich on a strong floor as shown in Figure 5.2. The force is applied by two cylinders, which allow to apply a horizontal force of 300 kN on the specimen. The columns are connected to the strong floor with steel profiles and special supports. The supports were constructed in a way that allows the columns to rotate if necessary but also to constrain them. The pushover tests can therefore be performed with fixed and pinned column bases, respectively.

Between the timber columns, six large steel columns are positioned, which are connected to the strong floor (see Figure 5.2). Special supports are attached to each of these columns, which prohibit any movement perpendicular to the direction of the applied load.

Figure 5.2: Three-bay post-tensioned timber frame for pushover tests on the strong floor at the ETH Zurich

5.1.3 Measuring instrumentation

In order to investigate the structural behaviour of the post-tensioned timber frame under horizontal loading several types of measuring devices are being used:

- Linear variable differential transformers (LVDTs)

- Infra-red LEDs / optical 3D measurement system

- Inclinometers

- Hydraulic pumps

- Accelerometers

The LVDTs record the horizontal displacements of the two outer beams. The LVDTs are mounted in the middle of each beam and measure the deformation relative to one of the steel

columns fixed to the strong floor. The type of LVDTs used is the Precisor TK-100-E-2 with a range of 100 mm.

Several inclinometers of the type NS-5/P are positioned on top of each column and also on two beams (see Figure 5.3) and allow measuring the inclination relative to the horizon.
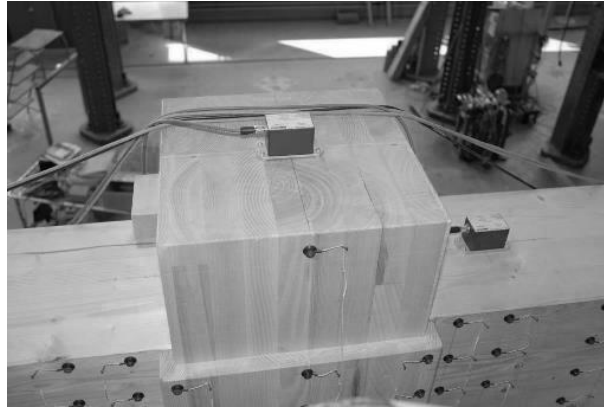
Figure 5.3: Inclinometers attached to the column and the adjacent beam

An optical 3D measurement system is used to measure the position of several infra-red LEDs attached at the beam-column interface of one outer and one inner column as shown in Figure 5.4. The system (NDI Certus HD) uses three cameras and is able to measure the position of each single LED (shown in Figure 5.4). The single LEDs are used to check the connection behaviour. The behaviour is crucial for the horizontal stiffness of the system and is also required to validate the analytical model introduced in Chapter 3. Due to the fact that only one camera was available, only one column could be evaluated during the test. In order to obtain a LED-measurement for each column, all tests had to be performed twice.
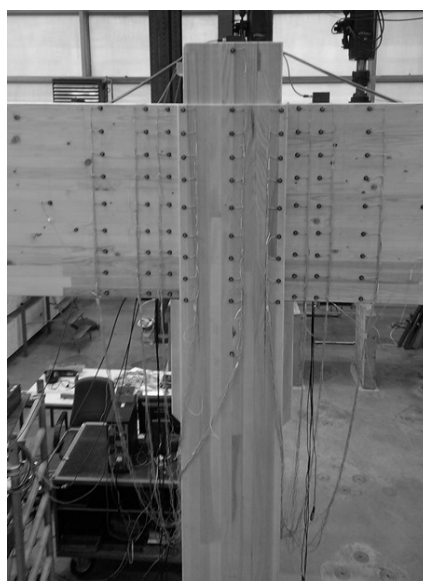
Figure 5.4: LEDs at the inner column. Each LED transmits its coordinates to a computer

Two pumps of the type Bieri HP 2.2 D-15110 are used during the tests. One pump is needed to pre-stress the tendon. The second one is used for horizontal loading.

The oil pressure is measured for each press separately. These values are necessary to calculate the forces in the cylinders and the tendon, respectively.

Several accelerometers of the type LIS344 were used for the preliminary dynamic tests. The accelerometers record values up to 2 g for all three axes with a sampling rate of 2000 Hz.

5.2 Experimental analysis

The horizontal force F applied on the frame as well as the displacement of the frame u are recorded in order to generate a pushover curve (see Figure 5.5). The force can be calculated from the pressure in the hydraulic system. The displacements are measured with two LVDTs placed on top of the beams and can also be estimated with the LEDs attached on the columns.
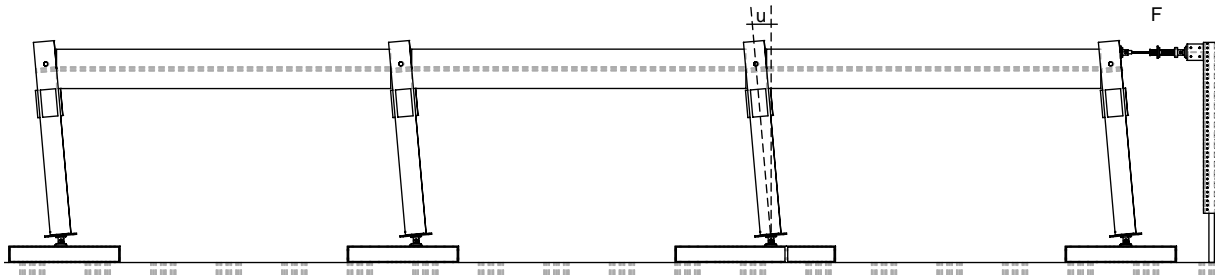
Figure 5.5: Deformed frame under horizontal load F with horizontal displacement u

However, for a comparison between the test results and the results obtained from an analytic model, the rotations have to be estimated as well. The LEDs attached to the connections allow calculating the rotations in the connections themselves. These rotations can be compared to the model in order to check its accuracy.

The rotations in the interface can be separated into rotations due to shear and due to the moment acting on the connection area. The LEDs are positioned on the interface as shown in Figure 5.6(a). If a horizontal load F is applied on the frame, a lateral displacement occurs, as shown in Figure 5.6(b) for a rigid body. The two resulting forces R acting on the interface lead to a shear deformation in the column as shown in Figure 5.6(c) and also due to the moment in the column as shown in Figure 5.6(d). The latter type of rotation is the same that could be observed during the test on the post-tensioned timber joint under gravity loads as discussed in Chapter 4. The total rotation of the interface is the sum of the rotation due to shear and moment in the column:

$$\theta_{tot} = \theta_{GA} + \theta \tag{5.1}$$

The total deformation of the column can be estimated by using the inclinometers or with the LEDs. The inclination of the beam-column interface minus the elastic rotation of the column $\theta_{col,el}$ corresponds to the total rotation θ_{tot}. Both components are shown in Figure 5.6(e).

Moreover, it is possible to determine the single components of the rotation by using the LEDs. The rotation due to shear θ_{GA} can be estimated with the length of the diagonals D and D' as shown in Figure 5.6(c). The diagonal D was chosen, since it is not influenced by the compression perpendicular to the grain. The moment acting on the column will lead to the behaviour known from the tests on the post-tensioned timber connection, i.e. the beam will be pressed into the column, leading to a compressive zone and a gap opening (Figure 5.6(d)). The total rotations are shown in Figure 5.6(e) and include the rotation due to shear as well as the rotation due to the moment. Moreover, the column itself will also rotate, due to the moment in the column.

This procedure is also valid for the outer column with only one beam-column interface. However, the resulting force R is fixed to the middle of the column on the side where the anchorage is mounted as shown in Figure 5.6(f). The shear panel is smaller for the outer column compared to the inner one and the shear deformation will therefore not be as large compared to the inner column.

Since the columns are wider than the beams (380 mm compared to 280 mm) the LEDs are not in the same plane as the surface of the beams. Therefore, the recorded displacements may be too small. The influence on the total rotation will be negligible, since it mainly depends on the rotation of the interface and the column. However, the influence on the shear rotations may be significantly larger. The recorded values should therefore only be considered as approximations.

5.3 Experimental analysis for the dynamic tests

The frame was excited horizontally by using a large impact hammer, whereas the accelerometers mounted on the columns and beams recorded the amplitude of the impulse.

These experiments were performed as preliminary tests for a larger campaign on a building site.
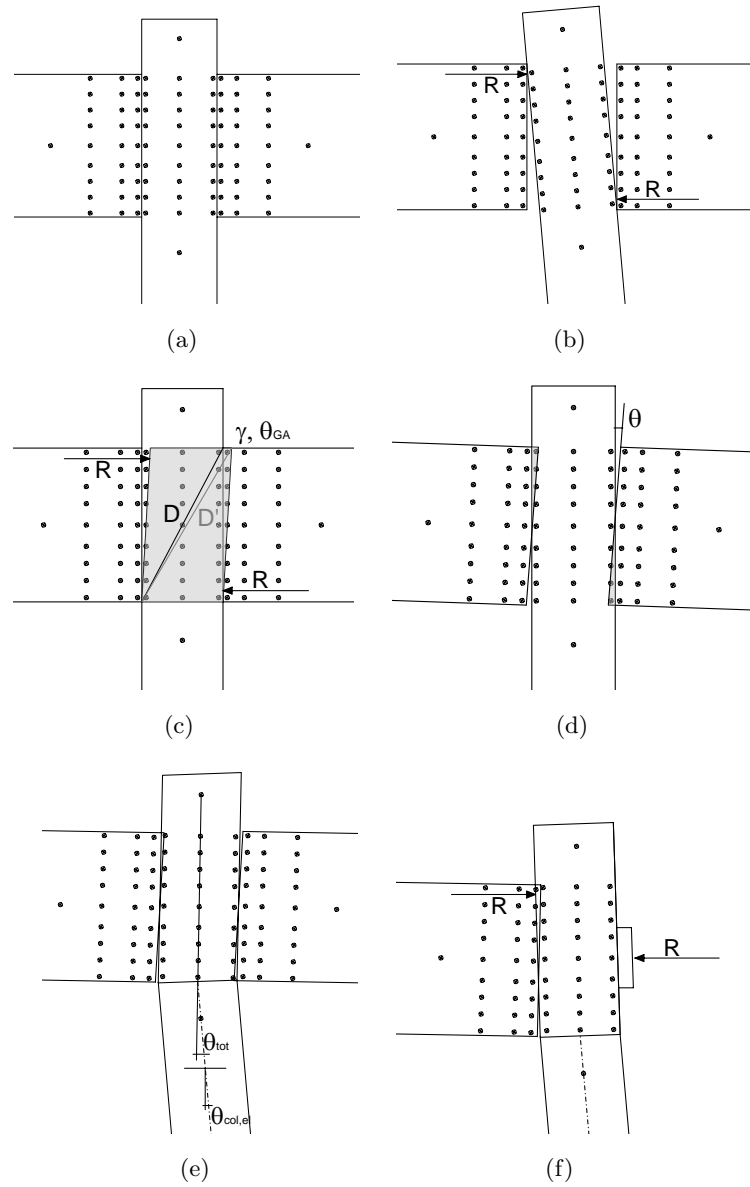
Figure 5.6: 5.6(a): LEDs on the unloaded specimen 5.6(b): Rigid body motion and resulting force R on the interface 5.6(c): Shear rotation θ_{GA} in the connection area 5.6(d): Rotation due to the moment θ in the beam-column interface 5.6(e): Total rotation θ_{tot} of the specimen due to shear, compression and elastic rotation of the column $\theta_{col,el}$ 5.6(f): Rotation of the outer column with resulting forces R in the connection area

5.4   Test results

The test results for three different tendon forces (600 kN, 500 kN and 400 kN) are presented in this chapter. The tendon forces are representative for the tests with a high, an intermediate and a low tendon force. The initial stresses are similar to the ones from the tests presented in Chapter 4 and correspond to 3.0 MPa, 2.5 MPa and 2.0 MPa.

Moreover, investigations concerning the long-term behaviour suggest that losses in tendon force of approximately 30% should be accounted for in the design process (see Chapter 7). Such a loss can be represented by these test series, i.e. 600 kN is representative for the initial tendon force, whereas 400 kN corresponds to the tendon force including the long-term losses.

5.4.1   Tests with a high tendon force

The pushover-curve for the tests performed with a tendon force of 600 kN is plotted in Figure 5.7. The curve shows a nearly linear behaviour with a slight decrease in stiffness for higher forces. No energy dissipation could be observed, i.e. the loading path corresponds to the unloading path.
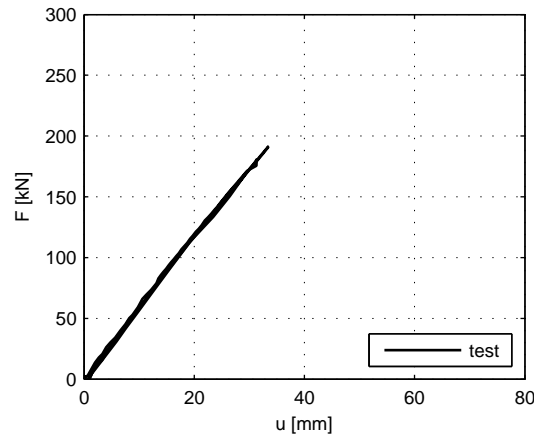
Figure 5.7: Pushover-curve for the test with a tendon force of 600 kN

The rotations in the inner column with two adjacent beams are shown in Figure 5.8(a), the black curve indicating the total rotations, whereas the rotations due to shear are plotted in grey. It is noticeable that the rotations due to shear account for over 60% of the total rotation, whereas only a small part is due to the moment acting on the connection, i.e. the difference between the total rotations and the rotations due to shear.

The rotations in the outer column with one adjacent beam are shown in Figure 5.8(b). The rotations due to shear (grey) are very small compared to the total rotations (black). This means that most of the rotation are due to the moment acting on the connection. The total rotations are larger than for the inner column, i.e. the connection at the outer column is softer than the ones at the inner column.
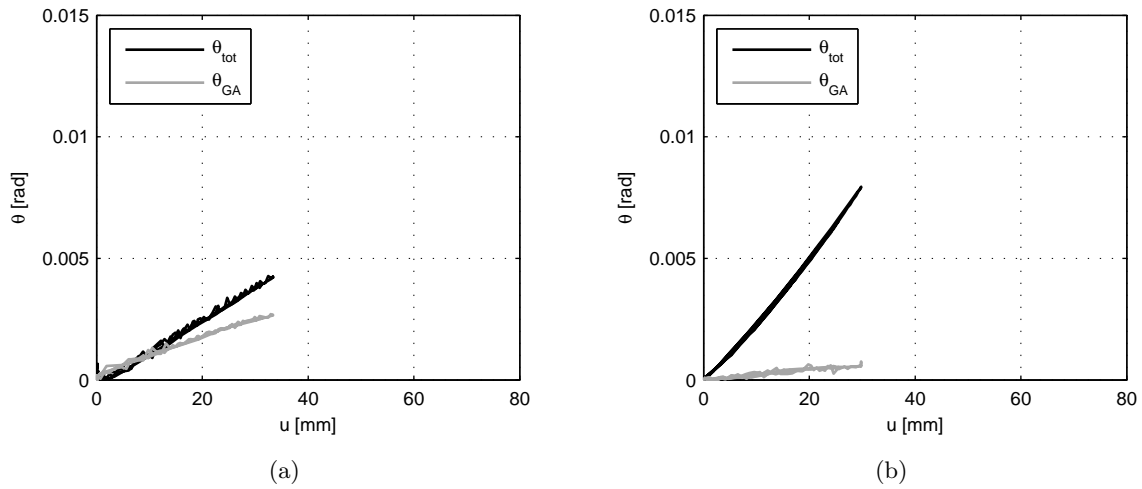
Figure 5.8: 5.8(a): Rotation for the inner column tested with a tendon force of 600 kN 5.8(b): Rotation for the outer column tested with a tendon force of 600 kN

5.4.2 Test with an intermediate tendon force

The pushover-curve for the tests performed with a tendon force of 500 kN is shown in Figure 5.9. The plot is slightly curved, the stiffness decreases with increasing lateral force. As opposed to the previous case with a high tendon force, the loading and unloading paths differ from each other. This could mean that the column is getting deformed and therefore absorbs some energy.
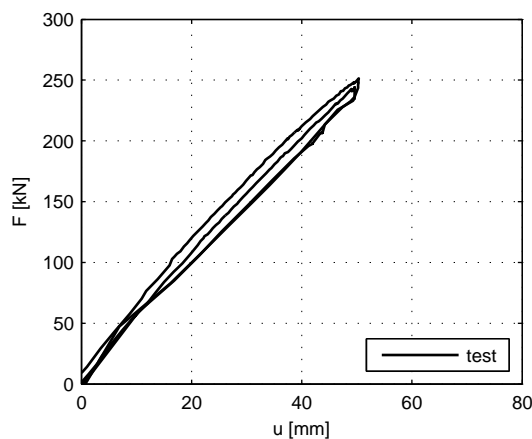
Figure 5.9: Pushover-curve for the test with a tendon force of 500 kN

The rotations in the inner column with two adjacent beams area are shown in Figure 5.10(a) and the rotations in the outer column with one adjacent beam area are shown in Figure 5.10(b). For the inner column, the rotations due to shear account for approximately 60% of the total rotation, as opposed to the outer column, where they are significantly smaller. The total rotations of the outer column are approximately twice as high compared to the inner column.

(a)   (b)
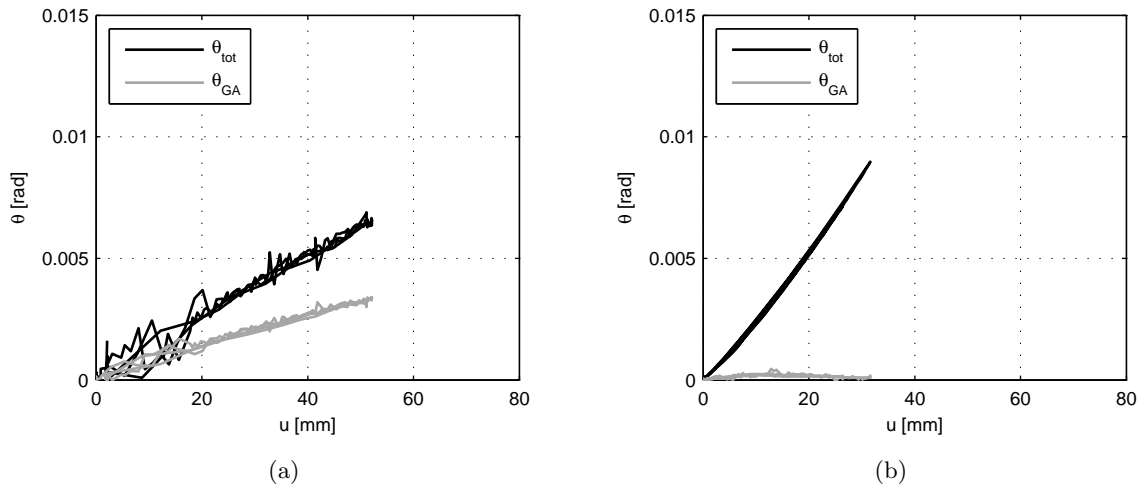
Figure 5.10: 5.10(a): Rotation for the inner column tested with a tendon force of 500 kN 5.10(b): Rotation for the outer column tested with a tendon force of 500 kN

5.4.3   Tests with a low tendon force

The pushover-curve for the tests performed with a tendon force of 400 kN is shown in Figure 5.11. The curve is similar to the one from the previous case, with different loading and unloading path.
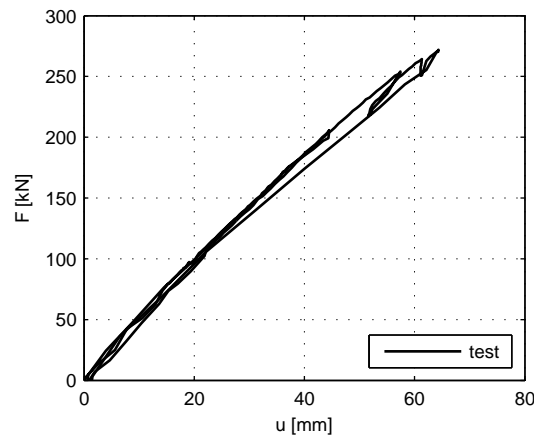
Figure 5.11: Pushover-curve for the test with a tendon force of 400 kN

Figure 5.12(a) shows the rotation in the inner column with two adjacent beam, Figure 5.12(b) the rotations in the outer column, where the total rotations are approximately twice as high. The rotations due to shear are far lower for the outer column compared to the inner column, where they account for nearly 50% of the total rotations.
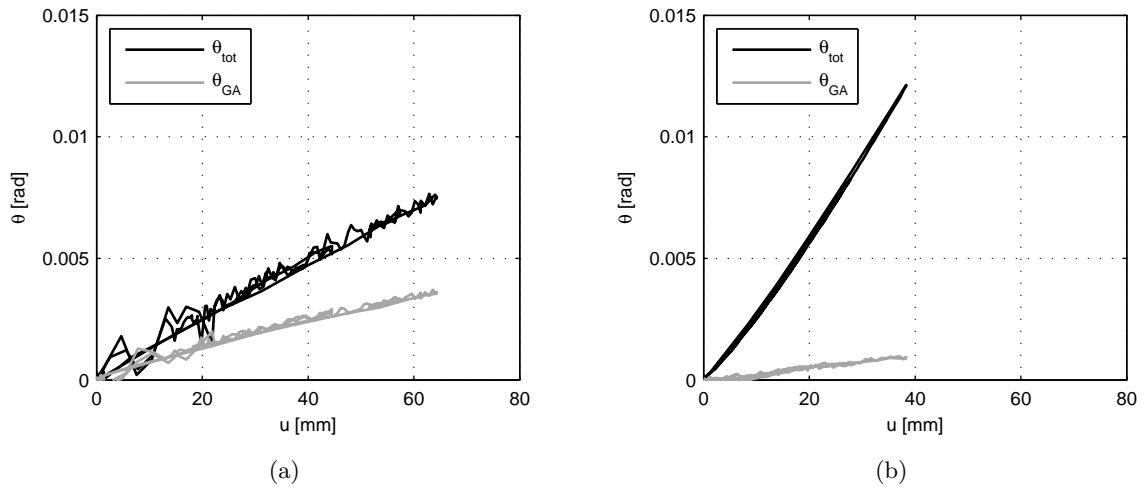
Figure 5.12: 5.12(a): Rotation for the inner column tested with a tendon force of 400 kN 5.12(b): Rotation for the outer column tested with a tendon force of 400 kN

5.5 Comparison model and test results

5.5.1 Pushover-curves

The pushover-curves for all tests are shown in Figure 5.13 together with the analytical solution, which is independent of the tendon force. The analytical solution matches the results for the tests with a tendon force of 600 kN and 500 kN, respectively. The higher the tendon force is, the better the match between the analytical model and the test results.
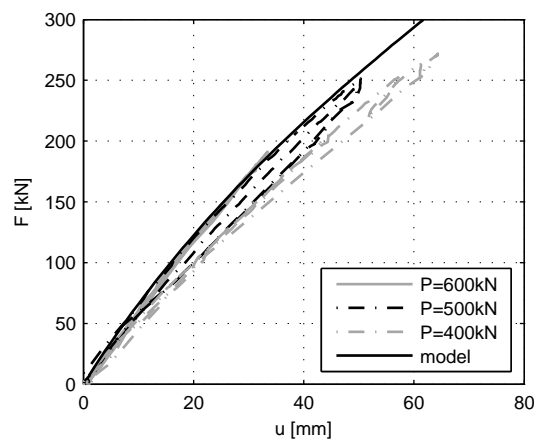
Figure 5.13: Pushover-curve for a tendon force of 600 kN, 500 kN and 400 kN including the pushover-curve obtained from the analytical solution

5.5.2 Rotations at the connections

The rotations measured at the connections are shown in Figure 5.14 (grey lines) together with the analytical solution (black lines).
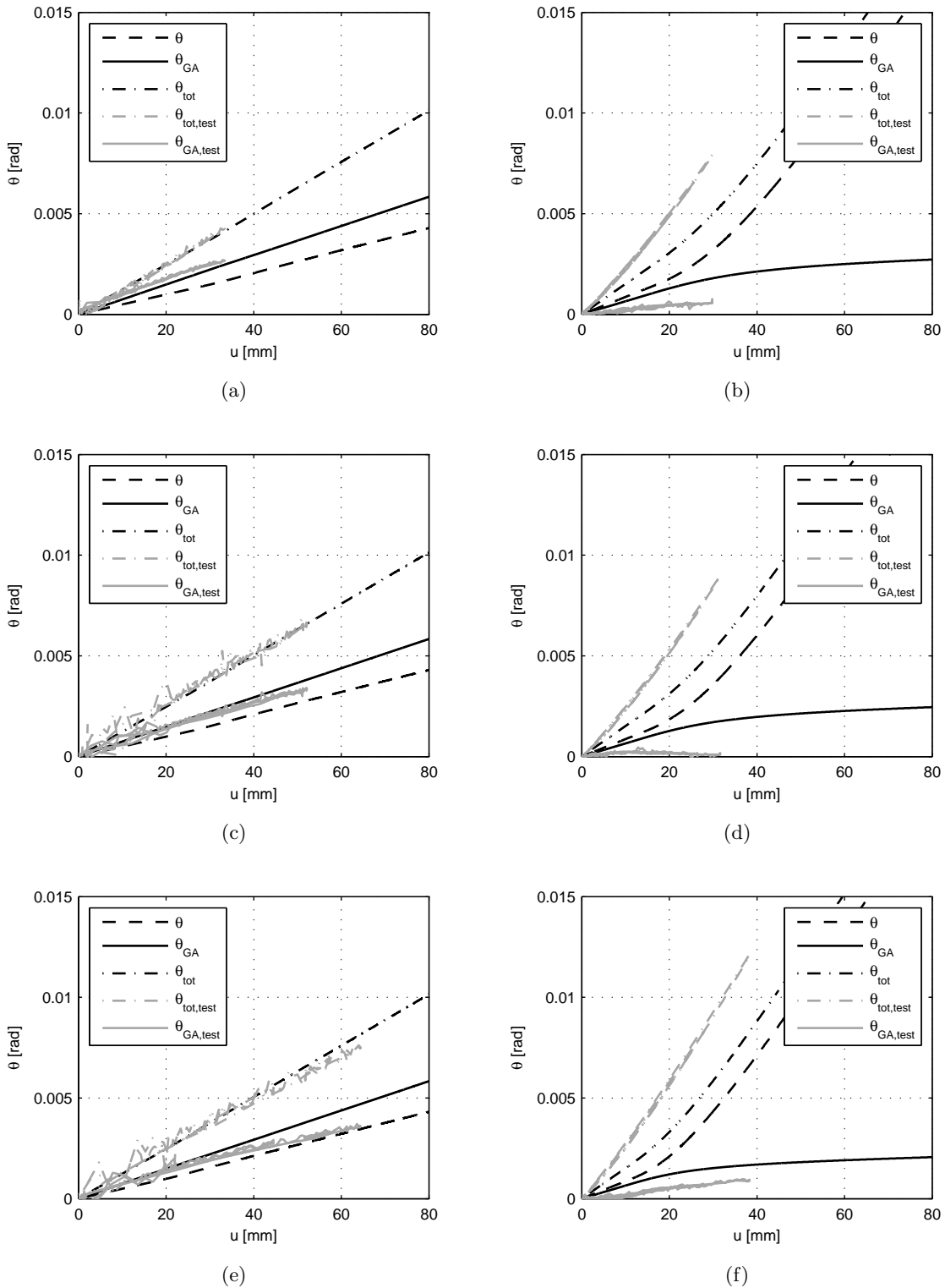
Figure 5.14: Rotations from tests (grey) and the analytical model (black); Total rotations θ_{tot}, rotations due to shear θ_{GA} and rotations due to the moment θ for different tendon forces P 5.14(a): Inner column P=600 kN 5.14(b): Outer column P=600 kN 5.14(c): Inner column P=500 kN 5.14(d): Outer column P=500 kN 5.14(e): Inner column P=400 kN 5.14(f): Outer column P=400 kN

The rotations for the inner column are plotted in Figures 5.14(a), 5.14(c) and 5.14(e), i.e. all figures on the left, whereas the rotations of the outer column are plotted on the right (Figures 5.14(b), 5.14(d) and 5.14(f)).

The rotations in the inner column with two adjacent beams are always predicted well by the analytical model, both for the total rotations θ_{tot} as well as for the rotations due to shear θ_{GA}. Note that the analytical solution is also given for the rotation due to the moment θ acting on the connection.

The rotations at the outer column with only one adjacent beam are not predicted as well as for the inner column. The total rotation is under-predicted by the analytical model, whereas the rotations due to shear are over-predicted by the model throughout all the performed tests.

5.6 Experimental analysis - discussion

5.6.1 Dynamic tests

The measured horizontal excitation from the impact hammer test is plotted in Figure 5.15(b) for a tendon force of 600 kN. The other two tests (with a tendon force of 500 kN and 400 kN are not shown since the figures would look very much alike). The data was obtained from the accelerometer mounted on the outer column, i.e. the same column that was used for the impact. The recorded amplitude is largest at the beginning and gets smaller due to the damping of the system.

The impact tests allow estimating the damping ratio of a single post-tensioned timber frame. The eigenfrequency of the system was estimated with the impulse from the hammer by performing a Fourier analysis. The eigenfrequency could be estimated according to Figure 5.15(a) to 8.7 Hz.
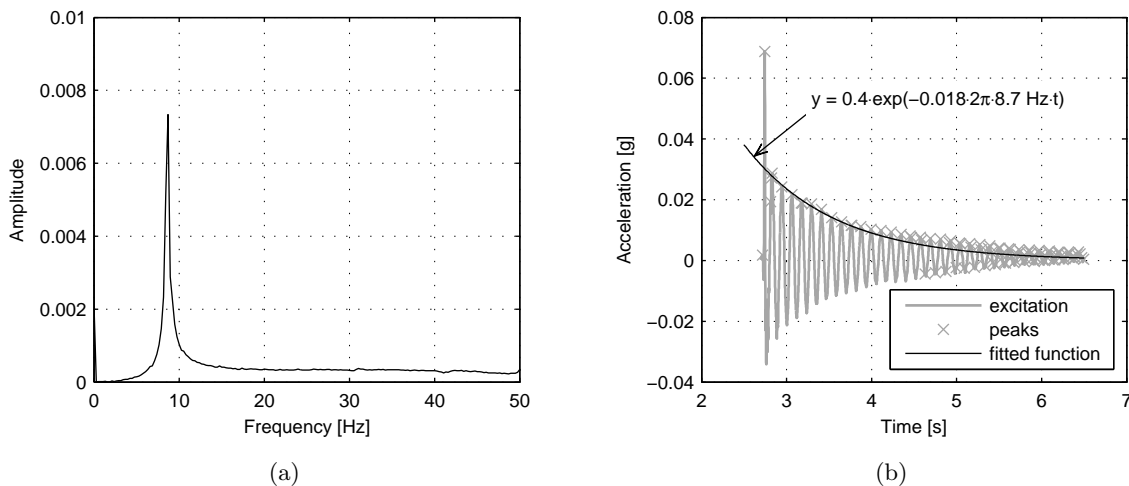
Figure 5.15: 5.15(a): Frequency spectrum for the impact hammer test on the post-tensioned timber frame 5.15(b): Damping ratio of the post-tensioned timber frame from impact hammer test

The recorded excitation is shown in Figure 5.15(b). The damping can be estimated with an envelope [74] of the form $\rho \cdot e^{-\omega_n \cdot \zeta \cdot t}$ which was added to the data obtained from the excitation.

The damping ratio ζ can be estimated with 1.8% for the shown excitation. In order to simplify the fitting of the envelope a Butterworth filter [75] was applied beforehand, which eliminated all frequencies above 50 Hz.

The eigenfrequencies as well as the damping ratios are summarised in Table 5.3

Table 5.3: Estimated eigenfrequencies from impact hammer test and pushover tests

Tendon force	Eigenfrequency [Hz]	Damping ratio [%]
high	8.7	1.8
intermediate	8.4	1.8
low	8.6	2.2

5.6.2 Pushover tests

The results of the experimental analysis show the favourable structural behaviour of the developed post-tensioned timber frame. The frame can deform under horizontal loads and re-centre itself if the load is reduced. Nearly no damage occurred during the tests, only minor residual deformations were observed during the entire test series.

The three test series with a tendon force of 600 kN, 500 kN and 400 kN (plotted in Figure 5.16) showed that a loss of 30% tendon force only leads to a small decrease in horizontal stiffness. A decrease in stiffness of 20% can be observed at a horizontal load of 150 kN by comparing the curves for a tendon force of 600 kN and 400 kN, which corresponds to an increase in lateral displacement of 7 mm.
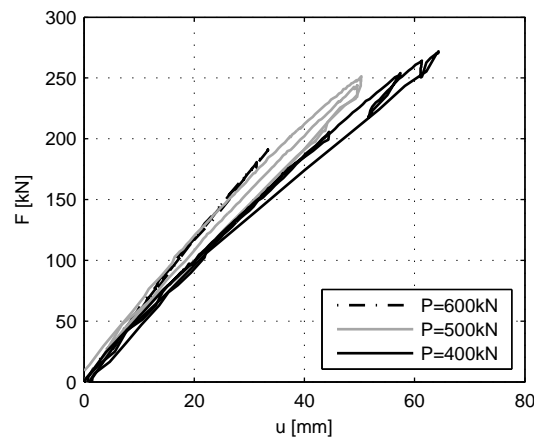
Figure 5.16: Pushover-curve for a tendon force of 600 kN, 500 kN and 400 kN

Figure 5.17 shows the analytical pushover-curves for the investigated post-tensioned timber frame as well as for the same frame with rigid beam-column connections. The difference in stiffness is small for displacements smaller than 20 mm, increases however for larger displacements as the post-tensioned timber frame softens with increasing lateral force. This behaviour is very favourable; the system is stiff for small displacements as can occur during wind loads and it is

softer for larger displacements as can be induced by an earthquake, making it less vulnerable to damage.
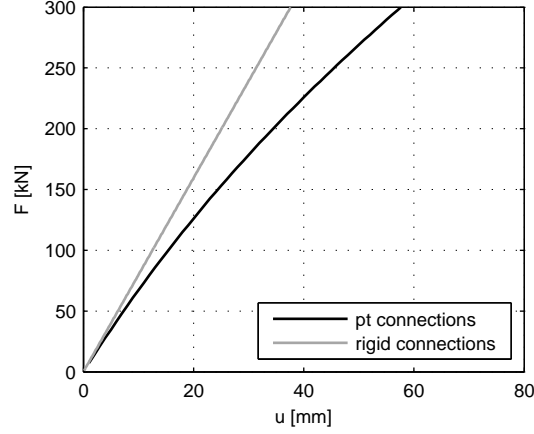
Figure 5.17: Analytical pushover-curve for a three bay frame with post-tensioned timber connections (black) and for the same frame with rigid beam to column connections

The theoretical horizontal stiffness up to the moment of decompression can be calculated with Equations (3.26)-(3.27):

$$K_{tot} = 2 \cdot K_o + 2 \cdot K_i = 136'800 kNm/rad \qquad (5.2)$$

and therefore:

$$K_{hor,max} = \frac{F}{u} = \left(\frac{h_c^3}{4 \cdot 3 \cdot E_c \cdot I_c} + \frac{h_c}{4 \cdot G_c \cdot A_c} + \frac{h_c^2}{K_{o,i}} \right)^{-1} = 6580 kN/m \qquad (5.3)$$

The initial stiffnesses of the frame were measured during each test and are shown in Figure 5.18(a). It can be seen, that the calculated stiffness could be matched for higher tendon forces, whereas the system behaves softer than predicted for lower tendon forces. This was already the case for the model predictions with the post-tensioned timber joint described in Chapter 4. Moreover a scatter even within the tests of equal tendon forces is noticeable. This is due to a major issue that occurred during the tests; as a result the low humidity in the environment, several cracks occurred in the specimens, especially the columns made of ash.

Figure 5.18(b) shows the actual stiffness normalized with the theoretical one versus the initial compressive stress. It is recommended to apply a tendon force that guarantees an initial compressive stress of 2.5 MPa at all times in order to obtain at least 80% of the calculated stiffness.

The analytical model was able to predict the connection behaviour under gravity loading reasonably well, including the tendon elongation. The same model was used to describe the tests described in this paper and analytical formulations were derived in order to calculate the pushover-curve. The model was able to predict the pushover-curve well for higher tendon forces whereas
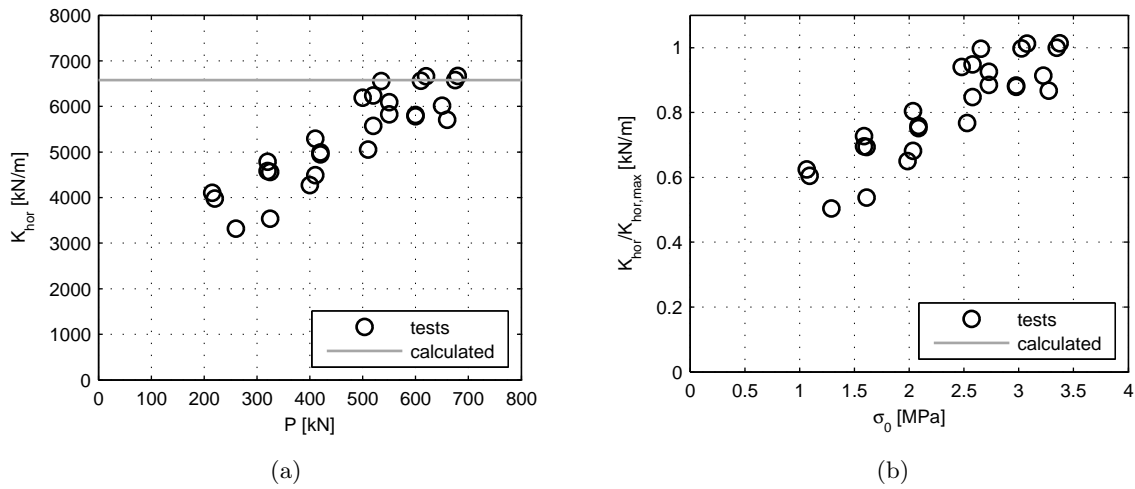
Figure 5.18: Measured and calculated initial horizontal stiffness for the post-tensioned timber frame specimen 5.18(a): Stiffness- tendon force plot 5.18(b): Stiffness normalized with theoretical stiffness over initial comrpessive stress on the connection due to tendon force

the model predicts a stiffer behaviour than measured for lower tendon forces.

One reason for the difference lies within the simplifications of the model, which is purely elastic and assumes that the beams are rigid. For the test with a tendon force of 400 kN there is an additional reason for the over-prediction of the stiffness. During the test series no increase in tendon force could be observed, however, the model predicted the gap to reach the tendon and elongate the latter, so that the force should start to increase at a lateral deformation of 40 mm as shown in Figure 5.19. The test showed nearly no increase in tendon force, which may be due to shortening of the frame due to grain crushing in the connection area or due to a measurement error in the hydraulic system.
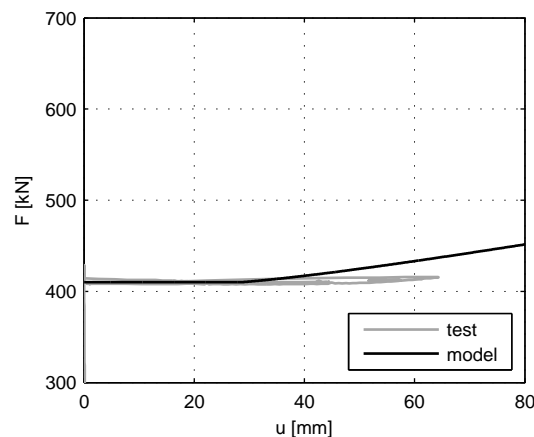
Figure 5.19: Tendon force during the test series with P=400 kN and analytical tendon force from the spring model

The model was able to reproduce the connection rotations well, especially for the inner column with the two adjacent beams. The outer column showed larger rotations than predicted for all the tests performed for this study. The reason for this is the load application, which was positioned on top of the outer column, leading to an additional inclination and therefore rotation. Figure 5.20 shows the inclination of all four columns for the pushover-test with a tendon force of 600 kN, measured with the inclinometers attached to the columns. The outer columns correspond to the black lines in Figure 5.20, whereas IL_{S1} is the column with the LEDs and the load application, i.e. the column that was used to estimate the rotations. It can be seen, that this column shows larger inclinations than the last column in the frame IL_{S4}. The two inner columns IL_{S2} and IL_{S3} behave nearly identical, showing the same amount of rotation during the test.
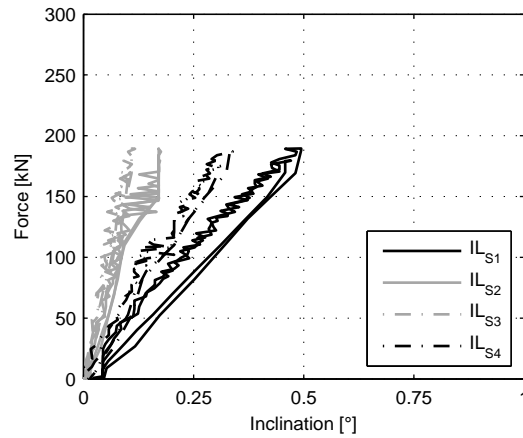
Figure 5.20: Inclination of the four columns during a pushover-test with a tendon force of 600 kN

The model also shows that the outer connections are softer than the inner ones (see Figure 5.21), which is due to the fact that the inner connections have two interfaces and are governed mainly by the shear rotations. Therefore, the connections behave nearly completely linear under horizontal loading, making it very easy to model. The outer connections are softer and mainly rotations due to compression were observed, whereas the shear deformations are smaller compared to those of the inner ones. This is due to fact, that the resulting force is located at the anchorage of the tendon.

The impact tests allowed estimating the eigenfrequency and the damping ratio of the system. The eigenfrequencies were estimated at approximately 8.5 Hz, whereas the damping was estimated at 2%. The period can be estimated from the pushover-curves according to [76] for a system with one degree of freedom:

$$T = 2 \cdot \pi \sqrt{\frac{u \cdot W}{F \cdot g}} \tag{5.4}$$

The eigenfrequency is then:

$$f = \frac{1}{T} \tag{5.5}$$
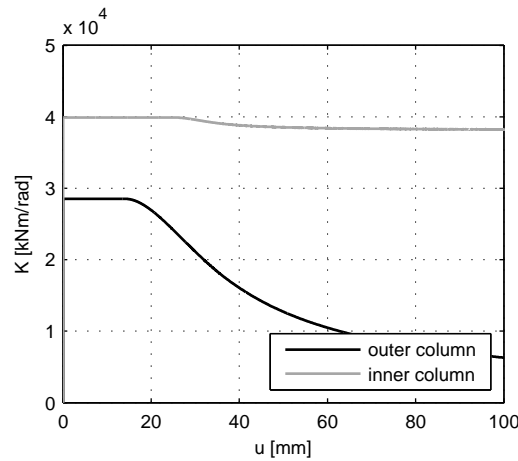
Figure 5.21: Stiffness of the inner and outer connection according to the analytical model

The weight of the superstructure of the frame is approximately 2'000 kg. The obtained values for the eigenfrequencies are summarised in Table 5.4. The values were estimated for the pushover-curves at a force F of 150 kN for the second loading cycle.

Table 5.4: Estimated eigenfrequencies from impact hammer test and pushover tests

Tendon force	Eigenfrequency [Hz]	
	Impulse	Pushover
high	8.7	8.6
intermediate	8.4	7.9
low	8.6	7.8

The values estimated from the pushover-curves are smaller than the ones from the impact hammer, especially for the low and intermediate tendon forces. The values from the pushover-curves match the softening behaviour as the tendon force decreases, i.e. the eigenfrequencies get smaller with smaller tendon forces and vice versa.

All damping ratios and eigenfrequencies are estimated for a single frame. A structure includes the lateral beams (i.e. in direction perpendicular to the frame) as well as floors and under given circumstances non-structural elements. The damping ratios as well as the eigenfrequencies are currently being investigated on a real building with post-tensioned timber frames [77]. These tests were performed by using an impact hammer but also with an electromechanical shaker, which is suited for the excitation of large structures.

Chapter 6

Numerical model

Based on the analytical approach described in Chapter 3, a numerical model was developed using the OpenSees finite element modelling framework [78], a free-ware that proved to be highly suitable to model the presented post-tensioned timber connection under static loading.

6.1 Model for connection tests

A model was created in order to simulate the behaviour of the connection specimen, which was subjected to vertical loading (as described in Chapter 4). The geometry of the numerical model corresponds to the one of the test specimen, except for the length of the beams, which are longer in the numerical model. Instead of considering the anchorage with all its details (nut and head of anchorage), the beams were modelled longer, so that the length of the tendon in the model corresponds to the original length in the test specimen. An accurate length of the tendon is important since it influences the increase in tendon force. The shorter the tendon, the higher the increase in tendon force (see Equation (3.18)). With this procedure, the connection itself is modelled more accurately, which is the focus of our investigations, as opposed to the anchorage detail.

6.1.1 Geometry and material properties

The numerical model for the connection in shown in Figure 6.1(a) in its initial state after pre-stressing. The model can then either simulate a symmetric load case as shown in Figure 6.1(b) or an asymmetric load case as shown in Figure 6.1(c), i.e. the same load cases that were performed during the tests on the post-tensioned timber connection described in Chapter 4.

The mesh of the numerical model is coarse in the areas which are not of any interest (main parts of the column and beams) and more dense in the area of interest, i.e. the beam column interface, whereas the edge of the beam was also modelled with a finer mesh.

The beams are not connected to the column at the interface. A tendon is modelled, which is connected to the steel plates at each end of the beams (see Figure 6.1(a), areas with a finer mesh at the edge of the beams). The tendon is supported in the column, so that it cannot move in vertical direction. This is necessary, since the tendon is positioned in a cavity within the

specimen, holding it in place. The tendon is therefore always positioned in the centre of the beam and column, respectively.

The ash reinforcement of the beam (bottom three lamellae at the beam-column interface) was not modelled, since the stiffness parallel to the grain is similar for ash and spruce.

The same material properties are used for the OpenSees model as for the analytical model, i.e. the properties listed in Tables 4.1 and 4.2.
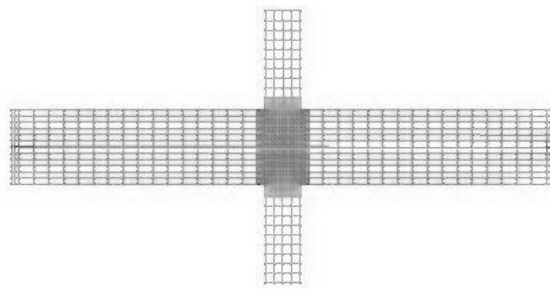
(a)
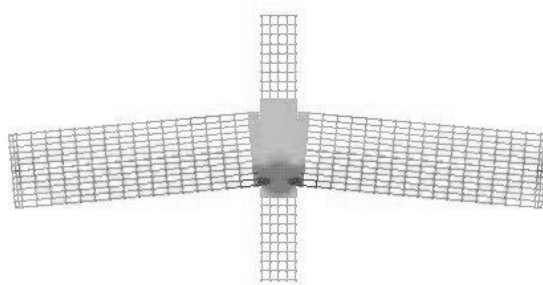
(b)
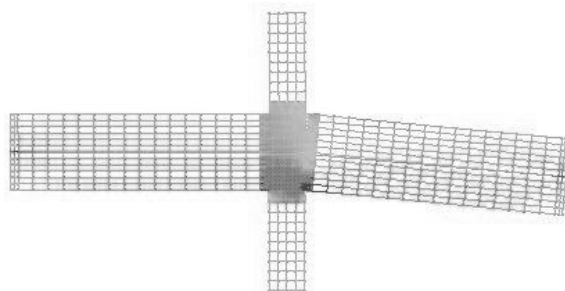
(c)

Figure 6.1: Numerical model 6.1(a): In its initial state after pre-stressing 6.1(b): Under symmetric loading 6.1(c): Under asymmetric loading

6.1.2 Elements and material tags

The model was created using the following elements:

- Four nodes (quadrilateral) shell elements for the timber parts as well as the steel plates at the end of the beams

- Corotational truss element for the tendon (1D element)

- Zero length element for the connection area to model the gap between the column and the beams

Material properties have to be assigned to each type of element. The materials for the model are defined as follows:

- J2-plasticity for the joint area of the model which accounts for embedment failure perpendicular to the grain of the column (controlling design criterion)

- Elastic orthotropic material for the columns of the model, which takes shear deformations into account; the Poisson's ratio ν_{RL} was set to 0.059 [79]

- Elastic isotropic material for the beams

- Uniaxial initial strain material for the tendon in combination with uniaxial material "Steel02"; the initial strain is used to model the tendon force

- Elastic isotropic material for the steel plates at the end of the beams

- Elastic, no-tension material for the zero length elements in order to allow a gap to open between the column and the beams

6.1.3 Recorders

Several recorders were set in order to obtain results from the numerical simulations. The following values were recorded:

- Stresses in the elements at the beam-column interface (in both, the beam and the column) to estimate the stresses and in order to calculate the moment in the connection area as well as the height of the neutral axis

- Drift in two elements at a distance of 70 mm at the beam-column interface (the rotation was calculated the same way as for the test evaluation in Chapter 4) in order to measure the rotation of the connection

- Displacements of the nodes at the beam-column interface (in both, the beam and the column) to check the neutral axis depth and the rotation

- Axial force in the tendon

6.1.4 Analysis

The analysis is performed in two stages:

- Apply tendon force in 10 steps

- Load the beams with a load in vertical direction up to a certain deformation under the beam. The load is applied 2 m from the beam-column interface in 100 steps

6.1.5 Predictions from the elastic model for the symmetric load case

The prediction from the numerical model are plotted with the test results in Figure 6.2. The predictions obtained with the analytical model were added as a reference.
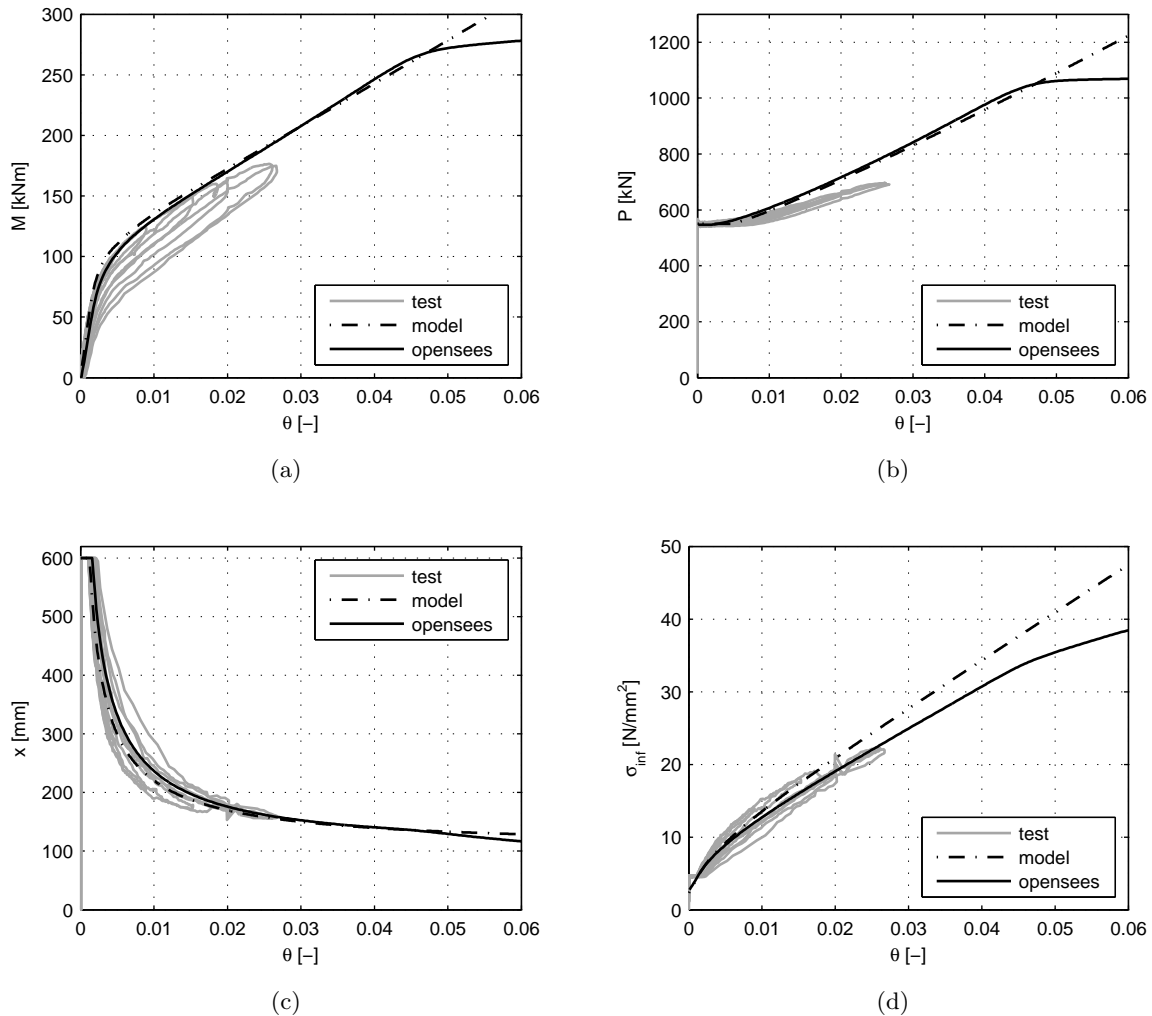
Figure 6.2: Test results and analytical as well as numerical model prediction 6.2(a): Moment-rotation behaviour 6.2(b): Tendon force 6.2(c): Neutral axis depth 6.2(d): Stresses at the interface

The predictions from the numerical model correspond well to the ones from the analytical model as well as the test results. The numerical model shows a slightly softer behaviour in the moment-

rotation-plot for moments smaller than 100 kNm as can be seen in Figure 6.2(a). The tendon force corresponds to the one from the analytical model (Figure 6.2(b)), with the difference that the tendon has a yield point in the numerical model. There are basically no differences in the neutral axis depth between the two models as shown in Figure 6.2(c). The stresses are, however, slightly smaller than for the analytical model (Figure 6.2(d)).

6.1.6 Predictions from the plastic model for the symmetric load case including grain crushing

The predictions presented in this section were generated with a J2-plasticity-material in the column interface. This means that the column is able to yield and a failure (grain crushing) can therefore be modelled. The predictions from the numerical model are plotted in Figure 6.3 together with the predictions from the analytical model and the test results.
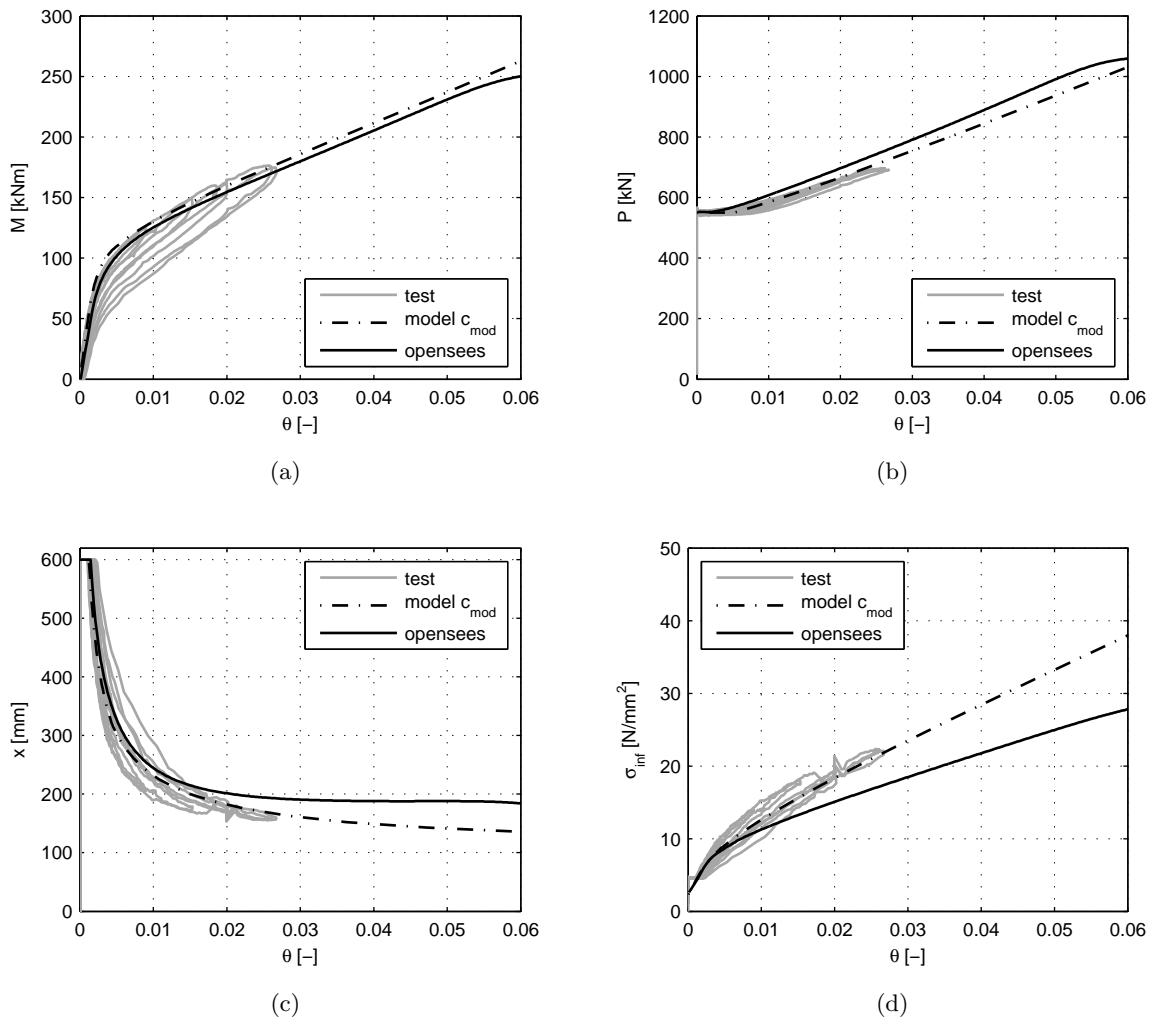
Figure 6.3: Test results and analytical as well as numerical model prediction including embedment failure in the column 6.3(a): Moment-rotation behaviour 6.3(b): Tendon force 6.3(c): Neutral axis depth 6.3(d): Stresses at the interface

The numerical model shows a softer behaviour in the moment-rotation-plot (Figure 6.3(a)) compared to the previous case with no embedment failure. Furthermore, the tendon force starts to increase at a lower rotation compared to the analytical model and the test results (Figure 6.3(b)). The stresses differ from the ones calculated by the model and also from the tests (Figure 6.3(d)). This can be attributed to the assumption that the section remains plain for the test evaluation and also for the analytical model, which are both based on linear elastic theory and are therefore unable to predict the stresses accurately after grain crushing occurs in the column. As a result, the neutral axis depth does not decrease further after a certain rotation has been reached, as can be seen in Figure 6.3(c).

6.1.7   Predictions from the orthotropic model for the asymmetrical load cases

The tests performed on the post-tensioned timber connection also included asymmetrical load cases, where only one beam was loaded while the other one remained unloaded. The moment-rotation behaviour was evaluated for the tests and is plotted in Figure 6.4 with the values derived from the analytical model and also with the values from the numerical model. Both models show a nearly identical moment-rotation behaviour.
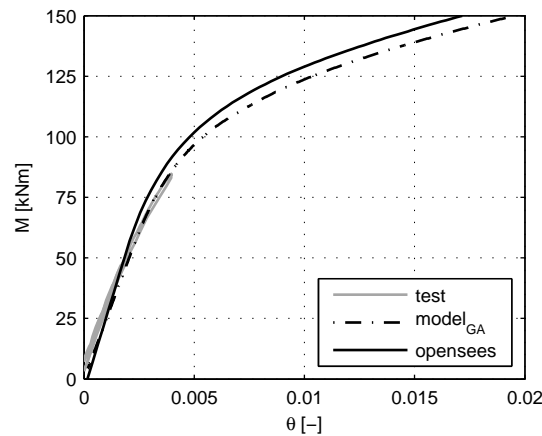
Figure 6.4: Predictions from the numerical and analytical model and test results for the asymmetrical load case including shear deformations in the column

6.2   Frame model for pushover tests

A frame model was developed based on the orthotropic connection model in order to compare the predictions with the analytical ones and the results from the pushover tests presented in Chapter 5. The geometry corresponds to the one of the test specimen; the columns were modelled longer in order to account for the connection at the bottom of the column. The model is shown in Figure 6.5(a) in its initial state and in Figure 6.5(b) in its deformed state.

(a)

(b)
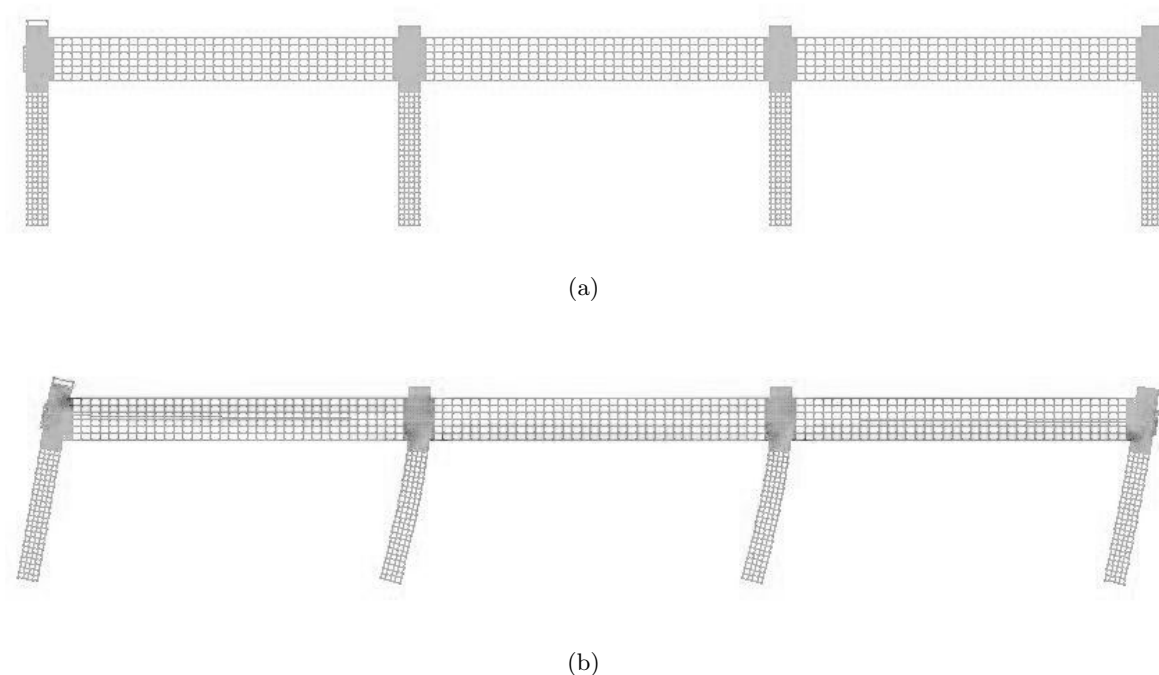
Figure 6.5: 6.5(a): Frame model for pushover-simulation 6.5(b): Deformed model after horizontal load is applied

6.2.1 Elements and material tags

The finite elements used in the numerical frame model are the same as those that were used for the numerical connection model:

- Four nodes (quadrilateral) shell elements for the timber parts as well as the steel plates at the end of the beams

- Corotational truss element for the tendon (1D element)

- Zero length element for the connection area

Material properties have to be assigned to each type of element. The materials are identical to the ones used for the connection model and are defined as follows:

- Elastic orthotropic material for the columns of the model; the Poisson's ratio ν_{RL} was set to 0.059 [79]

- Elastic isotropic material for the beams

- Uniaxial initial strain material for the tendon in combination with uniaxial material "Steel02"; the initial strain is used to model the tendon force

- Elastic isotropic material for the steel plates at the end of the beams

- Elastic no tension material for the zero length elements (gap)

6.2.2 Recorders

Several recorders were set in order to obtain results from the numerical simulations. Since only the connection behaviour is of interest, no attention was given to the elastic deformation of the beam or the column itself. The following values were recorded:

- Forces in the columns to calculate the base shear (which is equal to the applied force)

- Displacements in the frame for the pushover curve

- Axial force in the tendon

6.2.3 Analysis

The analysis is performed in two stages:

- Apply tendon force in 10 steps

- Loading the first column on the left (Figure 6.5(a)) with a horizontal force

6.2.4 Predictions from the numerical model for pushover analysis

The pushover-curve for the numerical model is plotted in Figure 6.6 with the prediction obtained from the analytical model and the test results for an initial tendon force of 500 kN. It is noticeable that the numerical model shows a softer behaviour than the analytical model and the test results. The beams were modelled rigid in order to compare the predictions from OpenSees with the one from the analytical model.
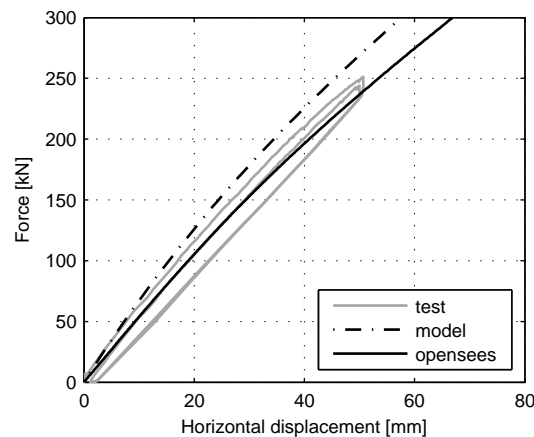
Figure 6.6: Comparison between the predictions made with the numerical and analytical model and the results from the pushover tests

The difference between the numerical model and the analytical model is small for small displacements. If the displacements get larger, the discrepancy increases. The numerical model also takes into account that the elements deform under loading (i.e. the elements get shorter), which the analytical model does not. However, several parameters are needed for the numerical model that remain uncertain, like the Poisson's ratio for the spruce and ash elements.

6.2.5 Parametric study

A short parametric study was performed in order to demonstrate the influence of the parameters. Two additional calculations are presented herein whereas only the column properties were changed. The first altered model has stiffer connections, i.e. the shear modulus as well as the Young's modulus perpendicular to the grain were increased to 1200 MPa as shown in Table 6.1. A second model uses the same properties in the connection area, however, the Young's modulus parallel to the grain of the column was increased to 16000 MPa (see Table 6.1).

Table 6.1: Parameters in [MPa] for original and modified models used for the parametric study

Property	Original	Modified connection	Modified column
E_0	13000	13000	16000
E_{90}	860	1200	860
G	810	1200	810

The pushover-curve for the model with the stiffer connection properties is shown in Figure 6.7(a). It can be seen that only a very small increase in stiffness was achieved by improving the connection properties. It is therefore not relevant to estimate the two parameters E_{90} and G more accurately.

The pushover-curve for the model with the stiffer column is presented in Figure 6.7(b). An increase of stiffness is clearly noticeable. Therefore, the bending stiffness of the column influences the outcome more than the connection properties.

(a)

(b)
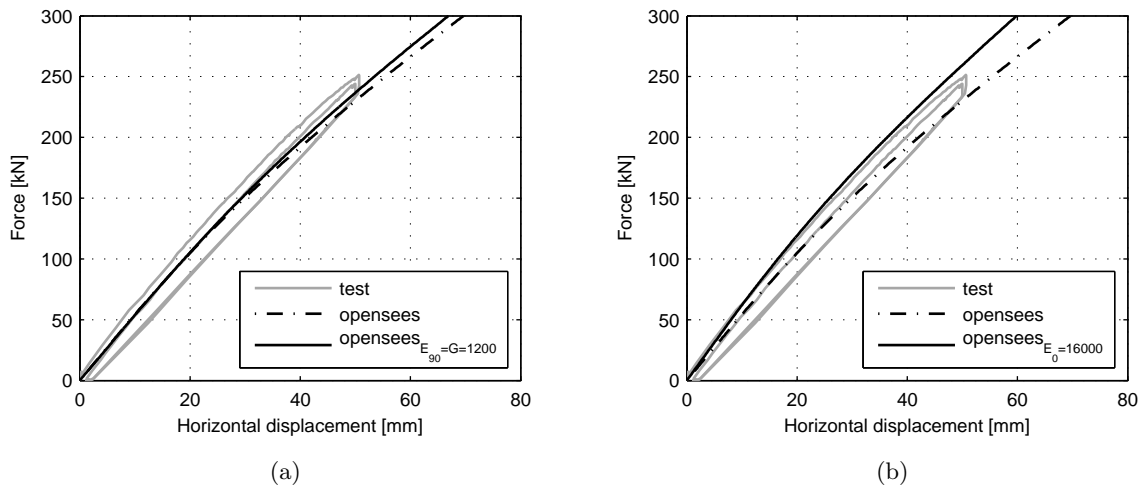
Figure 6.7: Comparison between the numerical and analytical model and the results from the pushover tests 6.7(a): OpenSees-model with $E_{90} = 1200$ MPa and $G = 1200$ MPa 6.7(b): OpenSees-model with $E_0 = 16000$ MPa

The significance of the Poisson's ratio was also studied. An increase of the value for the column from 0.059 to 0.1 or 0.15 only has a minor effect on the pushover curve as can be seen in Figure 6.8. The stiffness increases and matches the test results better as the Poisson's ratio is increased.

However, an increase from 0.05 to 0.15 corresponds to an increase of 200% of its initial value. The parameter is therefore not critical regarding its sensitivity.
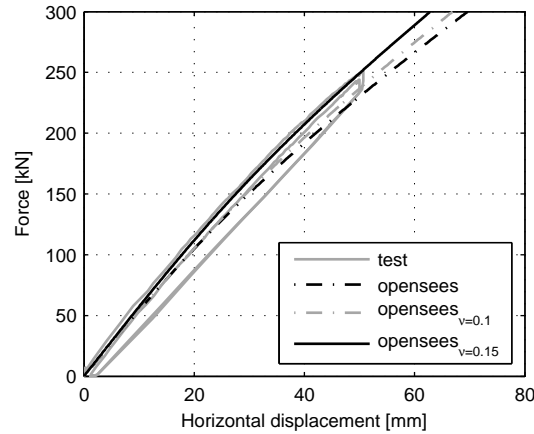
Figure 6.8: Comparison between the numerical model for different values of the Poisson's ratio and the test results

6.3   Discussion

The numerical model is able to predict the behaviour of post-tensioned timber connections reasonably well. The model could verify the results obtained from the simplified analytical approach.

In addition to the analytical model, the OpenSees model shows a deterioration in stiffness as the tendon force gets smaller. Figure 6.9 shows the pushover curves obtained from the OpenSees model together with the test results for tendon forces of 400 kN and 500 kN. The numerical model was generated with a stiffer column ($E_0 = 16000$ MPa) and includes the stiffness parallel to the grain of the beams ($E_0 = 11000$ MPa).
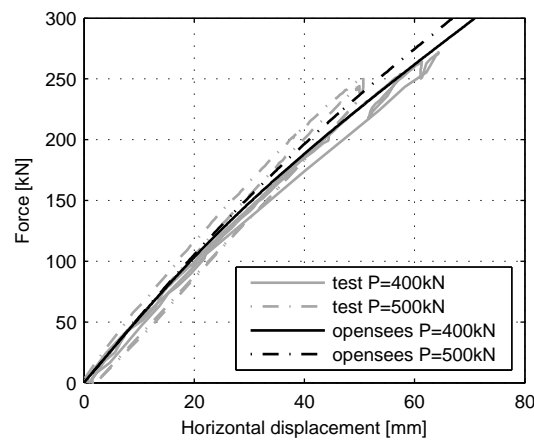
Figure 6.9: Comparison between the numerical model and the test results for tendon forces of 400 and 500 kN

Chapter 7

Long-term behaviour

The stiffness of the timber connection depends on the post-tensioning force as was demonstrated in the previous chapters. It could be shown that the stiffness increases as the force increases and vice-versa. However, losses in post-tensioning force and therefore a reduction in connection stiffness are not avoidable. It is thus crucial to estimate the losses in post-tensioning force over the service life of the structure. Therefore, some small-scaled long-term tests have been performed since 2012. Several beam and beam-column specimens were post-tensioned in different climatic conditions as can be seen in Figure 7.1.

<center>(a)   (b)</center>
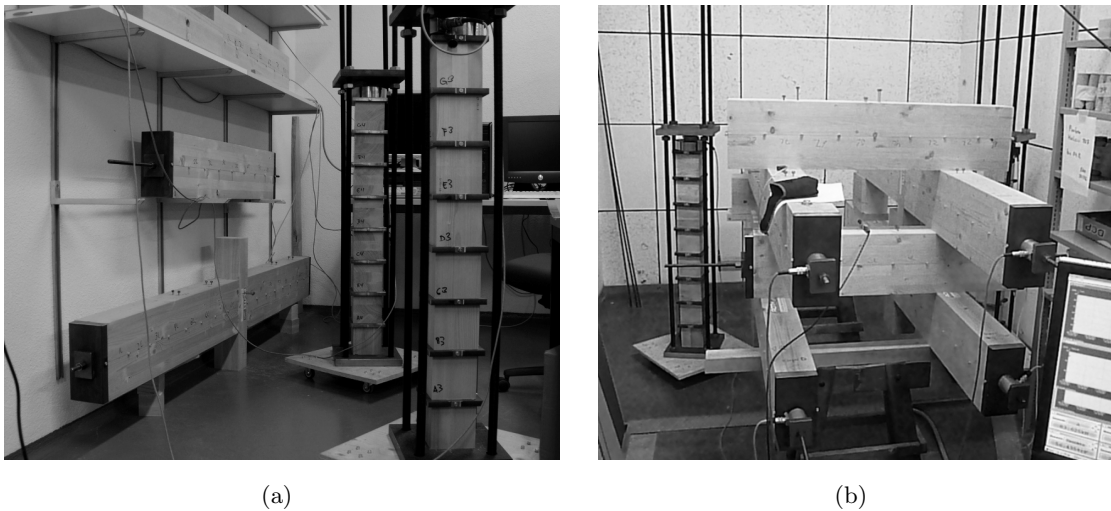
Figure 7.1: 7.1(a): Tests in controlled environment with beam-column and beam specimen (left) and stacked block specimens (right) 7.1(b): Tests in uncontrolled environment with beam-column and beam specimen and stacked block specimens

These tests are evaluated in this chapter. The presented tests are based on earlier publications [80], [81], however, an additional year of data as well as the results of a test specimen placed outdoors is included herein.

The tendon force is measured for each specimen and extrapolated in order to estimate the loss of post-tensioning force for such connections at the end of their service lives, i.e. after 50 years [82].

7.1   Specimens and test setup

The tests are conducted using different kinds of specimens:

- Block specimens

- Beam-column specimens (frame specimens)

- Beam specimens

- Dummy specimens (unloaded beam and column specimens)

These specimens were positioned in different climatic environments as summarised in Table 7.1.

Table 7.1: Overview of specimens and climatic conditions

Specimen	Controlled conditions	Uncontrolled conditions	Outdoors
Block	2×7	2×7	-
Beam-column	1	4	1
Beam	1	1	-
Beam dummy	1	1	-
Column dummy	1	1	-

7.1.1   Block specimens

Small blocks made of glulam (European ash and Norway spruce), with dimensions of $120 \times 120 \times 120$ mm are used to estimate the creep coefficient. The blocks consist of three lamellae and two adhesive layers. All specimens were stored in a climate chamber at 20°C and 65% relative humidity in order to reach the equilibrium moisture content before the tests were started. One set of specimens was left in the climate chamber (controlled conditions) whereas a second set was moved to a workshop (uncontrolled conditions).

The glulam blocks made of ash are loaded perpendicular to the grain (as is the column in the beam-column-specimens), the glulam blocks made of spruce are loaded parallel to the grain (as is the beam in the beam-column-specimens).

In order to apply a constant stress of 3 MPa on all blocks, they were stacked alternately with steel plates, as shown in Figure 7.2 on the right hand side. The load is applied with four steel rods and can be measured with a load cell, positioned on top of the block specimens. The load level chosen corresponds to approximately 30% of the strength perpendicular to the grain according to the EN 338 [62].

During the tests the load level had to be checked regularly and adjusted in order to keep the load constant. The distance between the steel plates, which separate the block specimens from each other, was measured periodically. From these measurements it is possible to obtain values for the creep coefficients parallel to the grain (spruce) and perpendicular to the grain (ash).

Two dummies are also placed in the climate chamber and the workshop as control specimens.

The dummies are also needed to measure the moisture content in the timber. The measurements are made in a depth of 30 mm and 60 mm, respectively.
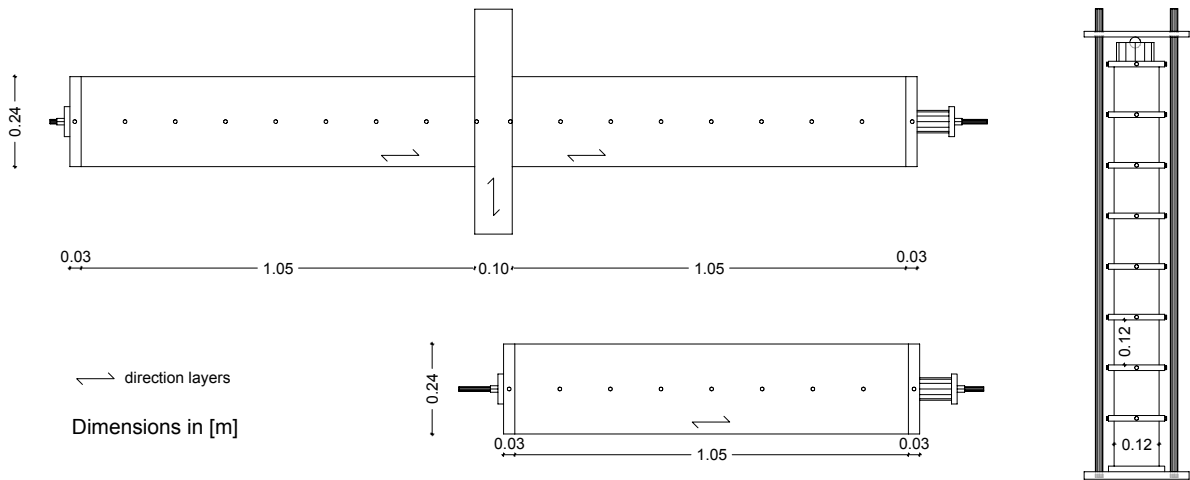
Figure 7.2: Beam-column specimen, beam specimen and stacked block specimens

7.1.2 Beam-column specimens

The beam-column specimens (on the left hand side in Figure 7.2) are made up of a column and two beams. The dimensions of a beam are 1050 × 120 × 240 mm (length × width × depth), those of the column are 600 × 120 × 100/160/240 mm (length × width × depth = distance between the beams). Two specimens have a column with a different to check whether it has an influence on the loss in tendon force (since more timber is loaded perpendicular to the grain). For this reason, a factor λ will be introduced, which is the ratio of the length of timber loaded perpendicular to the grain to the total length of the specimen.

$$\lambda = \frac{l_\perp}{l_\parallel + l_\perp} \tag{7.1}$$

Where $l_\perp$ and $l_\parallel$ are defined by the depth of the column and the length of the beams, if the widths of the beams and the columns are the same (120 mm):

$$l_\perp = depth_{column} \tag{7.2}$$

$$l_\parallel = 2 \cdot length_{beam} \tag{7.3}$$

There are therefore three different values for the factor λ, which cover the range that can typically be found in real timber frame structures: 4.5%, 7.1% and 10.2%.
All specimens are post-tensioned to an initial compressive stress of 3 MPa. A load cell measuring

the tendon force is placed between the anchorage of the tendon and the steel plate. Furthermore, the strains are measured along the specimen with a demec gauge (points alongside the specimens in Figure 7.2). These strains allow the estimation of the Young's modulus of the specimen after post-tensioning.

The moisture content of each beam is measured at three positions (mid-span and at one third of the span from the edge) at a depth of 60 mm. The moisture content of the column is measured at a depth of 30 mm.

7.1.3 Beam specimens

The beam specimens are post-tensioned to 3 MPa initial compressive stresses as well. The beams are the same as the ones used for the beam-column specimens with dimensions of $1050 \times 120 \times 240$ mm. The moisture content is measured as described in the previous subsection.

7.1.4 Dummies

The dummy specimens are beams and columns, which are not post-tensioned. The beams have the same dimensions as the ones being post-tensioned (see previous subsection). The dimensions of the columns are $600 \times 120 \times 100$ mm.

The dummies are used to estimate the influence of the climate (shrinkage and swelling). The moisture content was measured at mid span and at one third of the span in depths of 15 mm, 30 mm and 60 mm for the beam specimen and in a depth of 30 mm for the column specimen.

7.1.5 Tendon

Within this test series, conducted to estimate the long-term behaviour of post-tensioned timber structures, a high-strength steel rod (yield strength 1070 MPa) was used instead of a tendon. Since the relaxation is not a part of the testing program, it is easier to use the rods, because the force can be applied without needing a special anchorage (a steel plate and a screw nut are sufficient).

Values for the relaxation are usually given by the suppliers of the tendon for a stress level corresponding to 70% of the tensile strength. The tendon used for the post-tensioned timber frame described in Chapter 5 has a maximal relaxation of 2.5% [83]. This value is much smaller than the expected losses due to creep and mechano-sorptive creep effects and can therefore be neglected.

7.2 Experimental programme

The experimental programme includes tests in three environments:

- Uncontrolled environment: The temperature and relative humidity (RH) are not controlled, daily and seasonal changes occur

- Controlled environment: The temperature is regulated to 20°C, the relative humidity is kept at 65%

- Outdoors: The temperature and relative humidity (RH) are not controlled, daily and seasonal changes occur

7.2.1 Tests in the controlled environment

The controlled environment provides constant climatic conditions, where neither the temperature nor the relative humidity should change. However, the air-conditioning system had to be renewed in the climate chamber, which was used for the tests described herein. The change resulted in an increase of relative humidity after 160 days from 65% to 70%, as shown in Figure 7.3. The short drop in relative humidity after 29 days is due to a power cut, which lasted for a few hours. Moreover, a second failure in the air conditioning system occurred after approximately 340 days, which resulted in a further modification of the system, whereas the scatter in relative humidity increased afterwards.

The relative humidity was reduced to 60% after 460 days before starting with cycles of 60% ± 15%, i.e. generating an increase of the relative humidity up to 75% before reducing the value to 45%. The cycling of the relative humidity was aborted after two cycles lasting 14 days each due to problems with the measuring equipment, which were induced by the high moisture content in the air.

The temperature is kept at a constant value of 20°C, without any noticeable alterations. The temperature increased to 25°C while the cycles in relative humidity were generated. The increase in temperature was not accounted for during the test analysis.

Two sets of block specimens (one loaded parallel to the grain, one loaded perpendicular to the grain) as well as a post-tensioned beam and beam-column specimen are positioned in the climate chamber. Furthermore, a dummy beam and column specimen is placed there as well. The samples were conditioned to a moisture content of approximately 12 %, corresponding to the environmental relative humidity RH = 65 %, before the tests were started. The EN 789 [84] dictates, that the mass difference of a sample has to be smaller than 0.1% within 24 hours. The time span was increased for these tests to over a month. This means that the mass difference measured in a month's time was smaller than 0.1%. The largest difference in mass, recorded between the 18th of September and the 30th of October, was 0.09%. The specimens reached therefore the equilibrium moisture content before the tests were started.
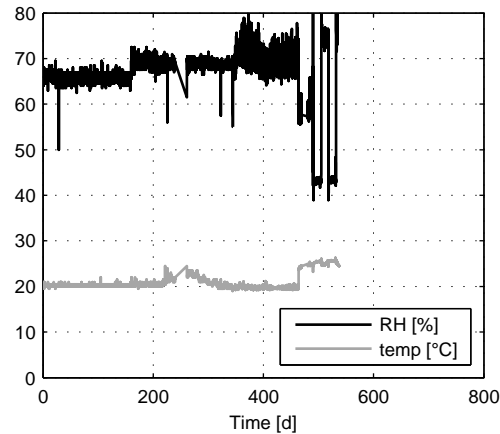
Figure 7.3: Climate in the controlled environment. The relative humidity varies from 63 to 70% and is clylced after 46 days between 45% and 75%. The temperature is constant at 20°C, increasing to 25°C during the cycles after 460 days

7.2.2 Tests in the uncontrolled environment

Most specimens are placed in the workshop, where the climate is not controlled. There are four beam-column specimens, one beam specimen as well as two sets of block specimens. Additionally two dummy specimens are in the workshop as well, a beam and a column which remained unloaded. The relative humidity varies, as does the temperature. The humidity lies between 30 and 70%, the temperature between 22 and 25°C (Figure 7.4). The change in temperature was neglected in the test evaluation.
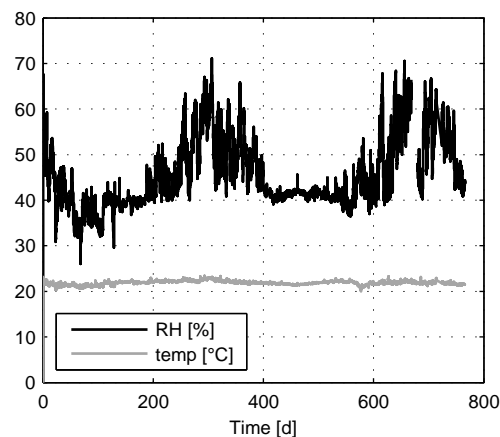
Figure 7.4: Climate in the uncontrolled environment

The tests began in autumn 2012, on the 4th of October. The humidity decreases during fall and is low in winter. In spring, the relative humidity starts to increase again and remains high during the summer. This cycle repeats itself after one year, as can be seen in Figure 7.4.

7.2.3 Test outdoors

One beam-column specimen is placed outdoors under a roof. However, the specimens were covered with snow several times and got wet if the weather was rainy and windy. The beam-column specimen has a column depth of 100 mm. It is - geometrically - identical to the beam-column specimen in the climate chamber and post-tensioned to the same initial stress of 3 MPa. However, the end faces of the beams are sealed with varnish. The idea is to reduce the reactivity due to a change in relative humidity of the environment since the moisture can not penetrate the timber from the front side any more where it is most reactive to a change in relative humidity. The test with this specimen started on the 23rd of January 2013. The climate is recorded and shown in Figure 7.5. The temperatures are low during winter, increase in the spring, and drop again in the fall. The relative humidity scatters from 50% to 90%. The tests were stopped after approximately 500 days.
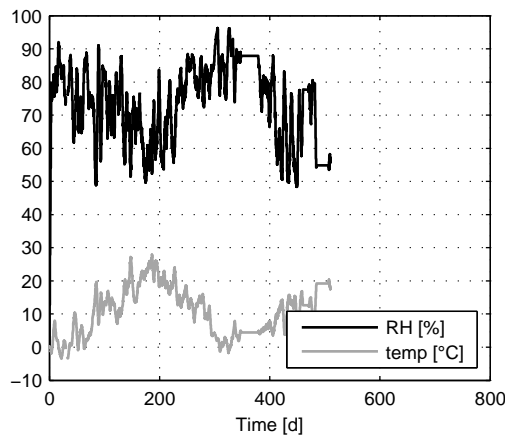
Figure 7.5: Climate outdoors

7.2.4 Tendon force losses and their mechanisms

The loss in pre-stressing can be attributed to different phenomena:

- Tendon relaxation

- Creep parallel to the grain

- Creep perpendicular to the grain

- Mechano-sorption parallel to the grain

- Mechano-sorption perpendicular to the grain

- Shrinkage and swelling parallel to the grain

- Shrinkage and swelling perpendicular to the grain

Not all phenomena occur in every environment for every specimen. For example, a post-tensioned beam does not experience any phenomena perpendicular to the grain. The mechano-sorption only occurs in the uncontrolled environment, since the relative humidity has to change for it to occur [85]. Table 7.2 summarizes the phenomena according to the load (post-tensioned or unloaded) and climate (controlled or uncontrolled). It can be seen, that the phenomena can - in theory - be separated, if the specimens behave similarly.

The differentiation between phenomena parallel and perpendicular to the grain can be achieved by comparing the beam specimen (only parallel to the grain) with the beam-column specimen (loaded parallel and perpendicular to the grain). It is therefore - again, theoretically - possible to separate the losses perpendicular to the grain.

Table 7.2: Overview of phenomena causing tendon force losses

Climatic condition Phenomena	Controlled Loaded	Controlled Dummies	Uncontrolled Loaded	Uncontrolled Dummies
Creep	x		x	
Mechano-sorption			x	
Shrinkage/swelling			x	x

Loss due to relaxation of the tendon is not taken into account, since the load on the tendon corresponds to only 25% of its yield load. The relaxation is therefore much smaller than 2.5% [83] and can be neglected.

7.3   Test results - small block tests

7.3.1   Moisture content

The moisture content in the block specimens was measured periodically (in both environments). The results are presented in Figure 7.6(a), together with the relative humidity in the environment (Figure 7.6(b)).

The moisture content of the block specimens in the controlled environment is nearly constant during the first 28 days before it drops due to problems with the air conditioning. Afterwards it remains constant until the relative humidity in the controlled environment was increased after 150 days. The reason for this is the installation of a new air conditioning system, causing the relative humidity to increase from 65% to 70%. A gap is noticeable after approximately 240 days, where no measurements of relative humidity could be recorded. The recording was re-started again after approximately 260 days. The relative humidity scatters stronger after 340 days than before due to a technical problem. After 460 days, the humidity was changed to 60% before varying the relative humidity between 45% and 75%, i.e. 60% ± 15%. The tests were stopped after two cycles were completed, each cycle lasting 14 days.

The temperature is relatively constant at 20° and it is assumed, that the temperature does not influence the behaviour of the specimens very much and is therefore negligible.

The moisture content of the specimens is nearly constant, the value for the ash block lies be-
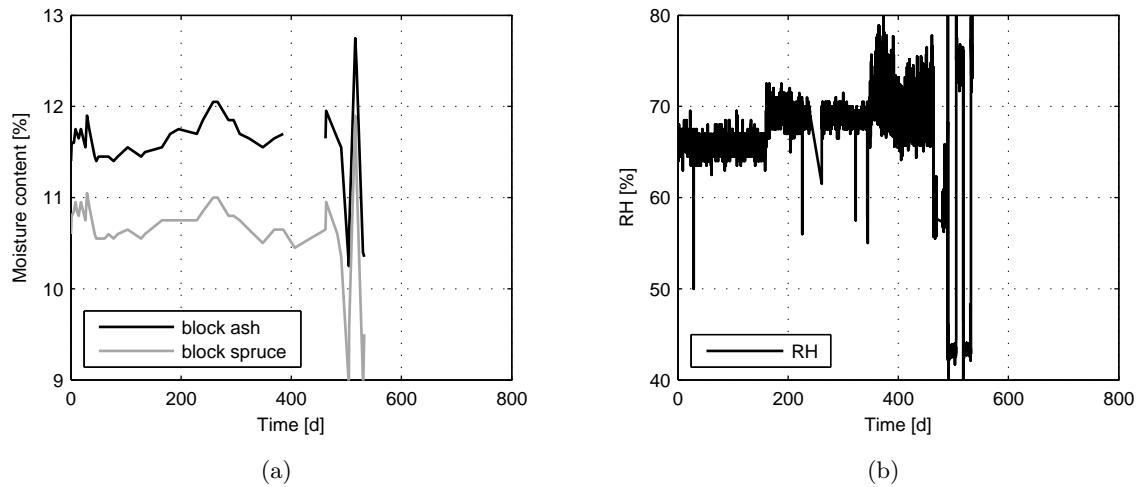
Figure 7.6: 7.6(a): Measured moisture content of the block specimens 7.6(b): Relative humidity in the controlled environment

tween 11.5% and 12% the one for the spruce block between 10.5% and 11%. During the relative humidity cycles the values for the ash vary from 10% to 13% the ones for the spruce from 9% to 12%. The moisture content correlates well with the relative humidity in the environment for both types of specimens.

The moisture content for the block specimens in the uncontrolled environment is presented in Figure 7.7(a) and together with the relative humidity in the environment (Figure 7.7(b)).
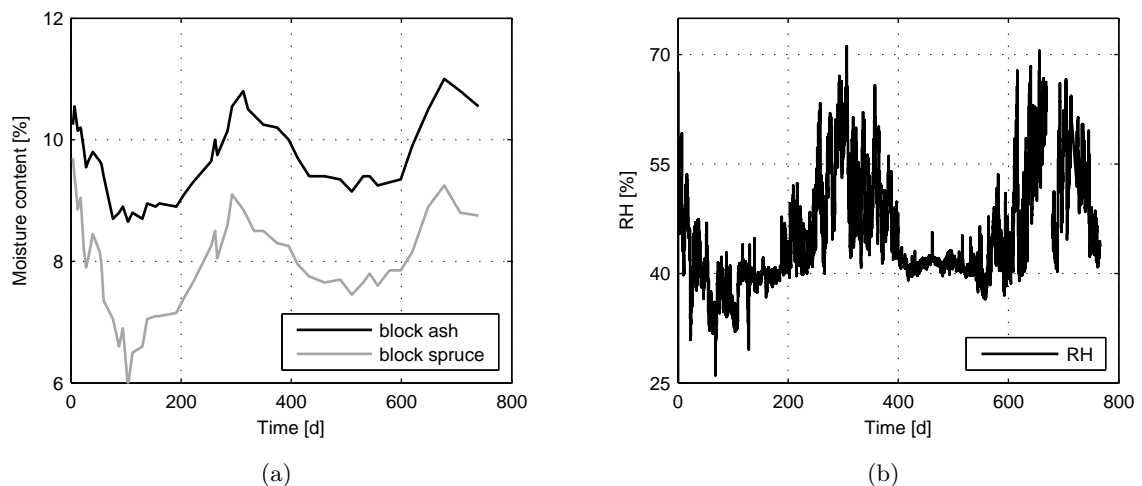
Figure 7.7: 7.7(a): Measured moisture content of the block specimens 7.7(b): Relative humidity in the uncontrolled environment

The relative humidity in the environment drops during the first 100 days of the test and is then constant up to 200 days. Afterwards it starts to increase and is high up to one year after the

beginning of the tests. The cycle start to repeat itself after one year. The relative humidity reflects the different seasons; the tests began in fall, where the relative humidity was still high. It fell during winter and started to increase in spring and was high during the summer months. The moisture content in the uncontrolled environment drops during the first 100 days of the test and reaches values of 6% for the spruce specimens and 9% for the ash specimens. Afterwards the moisture content started to increase again in the summer where values of 9% and 11% were observed for the spruce specimens and ash specimens, respectively. The relative humidity in the uncontrolled environment correlates well with the moisture content in the block specimens.

7.3.2 Creep tests

The pressure could be held constant very well at 3 MPa in the case of the specimens in the controlled environment. However, in the uncontrolled environment, it was much more difficult to keep the pressure at a constant value, due to the fact that adjustments needed to be done on a daily basis. Nevertheless, it was possible to keep the pressure between 2.8 and 3.2 MPa with a few exceptions as can be seen in Figure 7.8.
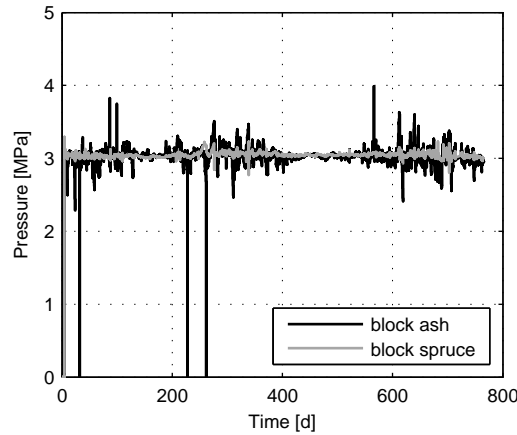
Figure 7.8: Pressure during the creep tests on the block specimens in the uncontrolled environment

The distance u between the blocks is measured periodically (see Figure 7.9). Steel plates are positioned between the single blocks with special measuring points for the demec gauge. The distance is measured from all sides, i.e. four measurements for one block.

With the obtained data, it is possible to define the creep coefficient parallel (for the spruce specimens) and perpendicular to the grain (for the ash specimens):

$$\phi = \frac{u - u_0}{u_0} - 1 \qquad (7.4)$$

With u being the actual deformation (current measured value) and u_0 as the initial elastic deformation after loading the specimens.
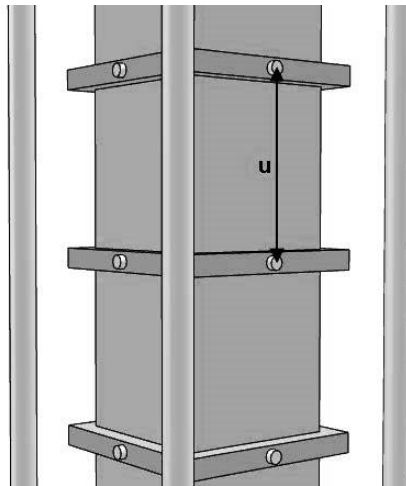
Figure 7.9: Distance measurements of the block specimens

Creep tests in the controlled environment

The results of the creep tests in the controlled environment are presented in Figure 7.10 where the average values for the creep coefficient are plotted for the spruce and ash blocks.
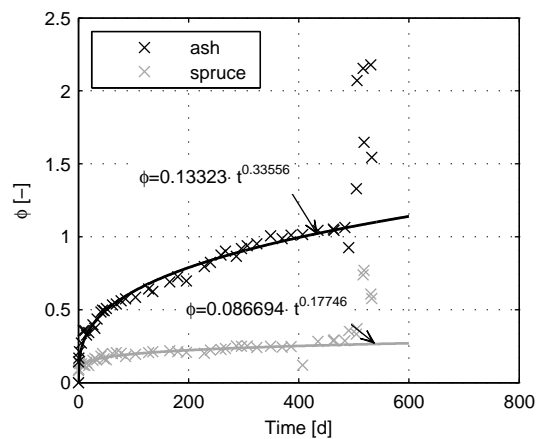
Figure 7.10: Pure creep for the block specimens in the controlled environment

These values take the effect of shrinkage and swelling into account, and represent, therefore, the pure creep coefficients, i.e. the effect of shrinkage and swelling was eliminated by using the dummy specimens. These coefficients can be fitted well with a function of the type $y = ax^b$. The extrapolated creep coefficient for ash after 50 years would correspond to 3.0, wheras the value for the spruce specimens would correspond to 0.48.

The large difference between the spruce and ash blocks is due to the direction of the load. Spruce is loaded parallel to the grain, with a ratio of the applied load to the failure load (assuming a strength class C24 [62] and variation between mean value and characteristic value according to JCSS [86]) of:

$$\frac{\sigma}{f_{c,0,mean}} = \frac{3}{21 \cdot 1.226} = 0.12 \tag{7.5}$$

The ash specimens are loaded perpendicular to the grain. The lower strength perpendicular to the grain results in a higher load level. Assuming a strength class D40 [62] and variation between mean value and characteristic value according to JCSS [86] the following ratio can be calculated:

$$\frac{\sigma}{f_{c,90,mean}} = \frac{3}{8.3 \cdot 1.197} = 0.30 \tag{7.6}$$

The curve fitting for both kind of specimens was performed without taking the values that were recorded during cycling the relative humidity in the environment into account, i.e. without the last seven measurements. These last measurements are much higher compared to the rest of the data set, since some mechano-sorptive creep occurred due to the change in relative humidity in the environment.

Creep tests in the uncontrolled environment

The creep tests in the uncontrolled environment include the mechano-sorptive creep (ms-creep) and pure creep. The shrinkage and swelling was eliminated by taking the measurements from the dummy specimens into account. The average creep coefficients for the ash and spruce blocks are shown in Figure 7.11.
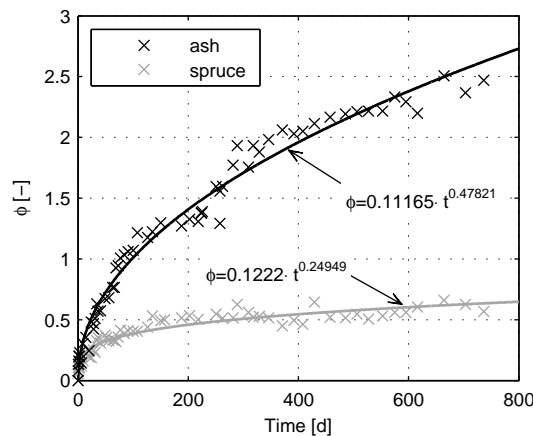
Figure 7.11: Coefficients for the block specimens in the uncontrolled environment, including creep and ms-creep

Evaluation of the creep tests

The measured values from the creep tests allow estimating the influence of the mechano-sorptive creep, at least in theory. If the creep values from the controlled environment are subtracted from

the values measured in the uncontrolled environment the mechano-sorptive creep is isolated. I.e. the curves in Figure 7.10 have to be subtracted from those in Figure 7.11 in order to obtain the curve for the mechano-sorptive creep itself.

The influence of the mechano-sorptive creep is shown in Figure 7.12 for ash loaded perpendicular to the grain (black shaded area) and spruce loaded parallel to the grain (grey shaded area).
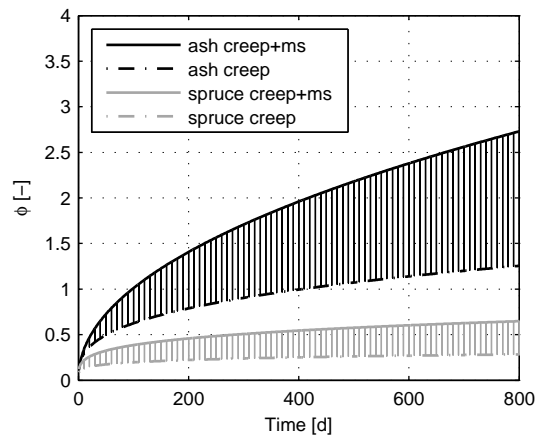
Figure 7.12: Creep and mechano-sorptive creep for the spruce and ash blocks

It is noticeable, that the mechano-sorptive creep is larger than the pure creep. By extrapolating the estimated curves for 1, 10 and 50 years, the values shown in table 7.3 and 7.4 are generated.

Table 7.3: Extrapolated values for creep coefficient for ash loaded perpendicular to the grain

	1 year		10 years		50 years	
pure creep	0.96	51%	2.09	37%	3.58	29%
ms creep	0.92	49%	3.55	63%	8.60	71%
total	1.88	100%	5.64	100%	12.18	100%

Table 7.4: Extrapolated values for creep coefficient for spruce loaded parallel to the grain

	1 year		10 years		50 years	
pure creep	0.25	55%	0.37	50%	0.49	46%
ms creep	0.28	45%	0.58	50%	0.92	54%
total	0.53	100%	0.95	100%	1.41	100%

The values are only rough estimations, since the tests have so far only be ongoing for two years. Furthermore, the values scatter and the block specimens are rather small, making them more vulnerable to changes in relative humidity compared to a full scaled specimen.

7.4 Test results - beam and frame specimens in the controlled environment

7.4.1 Moisture content

The moisture content in the specimens was measured periodically. The results are shown in Figure 7.13.
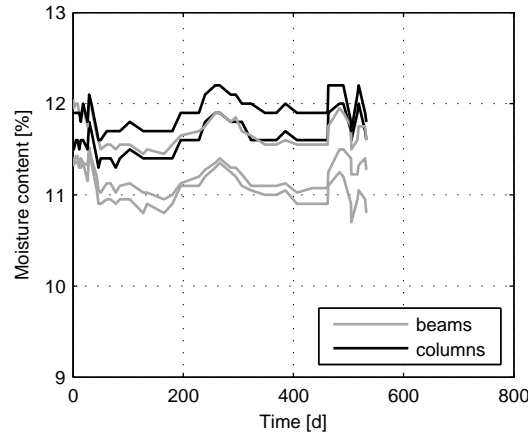
Figure 7.13: Measured values for the relative humidity and moisture content in the controlled environment

The moisture content for the beam specimens is approximately $11\% \pm 0.5\%$. The same accounts for the columns made of ash where the value is approximately 12%. The higher moisture content for the ash was already noticeable with the small block specimens. The cyclic relative humidity starting after 460 days does not seem to have a significant influence on the moisture content of neither the beams nor the column.

7.4.2 Losses in tendon force

The recorded tendon forces for the beam and the beam-column specimen are presented in Figure 7.14. Both specimens were loaded to approximately 86 kN. The loss rate is large in the first few weeks and decreases after that. An increase in tendon forces is also noticeable after 160 days, which is due to the increase in relative humidity.

In order to extrapolate the losses, a curve is fitted to the measured values. Figure 7.15 shows the fitted curves and their equations for the ratio between the tendon force and the initial tendon force over time. The equations indicate, that the beam-column specimen is going to experience more loss in tendon force than the beam specimen. This is due to the fact that the former specimen contains a column which is loaded perpendicular to the grain as well as two beams.

The extrapolated losses are listed in Table 7.5 for the beam and beam-column specimen. The losses after 50 years are only 4% for the beam specimen and approximately 13% for the beam-column specimen.
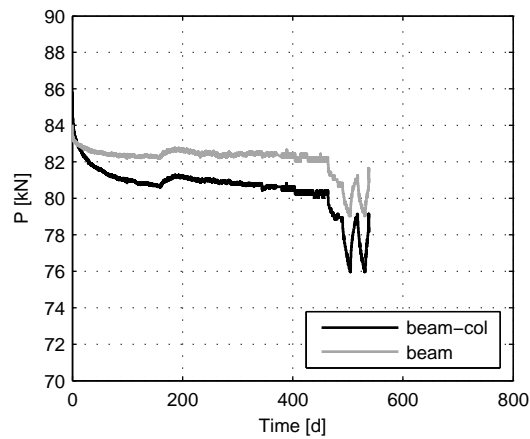
Figure 7.14: Tendon force over time in the controlled environment
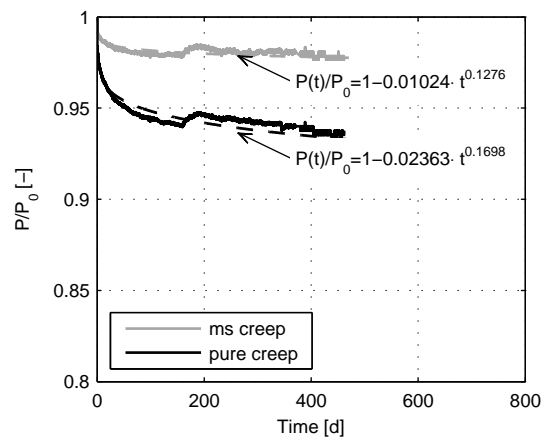
Figure 7.15: Tendon force normalized with initial tendon force in the controlled environment including fitted functions for extrapolation

Table 7.5: Extrapolated losses in tendon force in the controlled environment

Years	Beam specimen	Beam-column specimen
1	0.98	0.94
10	0.97	0.90
50	0.96	0.87

7.5 Test results - beam and frame specimens in the uncontrolled environment

7.5.1 Moisture content

The moisture content in the specimens was measured periodically. The results are shown in Figure 7.16. The measurements taken on the beams (from all beam-column specimens as well as the beam and dummy specimens) are plotted in Figure 7.16(a) whereas the measurements taken on the columns are plotted in Figure 7.16(b).

(a)   (b)
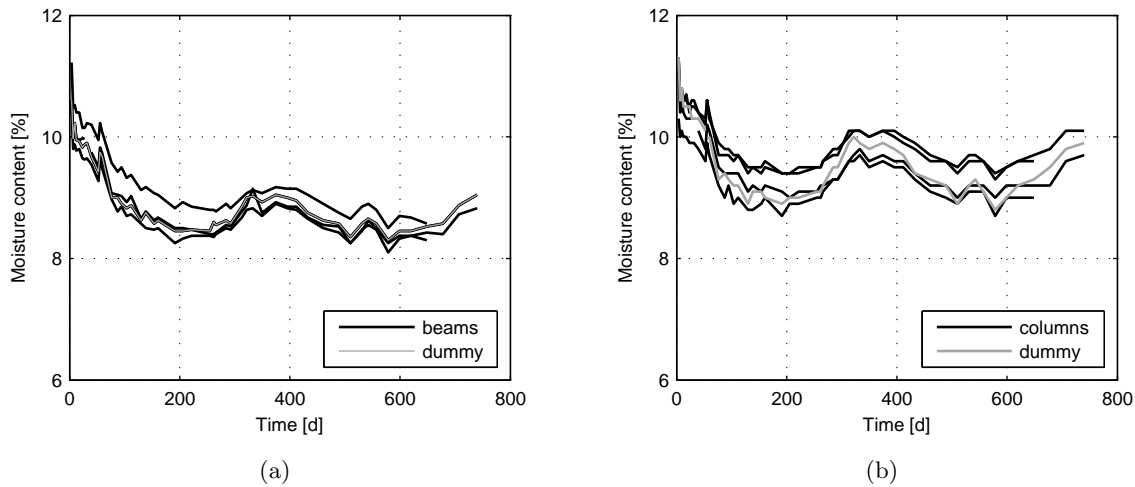
Figure 7.16: Moisture content for post-tensioned specimens in the uncontrolled environment 7.16(a): Measurements for the beams including the dummy beam 7.16(b): Measurements for the columns including the dummy column

The moisture content of the ash columns is slightly higher than the moisture content of the spruce beams as could already be observed with the block specimens and with the larger specimens in the controlled environment. The values - for the columns and beams likewise - follow the trends given by the relative humidity in the uncontrolled environment.

7.5.2 Losses in tendon force

The recorded tendon forces for the beam and beam-column specimens are presented in Figure 7.17. The legend describes the kind of specimen and the depth of the column.
All specimens show a high loss rate at the beginning until 100 days after post-tensioning, when the loss rate slows down. After 200 days an increase in tendon force is noticeable. The force is high up to one year after the tests began before a second drop in tendon force occurred. The tendon force correlates with the relative humidity of the environment and therefore with the seasons. The largest drops occur in autumn when the relative humidity in the environment drops.
One specimen with a column depth of 100 mm was re-stressed after 140 days (black line in Figure

7.17 with the drastic increase in tendon force) to check whether re-stressing a post-tensioned timber connection is beneficial. Two of the specimens were disassembled after 650 days and the tests continued with a reduced number of specimens.
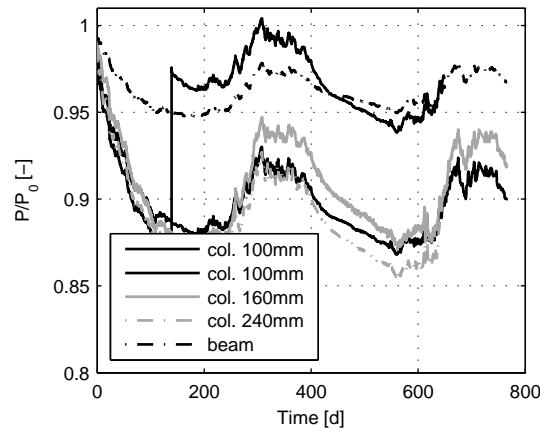
Figure 7.17: Tendon force over time in the uncontrolled environment

The graphs in Figure 7.17 are all similar. The difference between the beam-column specimens is small. However, it can be seen that the specimens with a larger column react more sensitively to a change in relative humidity, i.e. the beam-column specimen with a column depth of 160 mm (grey line in Figure 7.17) overtakes the specimen with a column depth of 100 mm twice; once during the first 100 days, and again when the tendon force increases after 200 days. This behaviour is less distinct for the specimen with a column depth of 240 mm (grey dash dotted line). This specimen showed a nearly identical behaviour as the specimen with a column depth of 100 mm up to the point of the second drop in tendon force after one year, which resulted in a larger loss in the specimen with the deeper column.

7.6 Test results - frame specimen outdoors

7.6.1 Moisture content

The moisture content measured in the beam-column specimen outdoors is plotted in Figure 7.18(a). The moisture content of the column is lower than the ones from the beams. This is due to the fact that the specimen was exposed to snow and sometimes rain. The moisture content in the beams was measured from the top (which got wet) whereas the moisture content in the column was measured from the side, which was more protected from snow and rain. The beam that was exposed the most is the one with the highest moisture content, represented by the dashed grey line in Figure 7.18(b).

The values all start at 8-9% before they begin to increase. The relative humidity is shown in Figure 7.18(b). There is some correlation between the relative humidity and the moisture content, a peak is for example noticeable in both plots after approximately 400 days. However, the trend of the moisture content shows a wetting tendency of the specimen. This is based on

the fact that the specimens were stored in the workshop in dry conditions before starting the test series outdoors.

| (a) | (b) |
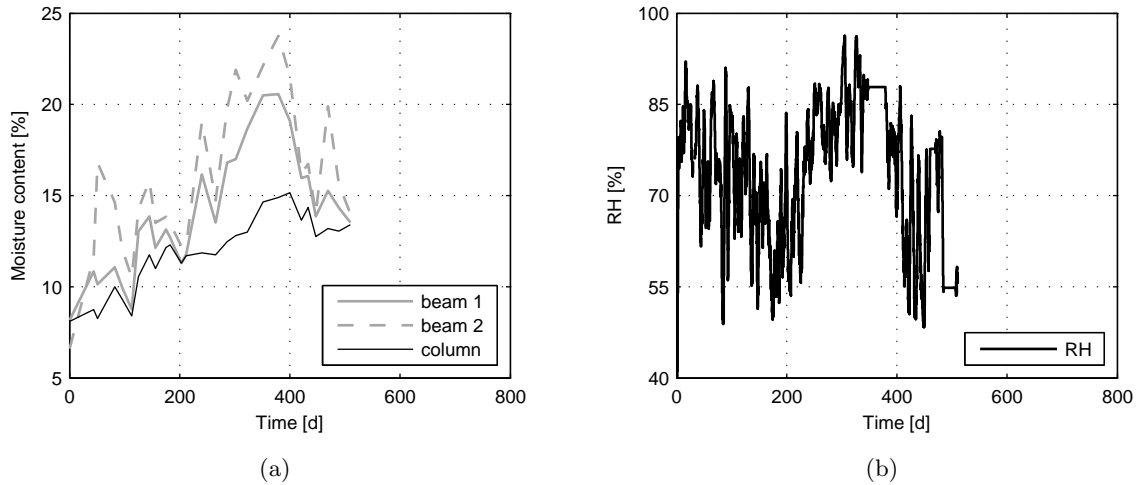
Figure 7.18: 7.18(a): Measured moisture content of the beam-column specimen positioned outdoors 7.18(b): Relative humidity in the environment outdoors

7.6.2   Losses in tendon force

The tendon force for the specimen positioned outdoors is shown in Figure 7.19. The tendon force starts to increase from the beginning of the test due to the fact that the specimen swells. Some decrease occurs after 100 days until the tendon force drops under its initial force after 200 days before it starts to increase again.
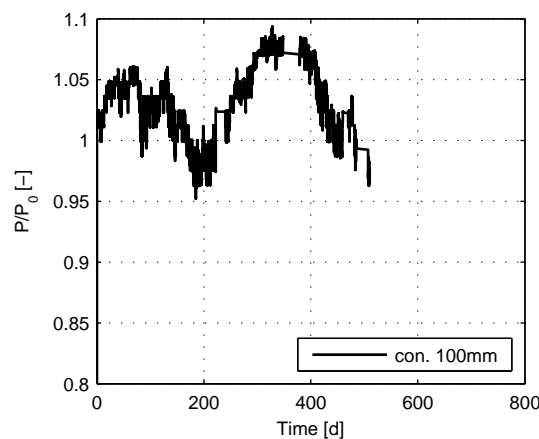
Figure 7.19: Tendon force over time for outdoor frame specimen

The fact that the tendon force barely drops under its initial value leads to the conclusion that the losses could be compensated by pre-stressing specimens that are too dry for their environment. The swelling of the specimen is therefore able to compensate for the loss in tendon force during the first stage where most of the losses occur.

7.7 Test evaluation - beam-column specimens

7.7.1 Influential factors

There are several factors influencing the losses in tendon force, as was already mentioned in Section 7.2.4.

Since mechano-sorption as well as shrinkage and swelling are both caused by a change in moisture content, these two phenomena are coupled and can not be separated directly. Due to the very small deformations and the scatter of the measurements on the dummy specimens (unloaded column and unloaded beam specimen) it was not possible to isolate the influence of shrinkage and swelling.

7.7.2 Pure creep

The influence due to pure creep can be estimated from the specimens in the controlled environment. By subtracting the loss of the beam specimen from the loss of the beam-column specimen twice, the loss in the column itself can be estimated. This procedure was done to obtain the graphs in Figure 7.20. The curves correspond to the mathematical functions defined in Figure 7.15.

(a)   (b)
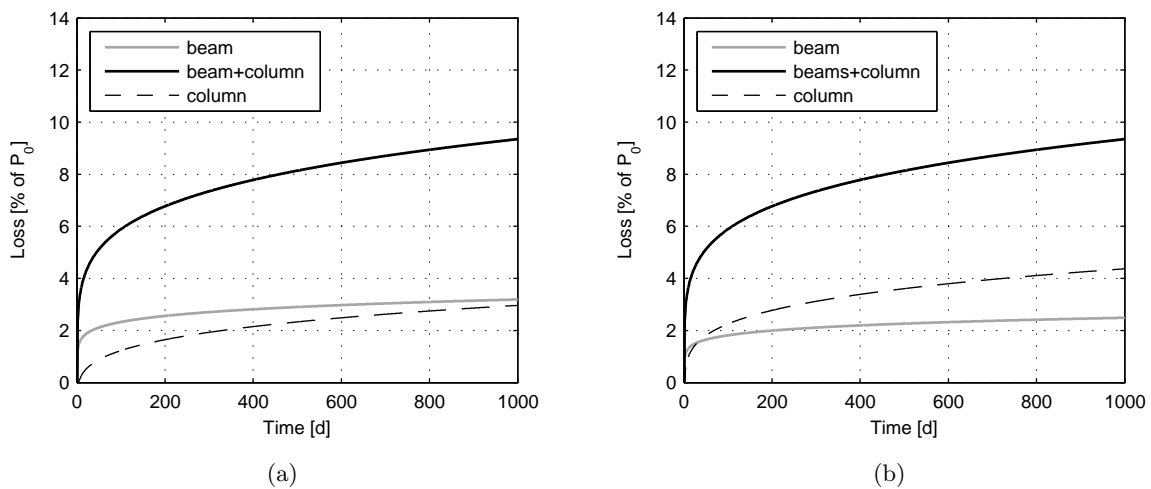
Figure 7.20: Loss of tendon force due to pure creep and tendon relaxation 7.20(a): Original data 7.20(b): Corrected data

It is noticeable, that the loss in the column is smaller than the loss in one single beam (Figure 7.20(a)). The prestressing loss in the beam is significant during the first few days. However, the loss rate drops rapidly afterwards. The initial high loss rate is most likely due to the softer areas at the edge of the beam specimen, where the two steel plates are mounted (see also Figure 7.21, where larger deformations were measured at the edge of the beams). The loss in the beam seems to be too large compared to the column. This could be due to the steel plates at the end of the beam specimen. The beam specimen has a steel plate on both ends, while the beams from the beam-column specimen only have a steel plate at one end. The - nearly rigid - steel

plate could be responsible for the large loss during the first days (locally crushing of the timber fibres).
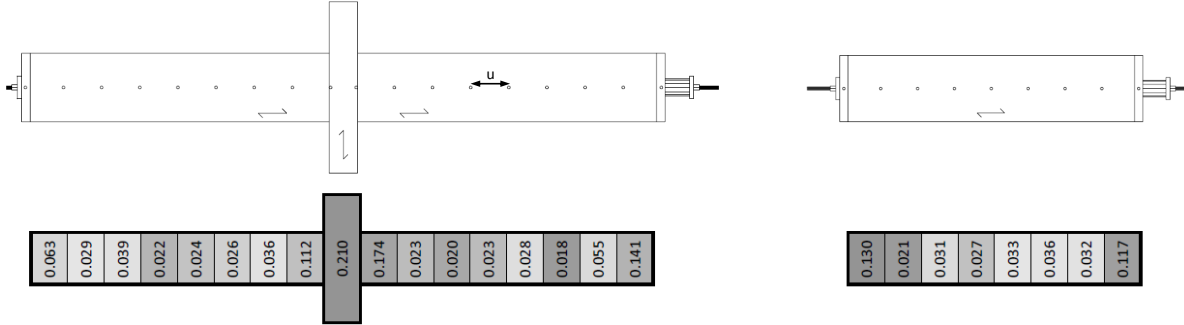
Figure 7.21: Measurement of the deformation u along the specimens and values for the elastic deformations

To account for this effect, a second graph was produced (Figure 7.20(b)), where the loss of the beam specimen was only subtracted 1.56 times from the loss of the beam-column specimen. The factor 1.56 can be obtained by expanding the post-tensioned beam specimen (Figure 7.21) to a length of 2.1 m (the same length as the two beams from the beam-column specimen) and only taking into account the soft areas once. This means, that the values for the displacement at the edges (0.130 and 0.117 mm in Figure 7.21) are taken into account once while the average value for the remaining part of the beam is taken into account 14 times, thus expanding the beam to a theoretical length of 2.1 m. The ratio between the total displacement of the beam with a length of 2.1 m and the total displacement of the actual beam with a length of 1.05 m corresponds to the factor of 1.56:

$$\frac{0.130 + 14 \cdot \left(\frac{0.021+0.031+0.027+0.033+0.036+0.032}{6}\right) + 0.117}{0.130 + 0.021 + 0.031 + 0.027 + 0.033 + 0.036 + 0.032 + 0.117} = 1.56 \qquad (7.7)$$

The results obtained with this procedure lead to larger losses in the column, which is more likely than the results obtained by subtracting the losses measured from the beam specimen twice from those measured in the beam-column specimen. However, only one beam specimen was available for the procedure and some uncertainty remains.

7.7.3 Mechano-sorption

Figure 7.22 shows the loss in post-tensioning force for the beam-column specimen in the climate chamber (black line) and the loss for the specimen in the uncontrolled environment (grey line). The dashed lines are fitted functions of the type $P(t)/P_0 = 1 - a \cdot t^b$. The fitted function for the specimen in the uncontrolled environment was fitted for the values 0/1 and the values after one year and two years. It is assumed, that the moisture content varies with a cycle of one year, i.e. the moisture content is the same after one year passed. This assumption seems

reasonable, since the average moisture content depends on the season, as can be seen in Figure 7.4. Therefore, the grey curve represents the total losses due to ms-creep, pure creep and tendon-relaxation.

With the curves presented in Figure 7.22 the losses due to creep and ms-creep can be predicted for different time periods. The results are summarised in Table 7.6.
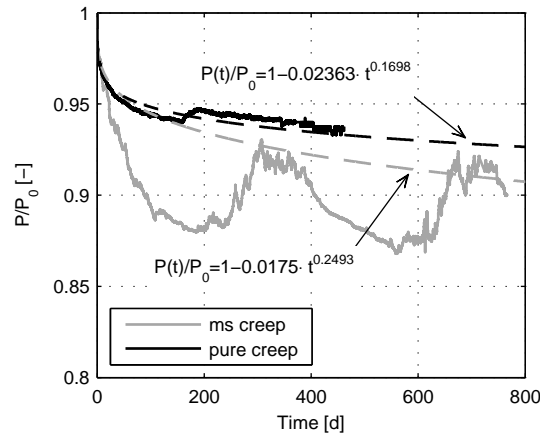
Figure 7.22: Loss of tendon force due to mechano-sorptive creep and tendon relaxation

Table 7.6: Losses in % of P_0 for the beam-column specimen (column depth 100 mm)

	1 year	10 years	50 years
pure creep	6%	10%	13%
ms creep	2%	4%	7%
total	8%	14%	20%

The mechano-sorptive creep has a much smaller influence on the total losses compared to the results obtained from the block specimens (Tables 7.3 and 7.4). This could be a size effect; since the blocks are much smaller than the beam-columns specimens, they are far more sensitive to a change in relative humidity and therefore also to the moisture content. This can also be seen by comparing Figure 7.6 with Figure 7.13 or Figure 7.7 with Figure 7.16. The change in moisture content is - next to the stress level - responsible for the ms-creep [85].

Nevertheless, the total loss after 50 years is estimated at 20%, which is more than the 15% [87] one would expect with a post-tensioned structure made of concrete.

The influence of shrinkage and swelling can also be estimated with the graphs shown in Figure 7.22. The vertical distance between the fitted function (dashed grey line) and the measured values (grey line) is due to a change in moisture content in the specimen itself. Shrinkage and swelling are therefore responsible for an additional loss up to approximately 5%. However, the loss is only temporary, since the climate is assumed to behave cyclic.

The influence of shrinkage and swelling also shows, that it is crucial for a post-tensioned timber structure to be conditioned before construction. If the timber has a moisture content, which is too high, additional losses will occur. The additional loss of 5%, which occurs approximately

200 days after the tests were started, is due to a change in moisture content of approximately 2%, as can be seen in Figure 7.16.

7.7.4   Column depth

The depth of the column does not seem to have an influence on the losses in post-tensioning force, or if so, it is very small. Figure 7.17 shows the losses over the time. The specimens with larger columns (i.e. 160 mm and 240 mm) show a more sensitive behaviour, especially the specimen with a column width of 160 mm (solid grey line in Figure 7.17). The loss rate is larger for this specimen than for the others, which could be due to the larger column.

In order to investigate the influence of the column depth on the loss of post-tensioning force the losses shall be compared. To do so, the influence of the stiffness has to be taken into account together with the different column depths. A specimen with a high combined stiffness (column and beam) will experience less losses in post-tensioning force than a soft specimen. The combined stiffness K_{sys} is defined as:

$$K_{sys} = \frac{1}{\frac{l_{\parallel}}{E_{\parallel} \cdot A_{\parallel}} + \frac{l_{\perp}}{E_{\perp} \cdot A_{\perp}}} \tag{7.8}$$

The stiffness is calculated for each specimen. The results are then compared to the specimen with a column depth of 100 mm (not re-stressed). All the results are summarised in Table 7.7.

Table 7.7: Combined stiffness in kN/m for the specimens

column width	stiffness	stiffness factor
100 mm	87512	1.0
100 mm (re-stressed)	76901	0.88
160 mm	68087	0.78
240 mm	66769	0.76

The multiplication of the loss of tension-force ΔP by the stiffness factor according to Table 7.7 should lead to a similar loss for all specimens. Figure 7.23(a) shows the graphs for the measured losses and Figure 7.23(b) shows the modified values, i.e the losses were multiplied with the corresponding stiffness factors.

The results in Figure 7.23(a) indicate that the losses are basically identical for all the specimens, i.e. the depth of the column does not seem to have an influence on the absolute measured losses. If the influence of the stiffness is eliminated (Figure 7.23(b)), it can be seen that the specimens with larger columns show less losses in tendon force. This finding is in contradiction with the analytical model used by Fragiacomo and Davies [46]. A possible explanation for the missing influence of the column depth could be the stress distribution in the column. A deeper column could distribute the stresses better than a thin column, since more timber is activated. This phenomenon can be taken into account in the analytical model, as was already mentioned in Chapter 3 (see also Figure 3.3).
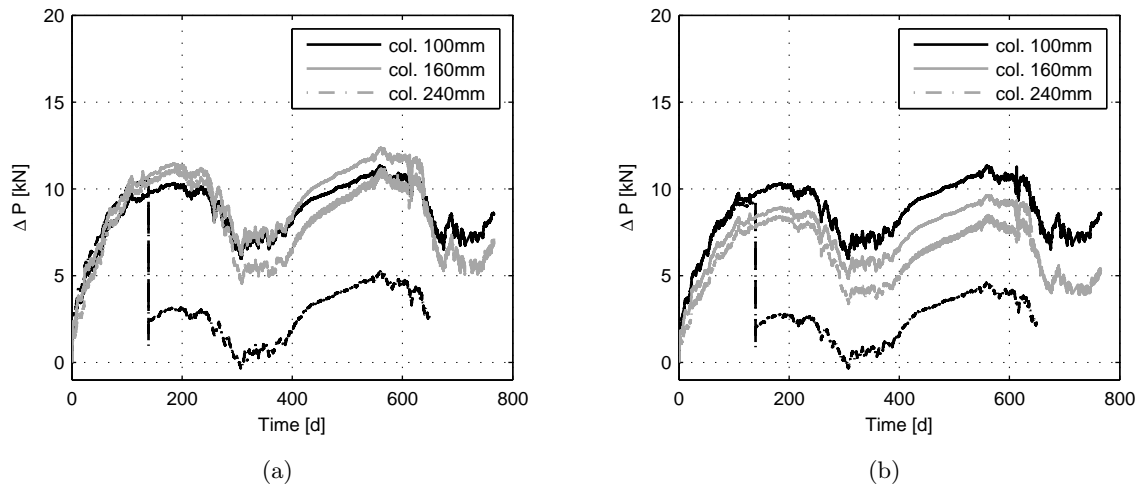
Figure 7.23: Loss of tendon force 7.23(a): Measured values 7.23(b): Modified values multiplied with stiffness factors

7.7.5 Re-stressing

Re-stressing does not seem to have a negative influence on the system. Figure 7.24 shows the loss in tendon force for the two columns with a depth of 100 mm, whereas the re-stressing was eliminated (i.e. the vertical discontinuity in Figure 7.23(b) was eliminated). It can be seen that the loss rate after re-stressing the system (i.e. after 140 days) increases a bit, due to the higher stresses acting on the specimen. The overall losses are very similar though, not indicating any additional loss in tendon force.
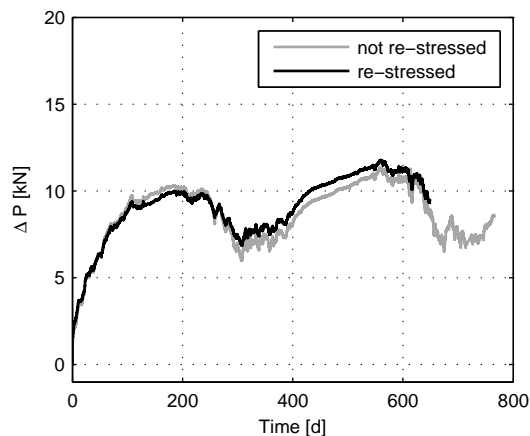
Figure 7.24: Loss in tendon force for the beam-column specimens with a column depth of 100 mm

The loss rates were calculated for the two specimens (re-stressed and not re-stressed) for two time periods in order to compare the losses numerically. The results are shown in Table 7.8. The differences are very small, and do not suggest that re-stressing the system leads to high loss rates which would make the re-stressing impractical. Re-stressing therefore makes sense in order to reduce the total amount of loss in post-tensioning force.

Table 7.8: Loss rate in N/day for different time periods

period [d]	not re-stressed	re-stressed
142 - 181	-0.15	-0.22
243 - 308	0.70	0.58

7.8 Analytical model for losses in the beam and beam-column specimens

A simple model to calculate the tendon force losses in post-tensioned timber structures was derived by Fragiacomo and Davies [46]. Equation (7.9) can be used without the term $\alpha \cdot r_p(t)$ to calculate the loss in tendon force, neglecting the influence of the relaxation of the tendon:

$$\Delta P(t) = P_0 \cdot \frac{\alpha \cdot r_p(t) + (1 - \lambda) \cdot \phi_\parallel(t) + n \cdot \mu \cdot \lambda \cdot \phi_\perp(t)}{\alpha + (1 - \lambda)\left[1 + \phi_\parallel(t))\right] + n \cdot \mu \cdot \lambda\left[1 + \phi_\perp(t)\right]} \tag{7.9}$$

With $\alpha = E_\parallel \cdot A_\parallel / (E_p \cdot A_p)$, $\lambda = l_\perp / (l_\parallel + l_\perp)$, $n = E_\parallel / E_\perp$ and $\mu = A_\parallel / A_\perp$.

However, the model does not take the influence of the environmental strains (temperature and shrinkage or swelling) into account. Therefore Equation (7.9) can only be compared with the results in the controlled conditions.

Fragiacomo and Davies [46] also provide a model which takes the environmental strains into account and can therefore be used to model the losses in the uncontrolled environment:

$$\Delta P(t) = \frac{P_0 \cdot \left\{ \frac{l_\parallel \cdot \phi_\parallel(t)}{E_\parallel \cdot A_\parallel} + \frac{l_\perp \cdot \phi_\perp(t)}{E_\perp \cdot A_\perp} + \frac{l \cdot r_p(t))}{E_p \cdot A_p[1 - \chi_p \cdot r_p(t)]} \right\} + \Delta\varepsilon_{\parallel,in}(t) \cdot l_\parallel + \Delta\varepsilon_{\perp,in}(t) \cdot l_\perp - \Delta\varepsilon_{p,in}(t) \cdot l}{\frac{l_\parallel[1 + \chi_\parallel \cdot \phi_\parallel(t)]}{E_\parallel \cdot A_\parallel} + \frac{l_\perp[1 + \chi_\perp \cdot \phi_\perp(t)]}{E_\perp \cdot A_\perp} + \frac{l}{E_p \cdot A_p[1 - \chi_p \cdot r_p(t)]}} \tag{7.10}$$

By further neglecting the ageing coefficients, the inelastic strains of the tendon and the tendon relaxation lead to the following, simplified, expression which can be used to calculate the losses in tendon force for the specimens in the uncontrolled environment:

$$\Delta P(t) = \frac{P_0 \cdot \left\{ \frac{l_\parallel \cdot \phi_\parallel(t)}{E_\parallel \cdot A_\parallel} + \frac{l_\perp \cdot \phi_\perp(t)}{E_\perp \cdot A_\perp} \right\} + \Delta L_{in,beam}(t) + \Delta L_{in,column}(t)}{\frac{l_\parallel[1 + \phi_\parallel(t)]}{E_\parallel \cdot A_\parallel} + \frac{l_\perp[1 + \phi_\perp(t)]}{E_\perp \cdot A_\perp} + \frac{l}{E_p \cdot A_p}} \tag{7.11}$$

7.8.1 Comparison between model and test results with creep coefficients from block specimens

Controlled conditions

Since the elastic deformations of the beam and the beam-column specimen were measured, it is possible to estimate the Young's modulus for the two specimens. The values are needed, to calculate the loss in post-tensioning force according to Equation (7.9) and (7.11) and were calculated with the measured elastic deformations shown in Figure 7.21 and are summarised in Table 7.9.

Table 7.9: Young's modulus [MPa] parallel and perpendicular to the grain in controlled environment, rounded to 10 MPa.

	$E_\perp$	$E_\parallel$
Beam-Col 100mm	1380	7280
Beam	-	8730

The low value for the beam is due to the large deformations at the edge of the beam, between the beam and the steel plate, which is a part of the anchorage system. The same phenomenon could be observed with the frame specimens, where high deformations occurred in the column due to the low modulus of elasticity perpendicular to the grain, but also at the interfaces between column and beam.

With the elastic properties of the specimens (Table 7.9) and the measured creep coefficients from the block specimens (Figure 7.10), the losses at several time steps can be calculated with Equation (7.9) and compared with the measured values. The result is presented in Figure 7.25(a) for the beam-column specimen and in Figure 7.25(b) for the beam specimen.

(a)   (b)
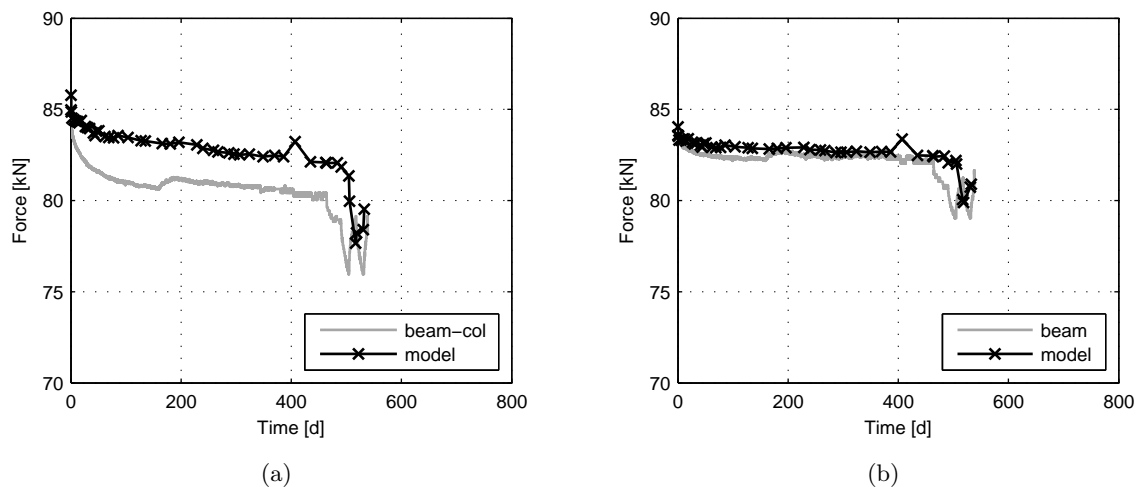
Figure 7.25: Calculated losses in post-tensioning force and measured losses in the controlled environment 7.25(a): Beam-column specimen 7.25(b): Beam specimen

The calculated values for the beam-column specimen are not as precise as the values for the beam specimen. The losses in the beam specimen are predicted very well, considering the sensitivity of the measurements. The losses are slightly under predicted by 1 kN.

However, the losses in the frame (beam-column) specimen are underestimated with the model and the estimated creep coefficients. This could be due to the model itself (no ageing coefficients, no relaxation) or due to the estimated creep coefficients. The loss rate between the model and the measurements is accurate, i.e. the slope of the curve is nearly identical for both specimens, only the initial loss can not be accounted for properly by the model.

Uncontrolled conditions

The elastic properties of the specimens can be estimated with the measured elastic deformations (as shown in Figure 7.21) which occur during the process of applying the tendon force. The values for the Young's modulus are summarised in Table 7.10.

Table 7.10: Young's modulus [MPa] parallel and perpendicular to the grain in the uncontrolled environment, rounded to 10 MPa.

	$E_\perp$	$E_\parallel$
Beam-Col 100mm	1300	7700
Beam-Col 100mm	1270	9020
Beam-Col 160mm	1110	8040
Beam-Col 240mm	1260	6950
Beam	-	5020

The losses in tendon force can be calculated by using Equation (7.11). The creep coefficients were obtained from the block specimens (see Figure 7.11). The inelastic deformations due to shrinkage and swelling were measured with the dummy specimens as indicated in Figure 7.21. The obtained values for the tendon force over time are presented in Figure 7.26. The losses are predicted well up to 400 days, afterwards all losses are over predicted. Moreover, an offset is clearly noticeable after 400 days. This is due to an offset in the demec gauge which lead to a measurement error. The error was 0.03 mm and affected all measuring points for nearly 200 days. The black markers in Figure 7.26(a)-7.26(e) show the measured values including the offset. The grey markers are the corrected values where the offset was removed. The measurements were stopped after 620 days, i.e. when the tests continued with only three specimens.
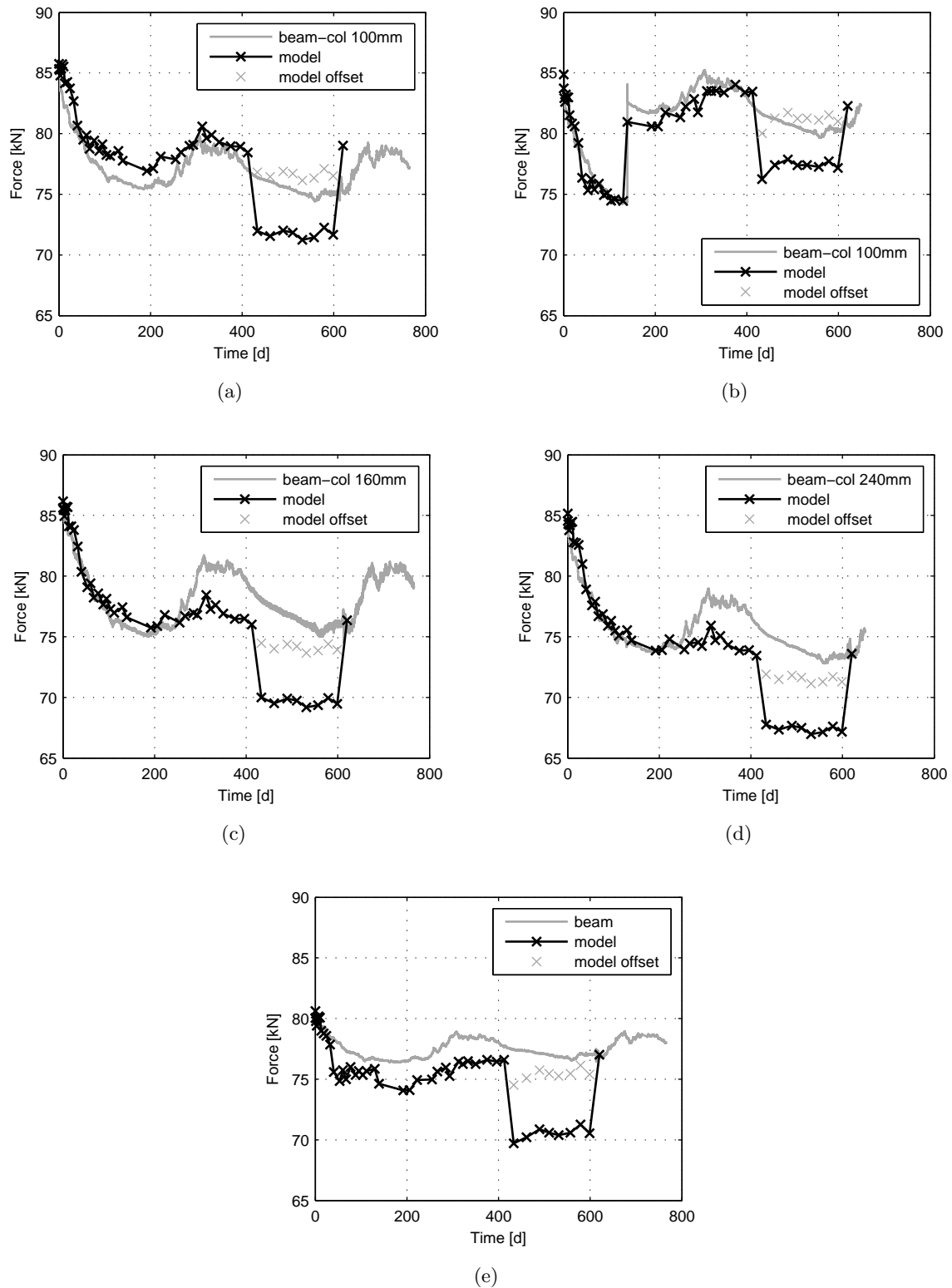
Figure 7.26: Calculated losses in post-tensioning force and measured losses in the uncontrolled environment 7.26(a): Beam-column specimen with column depth of 100 mm 7.26(b): Beam-column specimen with column depth of 100 mm (re-stressed) 7.26(c): Beam-column specimen with column depth of 160 mm 7.26(d): Beam-column specimen with column depth of 240 mm 7.26(e): Beam specimen

Prediction of the losses in tendon force with the analytical model

The model can be used to predict the total amount of losses in tendon force after the service life of a building (50 years). By using the extrapolated creep coefficients from the small block specimens for ash (Table 7.3) and spruce (Table 7.4) the losses for the specimens in the uncontrolled and controlled environment can be calculated. The results are presented in Table 7.11 without the specimen that was re-stressed.

Table 7.11: Model prediction for the losses in tendon force in the uncontrolled and controlled environment

	Total loss in kN	Loss in %
Uncontrolled environment		
Beam-Col 100mm	23	27
Beam-Col 160mm	31	33
Beam-Col 240mm	33	39
Beam	9	11
Controlled environment		
Beam-Col 100mm	9	10
Beam	3	3

The model prediction as well as the extrapolated losses for all beam and beam-column specimens are presented in Table 7.12. The comparison of the results show that the model tends to slightly under predict the losses in the controlled environment. However, too large losses are predicted for the specimens in the uncontrolled environment where the losses for the beam-column specimens are predicted in a range of 27-39% while the extrapolated losses from the tests suggest losses that are about 10% lower.

Table 7.12: Extrapolated losses in % from the beam and beam-column specimens and the corresponding model prediction

Specimen	Loss specimens	Loss model
Uncontrolled environment		
Beam-Col 100mm	20	27
Beam-Col 160mm	15	33
Beam-Col 240mm	25[*)]	39
Beam	6	11
Controlled environment		
Beam-Col 100mm	13	10
Beam	4	3
[*)] extrapolation based on data for one year		

The deviation of the model can be explained with the very high creep coefficients obtained from the small block specimens in the uncontrolled environment. Since the larger beam and beam-

column specimens are less vulnerable to a change in relative humidity, smaller creep coefficients can be expected for the larger specimens.

7.9   Parametric study

To investigate the benefit of the reinforcement with hardwood in the column, the beam-column specimen can be compared with a beam-column specimen with no hardwood (i.e. the column is made of spruce) and a beam-column specimen using steel reinforcement in the column. The latter one could be a beam-column specimen with steel plates and epoxied rods, so that the load is transferred through the column via the rods instead of the timber as recommended by Fragiacomo and Davies [46] as a possible way to reduce the losses. This means that no losses perpendicular to the grain occur. However, this solution is more intrusive compared to a timber-based solution.

The calculations for the case with the column made of ash are based on the properties summarised in Table 4.1.

For the case with the spruce column, a Young's modulus perpendicular to the grain of 580 MPa was assumed. This value is obtained by multiplying the value for a strength grade C24 [62] by a factor 1.56. The factor was obtained by comparing the Young's modulus perpendicular to the grain for ash to the value of the strength grade D40 [62]. The properties of the beam are assumed to be the same as for the case with the column made of ash (Table 7.13).

The geometric properties are the same as for the beam-column specimen with a column depth of 100 mm. All calculations are done by using Equation (7.9), whereas the creep coefficients were obtained from the measurements in the controlled environment (Figure 7.10), while assuming that ash and spruce have the same creep coefficient perpendicular to grain. Although this assumption was not verified by experimental testing, it is regarded as a conservative estimation, since previous experimental testing carried out on glulam made from different softwood species (e.g. radiata pine) showed a lower creep coefficient perpendicular to the grain than that monitored on ash [88]. The results of the parametric study are summarized in Table 7.13.

Table 7.13: Calculated losses of tendon force in % of the initial tendon force

Configuration	1 year	10 years	50 years
Column made of ash	4.2	7.1	10.4
Column made of spruce	6.6	11.6	17.1
Column with steelwork	2.2	3.3	4.5

Reinforcing the column with ash (hardwood) is beneficial. The losses after 50 years can be reduced by 40% compared to the case where also the column is made of spruce. A reinforcement with steel plates would reduce the losses by 76%, however the use of steelwork may prove to be more expensive than the use of ash reinforcement. Therefore, it makes sense to concentrate future efforts on reinforcing the column by using economical solutions.

7.10   Discussion and limitations

The total losses for a post-tensioned timber frame are estimated larger than the losses expected in a post-tensioned concrete structure. In order to predict the losses in tendon force - especially in the uncontrolled conditions - more accurately, the tests presented in this paper will be continued for at least another year. However, even though the tests have only be ongoing for two years, some important conclusions can already be drawn.

For one, the losses depend on the relative humidity in the environment. If the humidity decreases, so does the moisture content in the timber and the tendon force drops. If the humidity increases, a recovery in tendon force can be observed. A drop in the relative humidity to an all time low is critical, since the creep coefficient will increase drastically as could be observed with the block specimens that were subjected to a cyclic relative humidity. Controlling the relative humidity would therefore reduce the total losses in tendon force. If the relative humidity can be kept constant, the losses could be in the range of 15 to 20% (as opposed to 25 to 30% in the uncontrolled environment).

The tests presented herein indicate that 30% of tendon force losses can occur over the service life of a post-tensioned timber structure, which has to be accounted for during the design process. However, the tests showed a size-effect; the small block specimens reacted more sensitive than the post-tensioned specimens, leading to additional losses due to ms-creep. A full-scaled specimen in a building would even be less sensitive to a change in relative humidity, which then again reduces the total losses.

Furthermore, the total losses can also be reduced by re-stressing the system. However, this has to be considered during the design of a building, since re-stressing is only possible with a special anchorage, which needs to be accessible.

The column depth did not have a strong impact on the total amount of losses in post-tensioning force. All the specimens showed a similar amount of loss in post-tensioning force over time.

It was possible to reproduce the measured data from the tendon force reasonably well by using an analytical model. The analytical analysis also showed that reinforcing the column with ash is beneficial in order to reduce the losses in tendon force. Reinforcing the column with a different type of hardwood or an engineered wood product could reduce the losses even further. Although a reinforcement using steel would minimize the losses, a solution using wood is preferred by the authors. Future efforts should concentrate on alternative ways of reinforcing the column.

The specimen positioned outdoors did not suffer from losses in post-tensioning force, since the swelling of the specimen was able to compensate for the losses. Applying the tendon force on very dry specimens could therefore be a way to avoid large tendon force losses.

The results and conclusions presented herein are based on a small number of specimens. More tests on this subject are necessary in order to increase the overall number of specimens and reduce the uncertainties of the results presented herein.

Furthermore the results are valid for two wood species only loaded under compression parallel to the grain (spruce specimens) and perpendicular to the grain (ash specimens). In addition to these limitations, the results are also only valid for the climatic conditions described in this paper.

Chapter 8

Prototype design

The post-tensioned timber frame investigated in the previous chapters was used to build a prototype building, the "ETH House of Natural Resources" (Figure 8.1), a building with a two-storey post-tensioned timber frame situated on the ETH Hönggerberg campus [89]. The design is performed according to the Swiss SIA standards [60], [82], [90].

Figure 8.1: "ETH House of Natural Resources" (Picture: ETH Zurich / Marco Carocari)

The building comprises four innovative structural systems, a post-tensioned timber frame, two composite beech LVL concrete floors and a biaxial timber slab made of cross laminated timber and beech LVL. The building serves as an office building for the laboratory of hydraulics, hydrology and glaciology of ETH Zurich. Furthermore it serves as a "living lab" for the implementation of a permanent sensor network for long-term monitoring of the structure and as a setup for a field testing campaign of in-situ tests at different construction stages [73].

The design chapter focuses on the timber frame, whereas the other structural as well as all non-structural elements are not discussed herein.

8.1   Structure

8.1.1   Post-tensioned timber frame

The frame has a height of 6 m (two 3 m stories) and three bays with a span of 6.5 m in both directions. The beams have a cross section of 720×280 mm and are made of glulam GL24h. The hardwood columns have a cross section of 380×380 mm and are made of ash with the strength grade D40.

A tendon force of 500 kN was chosen to achieve the building design objectives. This force has to be guaranteed over the lifetime of a building: thus, the initial tendon force was set to 700 kN, i.e. nearly 30% tendon force losses are taken into account based on the findings in Chapter 7.

The columns were modelled with pinned connections at the bottom to simplify the boundary conditions. The actual column support conditions are semi-rigid in order to facilitate the transfer of both gravity and horizontal loads.

Figure 8.2: Post-tensioned timber frame in the "ETH House of Natural Resources"

8.1.2   Composite slabs

The slabs on the first storey are timber-concrete composite slabs, using beech LVL plates (laminated veneer lumber) as reinforcement [72]. The LVL-plates are notched to transfer the shear forces between the concrete and the LVL plates as shown in Figure 8.3(a). The height of the slab is only 200 mm, whereas the LVL plates are 40 mm thick. The LVL-plates are positioned onto the frame before the concrete is poured onto the LVL-plates.

The slabs on the roof are made of timber-concrete composite hollow core elements using beech LVL. The design of these slabs is more conventional; a 70 mm prefabricated concrete slab is screwed to beech LVL beams with a cross section of 240×80 mm. Under the beams 40 mm thick LVL plates are connected to the beams, acting as tension reinforcement. The system is shown in Figure 8.3(b). The elements are pre-fabricated and directly transported to the building site. The slabs are not designed within this thesis, only their weight and load distribution to the frames are taken into account.

(a)   (b)
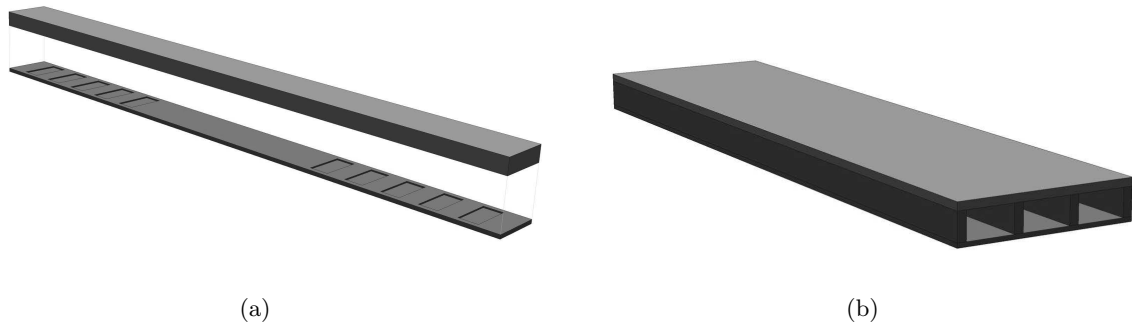
Figure 8.3: Slabs used in the building 8.3(a): Composite timber slab made of beech LVL plates, the notches in the plates transfer the shear between the LVL-plates and the concrete 8.3(b): Prefabricated timber-concrete composite hollow core elements using beech LVL

The load transfer from the composite slabs to the post-tensioned timber frames was alternated from one field to another as shown in Figure 8.4. This guarantees, that the frames are loaded uniformly. If all the slabs would transfer the load in the same direction, only the frames perpendicular to that direction would be loaded while the frames in the other direction would remain unloaded.
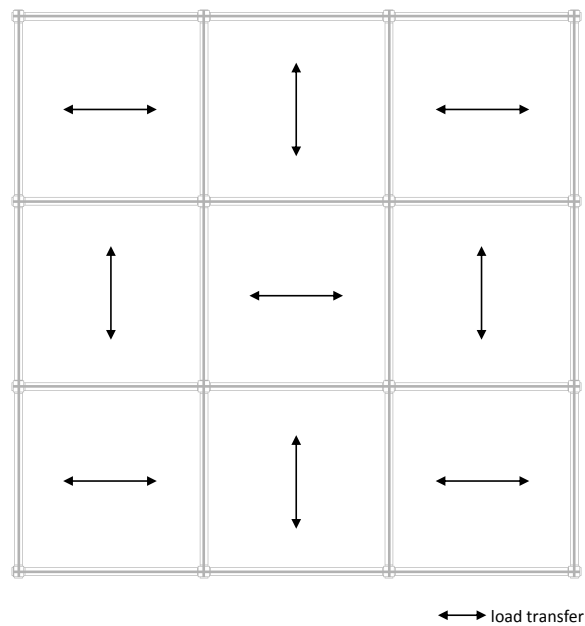
Figure 8.4: Load transfer from slabs to the post-tensioned timber frames

8.2   Loads

The gravity loads are summarised in Table 8.1. The weight of the frame itself is not listed in the gravity loads but is taken into account in the calculations.

The dead load of the 1st storey includes the weight of the slabs as well as the weight of the underlay and the floor covering. In addition to the dead load, 0.5 kN/m² were added to cover non-structural elements such as office partition walls. The dead load of the 2nd storey includes the weight of the slabs as well as the weight of the entire roof structure.

The live loads are given by the standards for an office building (1st storey) and for a non-accessible roof (2nd storey). The snow load was calculated according to the building's location in Zurich.

Table 8.1: Gravity loads acting on the post-tensioned timber frame

		1st storey	2nd storey
Dead load slabs	g_k	6.4 kN/m²	4.7 kN/m²
Live load	q_k	3 kN/m²	0.4 kN/m²
Snow load	$q_{k,s}$	-	1.3 kN/m²

The horizontal loads are summarised in Table 8.2. The global wind force was calculated for the given geometry and location of the building. The ground acceleration is chosen according to the 2003 Swiss standards for a site in Zurich.

Table 8.2: Horizontal load cases

Wind force	$q_{k,w}$	1.05 kN/m²
Ground acceleration	a_{gd}	0.6 m/s²

8.3   Design for gravity loads

8.3.1   Load application on the frame

The alternating direction of load transfer from the slabs leads to the situation, where the inner frames are fully loaded, whereas some outer frames are only partially loaded as shown in Figure 8.5.

The design will be governed by the inner frames where all beams are fully loaded. The calculations are therefore performed for the inner frames only.

The uniformly distributed load of the slabs for the first storey on the design level is:

$$q_{Ed,1} = \gamma_G \cdot g_k + \gamma_Q \cdot q_k = 1.35 \cdot 6.4 + 1.5 \cdot 3 = 13.1 \text{ kN/m}^2 \tag{8.1}$$

Resulting in the following uniformly distributed load on the frames:
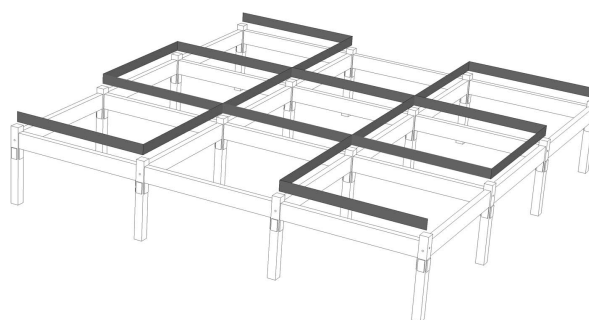
Figure 8.5: Uniformly loaded beams due to alternating directions of the slabs

$$q'_{Ed,1} = 6.5/2 \cdot 13.1 = 42.7 \text{ kN/m} \tag{8.2}$$

The uniformly distributed load on the roof slabs (second storey) is:

$$q_{Ed,2} = \gamma_G \cdot g_k + \gamma_Q \cdot q_k = 1.35 \cdot 4.7 + 1.5 \cdot 1.3 = 8.3 \text{ kN/m}^2 \tag{8.3}$$

$$q'_{Ed,2} = 6.5/2 \cdot 8.3 = 27.0 \text{ kN/m} \tag{8.4}$$

8.3.2 Design with a simple hand calculation

The design of a post-tensioned timber connection can be performed with a simple calculation procedure presented in this section. Assuming a system with a single supported beam with two rotational springs as shown in Figure 8.6(a), the moments and shear forces (Figure 8.6(b)) in the beam can be calculated.

(a)   (b)
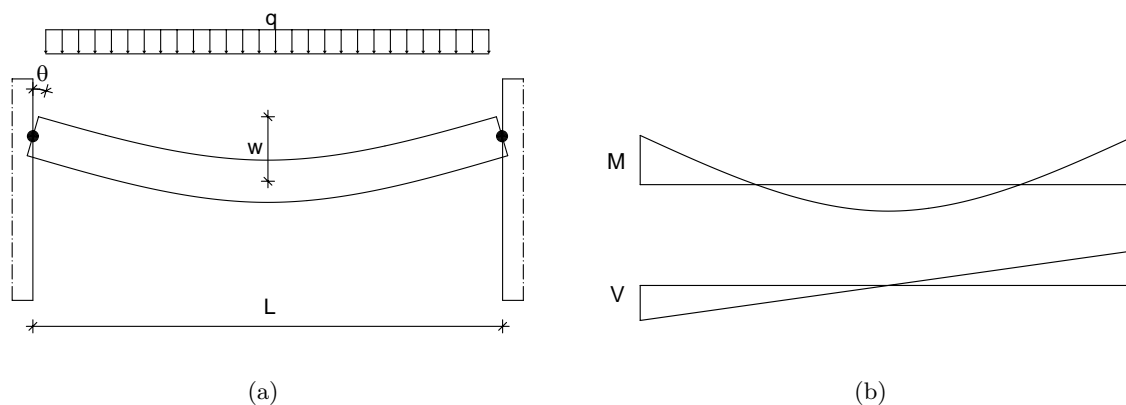
Figure 8.6: 8.6(a): Analytical system for hand calculation with rotational springs 8.6(b): Moments and shear forces in the beam

The two Equations (8.5) and (8.6) can be used to calculate the moment at the beam-column interface and the moment in mid-span of the beam. The equations can be derived easily using the force method, putting a redundant moment on either side of the beam.

$$M^- = \frac{2 \cdot E \cdot I}{L} \cdot \theta - \frac{q \cdot L^2}{12} \tag{8.5}$$

$$M^+ = \frac{2 \cdot E \cdot I}{L} \cdot \theta + \frac{q \cdot L^2}{24} \tag{8.6}$$

The maximal shear force is:

$$V = \frac{q \cdot L}{2} \tag{8.7}$$

The deflection in the middle of the beam can be calculated according to Equation (8.8), which can be derived with the principle of virtual work.

$$w = \frac{q \cdot L^4}{384 \cdot E \cdot I} + \frac{q \cdot L^2}{8 \cdot G \cdot A} + \frac{L}{4} \cdot \theta \tag{8.8}$$

The model presented in Chapter 3 allows the calculation of the negative moment at the beam-column interface. It is recommended to use a spreadsheet which calculates the moment at the interface, maximal stresses, neutral axis depth and the moment in mid-span of the beam based on a given rotation. All design parameters are summarised in Table 8.3.

Table 8.3: Design under gravity loads using the spring model

Parameter		1st storey	2nd storey	Design limit
Load	q	42.7 kN/m	27.0 kN/m	62.0 kN/m
Stresses at interface	σ_{inf}	6.5 MPa	4.9 MPa	8.6 MPa
Neutral axis depth	x	551 mm	720 mm	416 mm
Moment at interface	M^-	88.1 kNm	57.4 kNm	110.1 kNm
Moment mid-span	M^+	134.7 kNm	79.6 kNm	387.1 kNm
Shear force	V	134.7 kN	87.6 kN	195.8 kN
Deflections	w	6.8 mm	4.4 mm	13 mm

The design limits were all calculated according to SIA 265 [60]. The controlling design criterion is the stress at the interface perpendicular to the grain. The design limit of 8.6 MPa includes a stress distribution factor. However, the value of 8.6 MPa is much smaller than the values that were obtained during the test series on the connection (Chapter 4). Therefore, a design limit of 8.6 MPa is considered to be very conservative.

8.3.3 Design using OpenSees

The design can also be performed using a simple software like OpenSees [91]. A two storey, three bay frame is modelled according to the geometry of the building and loaded under gravity loads as shown in Figure 8.7.
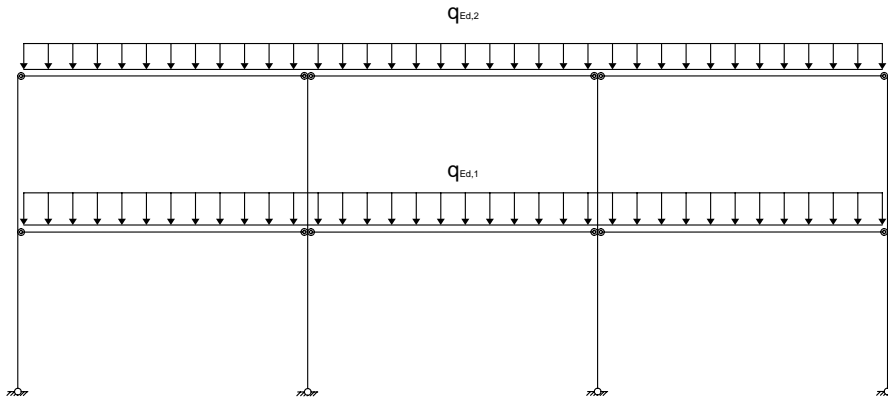
Figure 8.7: OpenSees model of the two storey building using rotational springs to simulate the post-tensioned connections

The following elements were used for the model:

- Columns: Elastic BeamColumn element

- Beams: Elastic BeamColumn element

- Joint: Rotational spring as zero length element

The springs are tri-linear springs which are implemented in OpenSees. The parameters for the springs can be calculated with the analytical model presented in Chapter 3. Figure 8.8 shows a comparison between the the results from the model and a tri-linear spring used for the OpenSees model. The zero length OpenSees spring matches the initial stiffness as well as the secondary stiffness. However, it overestimates the stiffness between 100 to 120 kNm due to the tri-linear characteristics of the spring. Moreover, the yielding point of the spring was set at 230 kNm. The reason for the premature yielding is a safety consideration, since the tendon would behave brittle and not yield.

The moments due to gravity loads from the OpenSees model are shown in Figure 8.9. The values are close to the ones from the simple hand calculation. A summary of the moments derived from the simple hand calculation as well as from the OpenSees model is given in Table 8.4. Since the calculations were performed for an inner beam, the values are compared to those of the inner beam as well as the outer beam (values in brackets in Table 8.4). The differences are small for the connection moments and become larger for the positive field moments in the outer beams.
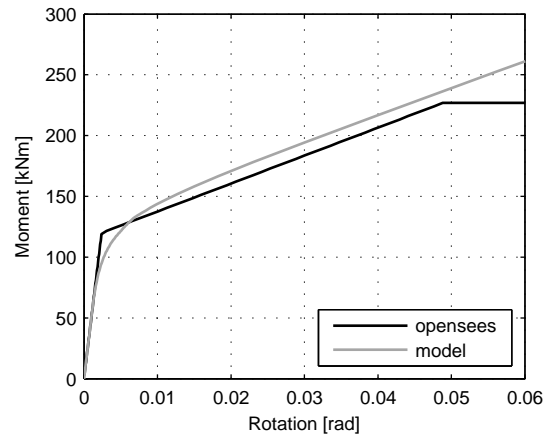
Figure 8.8: Spring properties according to the analytical model and tri-linear spring properties used for the OpenSees model
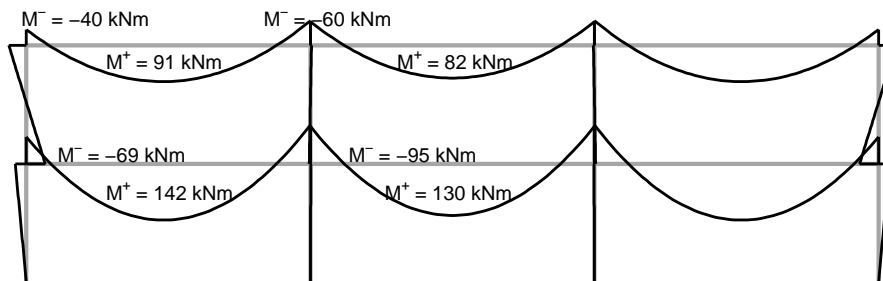
Figure 8.9: Moments due to gravity loads modelled with OpenSees

Table 8.4: Comparison between the moments due to gravity according to the hand calculation and according to the OpenSees model

Parameter	Hand calculation	OpenSees	Difference
$M^-_{1^{st} storey}$	88.1 kNm	95 kNm	+8%
$M^+_{1^{st} storey}$	134.7 kNm	130 (142) kNm	-4% (+5%)
$M^-_{2^{nd} storey}$	57.4 kNm	60 kNm	+5%
$M^+_{2^{nd} storey}$	79.6 kNm	82 (91) kNm	+3% (+14%)

8.4 Seismic design

8.4.1 Response spectra and performance goals

Three uniform hazard spectra [92] with a return period of 73, 475 and 2475 years will be used
for a performance based design [93]. The fourth spectrum was obtained from the Swiss SIA
standards [90] for a soil class C ("Deposits of naturally consolidated and uncemented gravel and
sand and/or moraine with a thickness exceeding 30 m") and a damping value of 5% and has
been added as a reference spectrum. The spectra are shown in Figures 8.10(a) and 8.10(b),
respectively. The latter spectra will also be used for the design. The design spectrum coincides
with the UHS spectra with a return period of 2475 years (i.e. the maximal credible earthquake)
for spectral displacements larger than 0.015 m.
No ductility will be accounted for, even though the SIA allows considering a ductility of q = 1.5
for any kind of timber structure [60]. However, since no steel elements such as dowels are used
for the connection and a damping ratio ζ of 5% is assumed for simplicity reasons, no ductility
shall be accounted for (i.e. q = R_μ = 1.0).
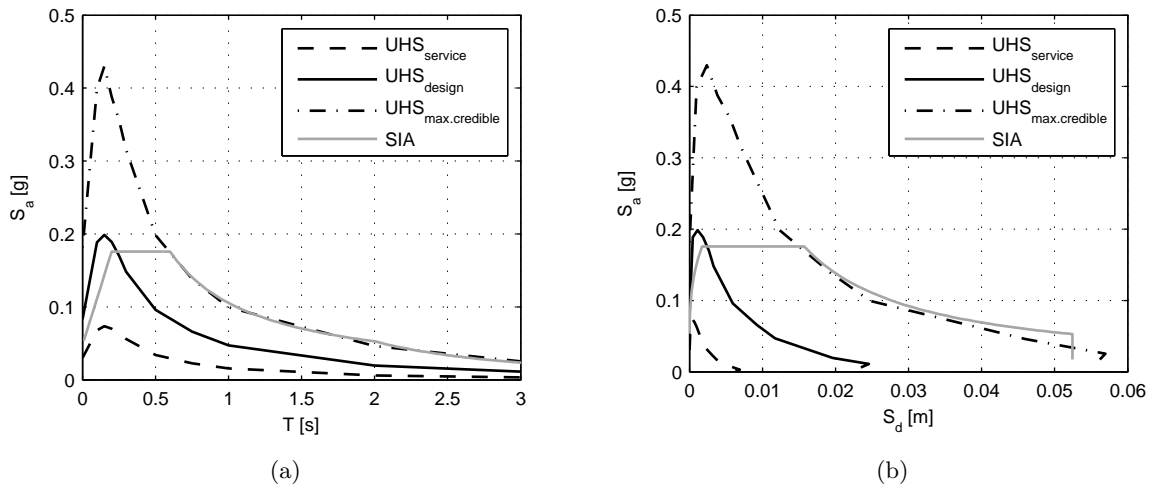
Figure 8.10: 8.10(a): Elastic acceleration spectra for Zurich 8.10(b): Elastic capacity spectra for Zurich

The performance goals are summarised in Table 8.5. During a serviceability earthquake no
damage should occur to the structure, so that the building can be used without any major
repair work. During a design earthquake, a limited damage in structural system may be taken
into account. The maximum credible earthquake should not result in a collapse of the structure,
however, irreparable damages may occur.

8.4.2 OpenSees model

The same model as shown in Figure 8.7 will be used for the seismic design. However, the gravity
loads differ since the characteristic values for the dead loads can be used and only a part of the
live loads have to be accounted for:

Table 8.5: Performance goals and hazard levels for the performance based design approach

Hazard level	Performance level	Return period	Exceedance
UHS service	Operational	73 years	10% in 50 years
UHS design	Limited damage	475 years	5% in 50 years
UHS maximum credible	Collapse prevention	2475 years	2% in 50 years

$$q_{Ed,1} = g_k + \psi_2 \cdot q_k = 6.4 + 0.3 \cdot 3 = 7.3 \text{ kN/m}^2 \tag{8.9}$$

$$q'_{Ed,1} = 6.5/2 \cdot 7.3 = 23.7 \text{ kN/m} \tag{8.10}$$

The values for the roof are smaller:

$$q_{Ed,1} = g_k + \psi_2 \cdot q_k = 4.7 + 0 \cdot 1.3 = 4.7 \text{ kN/m}^2 \tag{8.11}$$

$$q'_{Ed,1} = 6.5/2 \cdot 4.7 = 15.3 \text{ kN/m} \tag{8.12}$$

The moments due to gravity loads have to be calculated with the spring properties according to Figure 8.8 since no shear deformations occur in the panel region. The moments due to the reduced gravity loads are plotted in Figure 8.11.
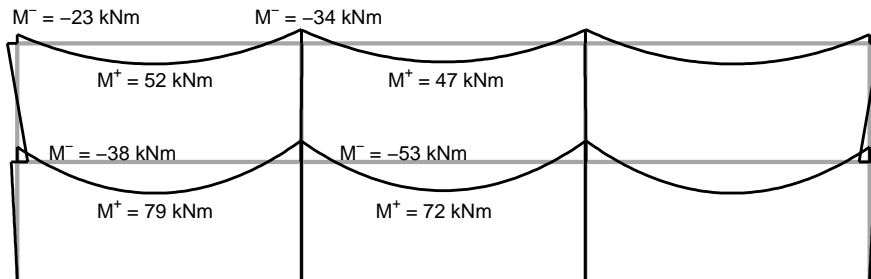
Figure 8.11: Moments due to reduced gravity loads modelled with OpenSees

The pushover-curve is generated with modified spring characteristics, since the shear deformations in the beam-column interface have to be accounted for. The springs are altered in

order to account for the additional deformation (see Figure 8.12(a)). The springs for the inner
columns are stiffer compared to the springs for the outer columns which soften with increasing
moment. The spring properties were calculated according to the model presented in Chapter 3
and verified with the pushover tests described in Chapter 5. These springs were used to gener-
ate the pushover-curve showed in Figure 8.12(b) which is plotted together with the analytical
pushover-curve and the curve obtained from the experimental campaign.

(a)   (b)
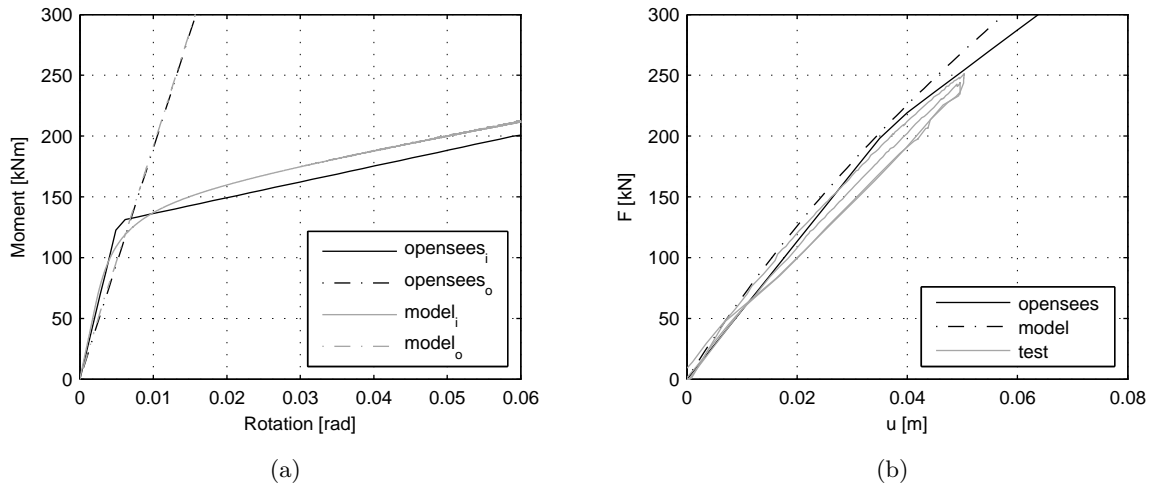
Figure 8.12: 8.12(a): Spring properties for the OpenSees as well as analytical model of the two storey
building (indices i: inner column, o: outer column) 8.12(b): Pushover-curves from OpenSees, analytical
model and test results for a tendon force of 500 kN

The gravity load is added on the columns so that they do not generate any moments in the
springs but can be accounted for the P-Δ effect.
A modal analysis [74] was performed in order to obtain the first period of the system which can
then be compared to the first mode from the OpenSees model (see Table 8.6). The mass acting
on the first storey is:

$$m_1 = 462.15 \text{ kN} \tag{8.13}$$

The mass on the roof structure is smaller:

$$m_2 = 298.35 \text{ kN} \tag{8.14}$$

The masses lead to a mass matrix of:

$$M = \begin{bmatrix} m_1 & 0 \\ 0 & m_2 \end{bmatrix} \tag{8.15}$$

The stiffness influence coefficients have to be calculated for both storeys. The equations can be found in the literature [74]. The lateral stiffness for one storey is defined as:

$$k = \sum_{columns} \frac{12 \cdot E_c \cdot I_c}{h_c^3} \cdot \frac{12 \cdot \rho + 1}{12 \cdot \rho + 4} \tag{8.16}$$

The parameter ρ is called the beam-to-column stiffness ratio and is defined as:

$$\rho = \frac{\sum_{beams} E \cdot I/L}{\sum_{columns} E_c \cdot I_c/h_c} \tag{8.17}$$

Inserting the material and geometric properties of the structure into Equations (8.17) and (8.16) leads to the value:

$$k_1 = k_2 = 8646 \text{ kN/m} \tag{8.18}$$

And the stiffness matrix can then be written with the stiffness influence coefficients for the frame with two storeys:

$$K = \begin{bmatrix} k_1 + k_2 & -k_2 \\ -k_2 & k_2 \end{bmatrix} \tag{8.19}$$

Solving the following equation for the eigenvalue problem:

$$[K - \omega^2 \cdot M] \cdot \phi = 0 \tag{8.20}$$

leads to the first eigenvector:

$$\phi_1 = \begin{bmatrix} 0.7 \\ 1.0 \end{bmatrix} \tag{8.21}$$

and the first period:

$$\omega_1 = 8.79 s^{-1} \rightarrow T_1 = \frac{2\pi}{8.79} = 0.71 \text{ s} \tag{8.22}$$

This value is smaller than the value obtained directly from the OpenSees model (0.83 sec as shown in Table 8.6), which means that the analytical solution is a bit stiffer than the OpenSees model.

The pushover-curve for the two-storey frame was generated with a load application that corresponds to the shape of the first eigenvector (see Equation (8.21)), i.e. the horizontal load acting

Table 8.6: First period and first eigenfrequency for the two storey timber frame

Calculation	Period T_1	Frequency f_1
Analytical model	0.71 s	1.4 Hz
OpenSees	0.83 s	1.2 Hz

on the top storey corresponds to 1.0 whereas the one on the first storey is scaled to 0.7, as shown in Figure 8.13.
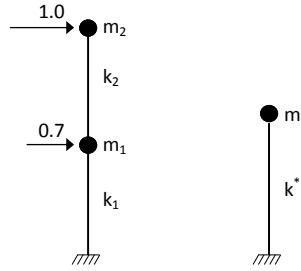
Figure 8.13: Actual 2DOF-system and the equivalent SDOF-system

The two storey frame has to be converted into an equivalent system with a single degree of freedom. Several parameters have to be calculated in order to transform the 2DOF-system into an equivalent SDOF-system (effective modal SDOF sytem) [74], [94], [95].
The modal participation factor is calculated as follows:

$$\Gamma_1 = \frac{\phi_1^T \cdot M \cdot e}{\phi_1^T \cdot M \cdot \phi_1} = 1.18 \tag{8.23}$$

where e is the a uniform vector [1 1]. The effective modal mass is calculated with:

$$m^* = \sum_i (m_i \cdot \phi_{1,i}) = 621.86 \text{ kN} \tag{8.24}$$

The mass participation factor:

$$\alpha_1 = \frac{\Gamma_1 \cdot m^*}{\sum_i m_i} = 0.97 \tag{8.25}$$

The pushover-curve for the 2DOF-system is then re-calculated for the equivalent SDOF-system (indicated with *). The strength coefficient C^* is defined as the ratio of the base shear V_{base} normalised with the reactive weight W divided by the mass participation factor α_1:

$$C^* = \frac{C}{\alpha_1} = \frac{V_{base}/W}{\alpha_1} \tag{8.26}$$

The roof displacement Δ has to be divided by the modal participation factor Γ_1:

$$\Delta^* = \frac{\Delta}{\Gamma_1} \tag{8.27}$$

The design spectra is shown in Figure 8.14.
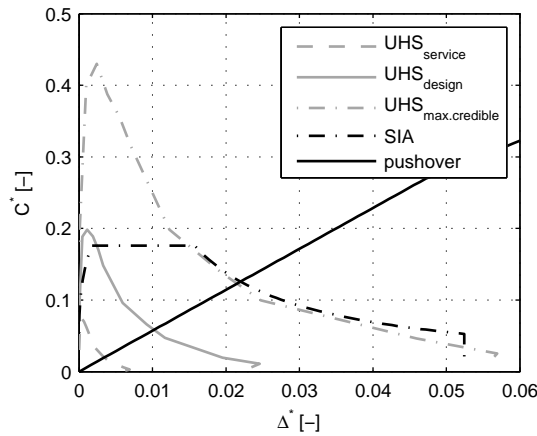
Figure 8.14: Capacity spectrum for the design of the two storey frame

The maximal credible earthquake leads to the necessary values of C^* of 0.122 and Δ^* of 0.021. A back substitution leads to a roof displacement of:

$$\Delta = \Delta^* \cdot \Gamma_1 = 0.021 \cdot 1.18 = 0.025 \text{ m} \tag{8.28}$$

And a base shear of:

$$V_{base} = C^* \cdot \alpha_1 \cdot W = 0.122 \cdot 0.97 \cdot 746.05 = 88.3 \text{ kN} \tag{8.29}$$

This displacement (or base shear) results in additional moments in the frame system as shown in Figure 8.15. These moments have to be added to the ones due to the reduced gravity loads (Figure 8.11) in order to get the total moments in a seismic event.

The maximum combined moment in a connection is 95 kNm (53 kNm due to gravity loads and 42 kNm due to the horizontal force). This moment is the same as for the design under gravity loads (see Figure 8.9). Therefore, the frame response remains in the elastic range during a design-level earthquake. Note, that this earthquake is also the maximum credible earthquake as shown in Figure 8.14.
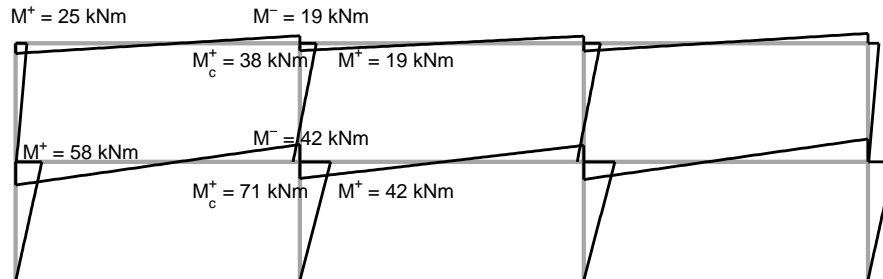
Figure 8.15: Moments due to pushover analysis (without gravity loads)

8.5 Wind loads

The wind loads need to be considered as well, especially concerning the serviceability limit state since the proposed post-tensioned timber frame is a soft system with a first eigenfrequency of 1.2 Hz. Since the wind loads are smaller than the seismic loads, only the serviceability will be checked herein.

The wind pressure for a building in Zurich with the corresponding shape and height amounts to 1.05 kN/m^2 according to SIA 261 [90]. It is assumed, that the façade is fixed at the top and bottom of each storey leading, to the following wind forces for the top and bottom storey (for a total building height of 7 m including 1 m for the roof structure):

$$Q_{w,2} = 6.5 \cdot 3.5/2 \cdot 1.05 = 11.9 \text{ kN} \tag{8.30}$$

$$Q_{w,1} = 6.5 \cdot 3.5 \cdot 1.05 = 23.9 \text{ kN} \tag{8.31}$$

The gravity loads on the structure according to SIA 261 are:

$$q_{Ed,1} = g_k + \psi_0 \cdot q_k = 6.4 + 0.7 \cdot 3 = 8.5 \text{ kN/m}^2 \tag{8.32}$$

$$q_{Ed,2} = g_k + \psi_0 \cdot q_k = 4.7 + 0 \cdot 3 = 4.7 \text{ kN/m}^2 \tag{8.33}$$

These have to be accounted for due to the P-Δ effect on the structure.

These loads and wind forces induce a roof displacement of 9 mm. This corresponds to 1/666 part of its height which is smaller than the recommended limit value for a brittle façade:
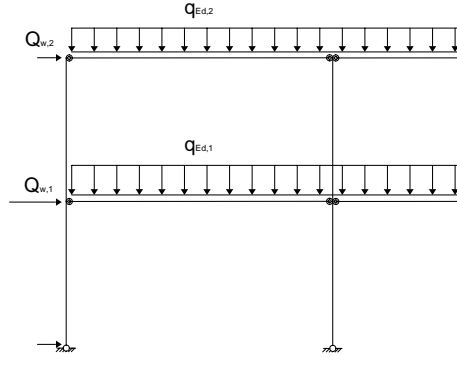
Figure 8.16: OpenSees model of the two storey building with Wind forces acting on the frame

$$\Delta_w = 9 \text{ mm} = \frac{H}{666} \leq \frac{H}{500} \tag{8.34}$$

However, the displacement of the first storey is already 6 mm and therefore:

$$\Delta_w = 6 \text{ mm} = \frac{H/2}{500} \leq \frac{H/2}{500} \tag{8.35}$$

The limit can vary depending on the installations (brittle, ductile) and are regulated in the SIA 260 [82]. If non-brittle elements are installed a limit of H/200 is recommended.

8.6 Time history analyses

Time history analyses were conducted with the OpenSees-model in order to check the seismic performance of the post-tensioned timber frame. The damping of the system has to be considered for the time history analyses whereas Rayleigh damping was chosen. The damping coefficients were calculated based the first two modes of the system with a damping ratio ζ of 5% [74]:

$$a_0 = \frac{2 \cdot \zeta \cdot \omega_1 \cdot \omega_2}{\omega_1 + \omega_2} = \frac{2 \cdot 0.05 \cdot \frac{2 \cdot \pi}{0.831} \cdot \frac{2 \cdot \pi}{0.181}}{\frac{2 \cdot \pi}{0.831} + \frac{2 \cdot \pi}{0.181}} = 0.621 \tag{8.36}$$

$$a_1 = \frac{2 \cdot \zeta}{\omega_1 + \omega_2} = \frac{2 \cdot 0.05}{\frac{2 \cdot \pi}{0.831} + \frac{2 \cdot \pi}{0.181}} = 0.002 \tag{8.37}$$

The coefficients a_1 was assigned to the elements of the model (i.e. to the columns and beams) and the coefficient a_0 to the nodes with the masses [96].

The following earthquakes were chosen for the analysis [97], [98]:

- East-west component of the Umbria earthquake (2nd shock) recorded at the station "Gubbio Piana" on the 26th of September 1997 with a magnitude $M_W = 6.0$

- East-west component of the Patti Gulf earthquake recorded at the station "Patti" on the 15th of April 1978 with a magnitude $M_W = 5.5$

- East-west component of the Aquila earthquake (main shock) recorded at the station "Centro Valle" on the 6th of July 2009 with a magnitude $M_W = 6.3$

The Umbria earthquake has similar characteristics as the design earthquake for the periods of the structure and will therefore lead to a similar displacement (see Figure 8.17). The Patti earthquake is stronger and will lead to greater displacements as were accounted for during the design process. The Aquila earthquake represents a very strong ground motion which can most likely not be handled by the structure.

(a)   (b)
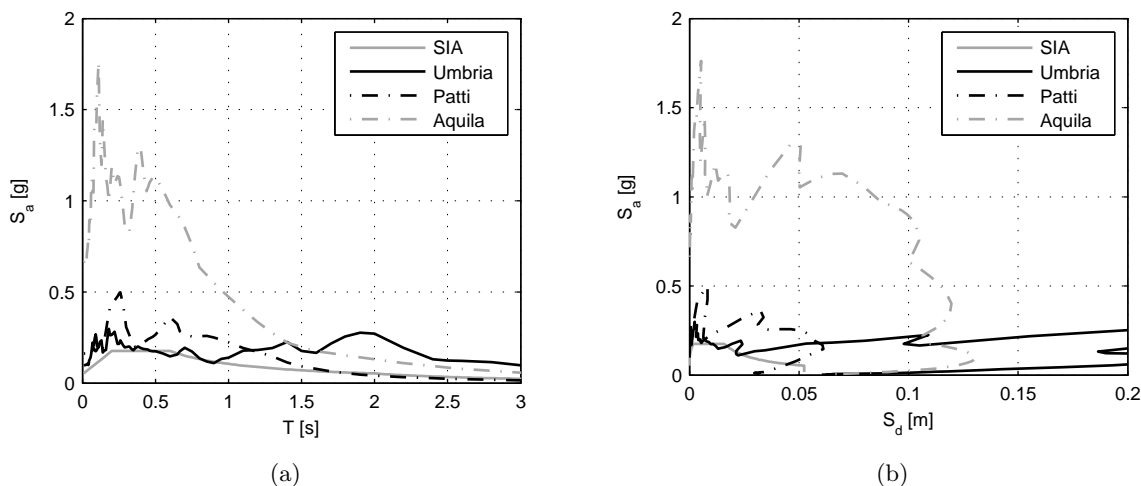
Figure 8.17: 8.17(a): Acceleration spectra for the chosen earthquakes 8.17(b): Capacity spectra for the chosen earthquakes

8.6.1 Umbria earthquake

The Umbria earthquake is the earthquake with the smallest accelerations (Figure 8.18(a)). The horizontal displacement due to the Umbria earthquake is shown in Figure 8.18(b) with the recorded displacement of the frame measured at one of the top nodes. The maximum roof displacement of the frame is approximately 0.023 m, which is slightly smaller than the displacement due to the design earthquake (0.025 m according to Equation (8.28)).

The force-displacement diagram is shown in Figure 8.19(a). The frame behaves as predicted with the pushover analysis, which is indicated with the grey line in Figure 8.19(a). The pushover-curve changes from the initial stiffness to a secondary stiffness at a force of 200 kN. The change in stiffness is due to the gap opening in the outer columns. The Umbria earthquake leads to too small deformations for the gap to open as can be seen in Figure 8.19(b), which shows the
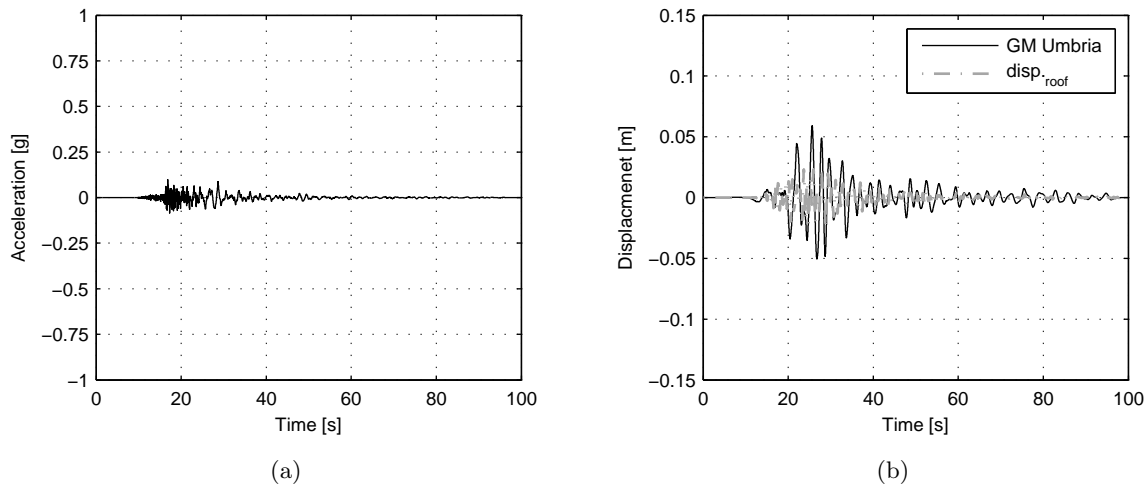
Figure 8.18: 8.18(a): Measured acceleration during the Umbria earthquake 8.18(b): Roof displacement of the structure and displacement of the ground motion

moments due to the Umbria earthquake. The moments are approximately 10% smaller than the ones due to the design earthquake (see Figure 8.15). The moments in the first storey are controlling for the design (53 kNm for the connection at the outer columns and 38 kNm for the connection at the inner columns).
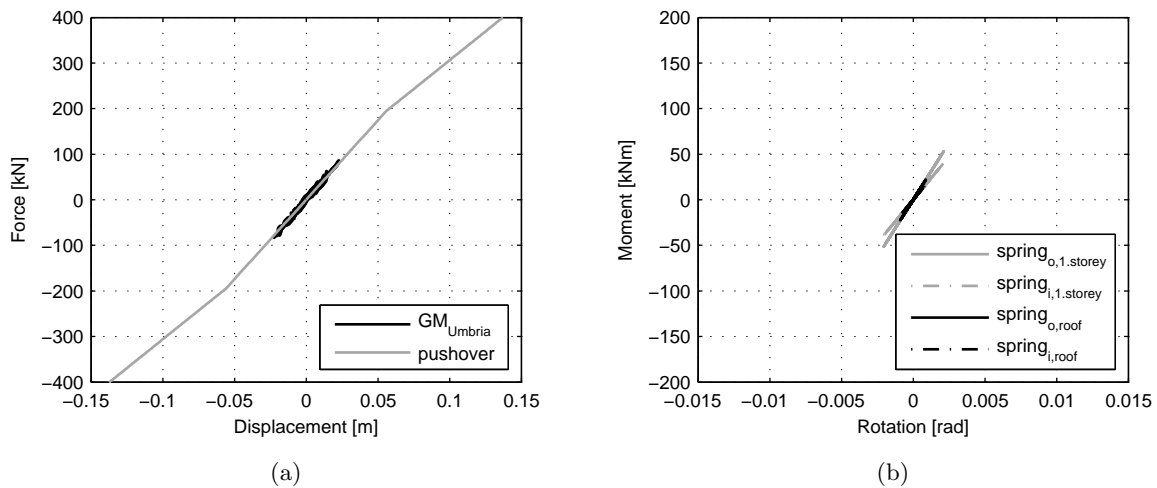
Figure 8.19: 8.19(a): Force-displacement plot resulting from the Umbria earthquake and pushover-prediction 8.19(b): Moments in the beam-column connections during the Umbria earthquake

8.6.2 Patti earthquake

Larger accelerations were measured during the Patti earthquake compared to the Umbria earthquake (Figure 8.20(a)). The horizontal displacement due to the Patti earthquake is shown in Figure 8.20(b) with the recorded displacement of the frame measured at one of the top nodes.

Figure 8.20: 8.20(a): Measured acceleration during the Patti earthquake 8.20(b): Roof displacement of the structure and displacement of the ground motion

Figure 8.21: 8.21(a): Force-displacement plot resulting from the Patti earthquake and pushover-prediction 8.21(b): Moments in the beam-column connections during the Patti earthquake

The maximum roof displacement of the frame is approximately 0.05 m, which is twice as large as the displacement based on the design earthquake (0.025 m according to Equation (8.28)). The force-displacement diagram is shown in Figure 8.21(a). The frame behaves as predicted with the pushover analysis, as indicated with the grey line in Figure 8.21(a). The pushover-curve changes from the initial stiffness to a secondary stiffness at a force of 200 kN. The change

in stiffness is due to the gap opening in the outer columns. The Patti earthquake leads to deformations that do not force the gap to open as shown in Figure 8.21(b).

8.6.3   Aquila earthquake

Large accelerations were measured during the Aquila earthquake (Figure 8.22(a)). The horizontal displacement due to the Aquila earthquake is shown in Figure 8.22(b) with the recorded displacement of the frame measured at one of the top nodes. The maximum roof displacement of the frame approximately 0.13 m, which is over five times larger than the displacement based on the design earthquake (0.025 m according to Equation (8.28)).

(a)   (b)

Figure 8.22: 8.22(a): Measured acceleration during the Aquila earthquake 8.22(b): Roof displacement of the structure and displacement of the ground motion

(a)   (b)

Figure 8.23: 8.23(a): Force-displacement plot resulting from the Aquila earthquake and pushover-prediction 8.23(b): Moments in the beam-column connections during the Aquila earthquake
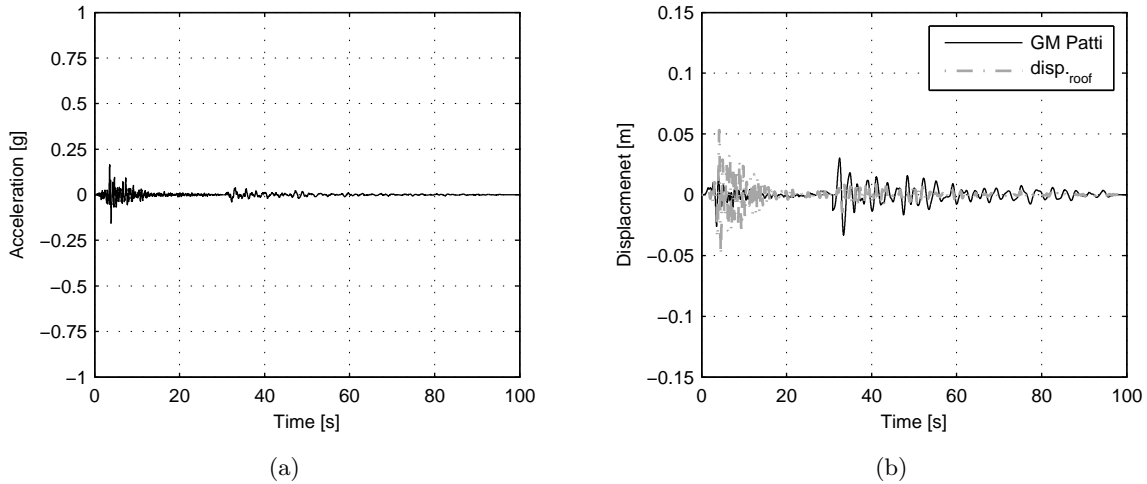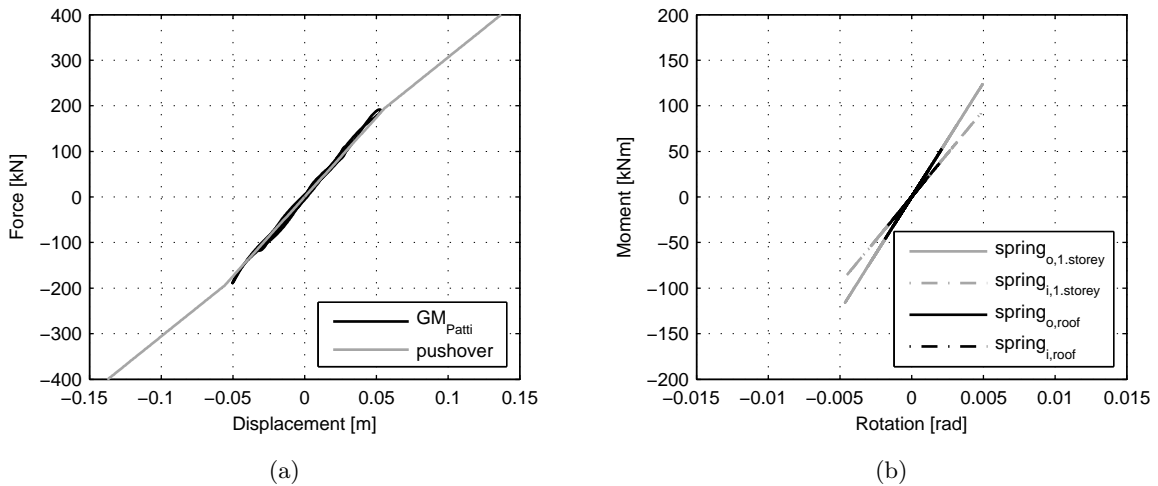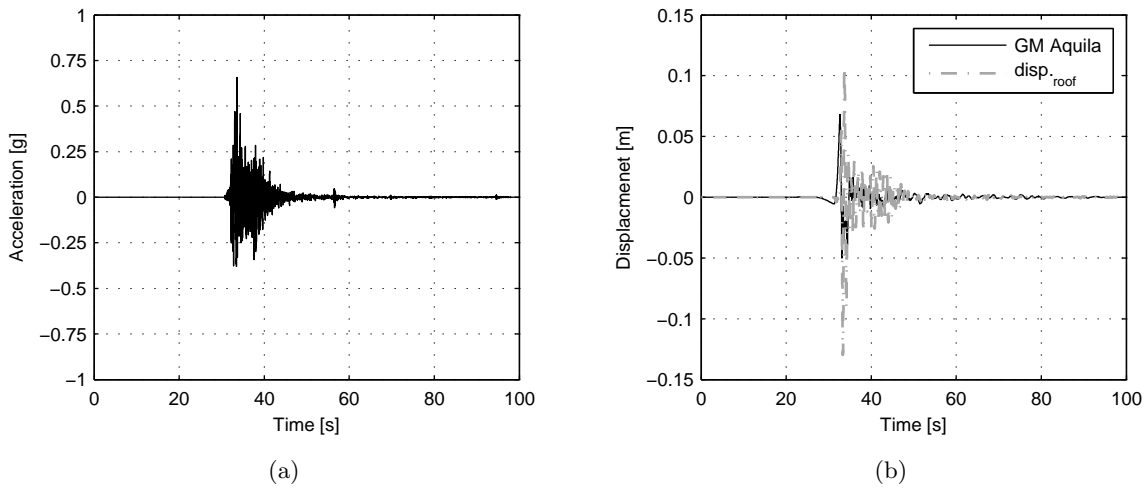
The force-displacement diagram is shown in Figure 8.23(a). The frame behaves as predicted with the pushover analysis, which is indicated with the grey line in Figure 8.23(a). The pushover-curve changes from the initial stiffness t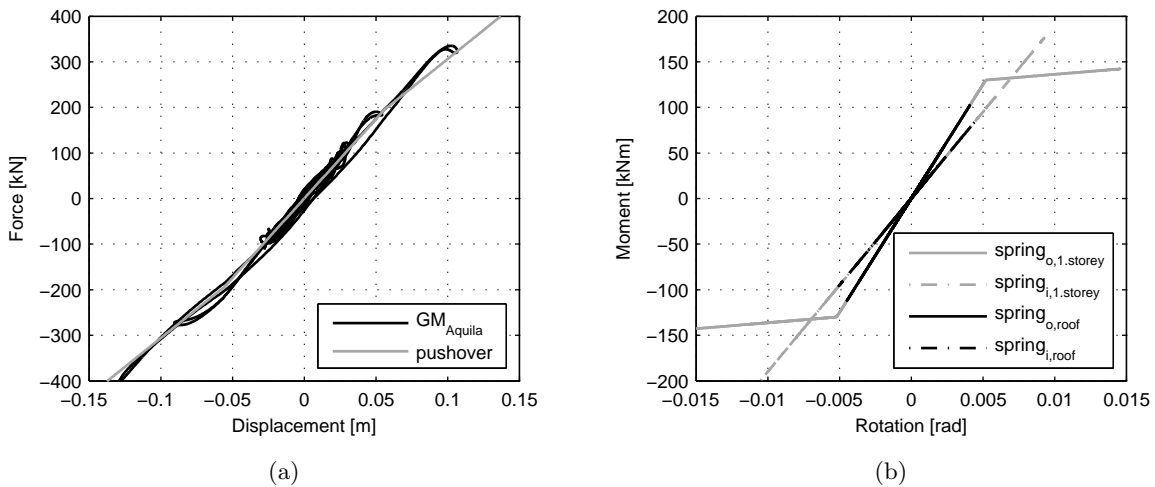o a secondary stiffness at a force of 200 kN. The change in stiffness is due to the gap opening in the outer columns, i.e. the Aquila earthquake leads to deformations that force the gap to open as shown in Figure 8.23(b).

8.7   Discussion

The design for gravity loads can be performed with a simple hand calculation or with the aid of software that is able to represent the non-linear moment-rotation behaviour of the post-tensioned timber connection using rotational springs.

The controlling design criterion is the stress in the column perpendicular to the grain. However, the tests under gravity loads lead to the conclusion that the joint can be loaded beyond the design value for the strength perpendicular to the grain without suffering from noticeable damage. Complying the requirements according to the standards lead to large cross sections of the beams in order to distribute the load over a larger area and therefore reduce the stresses. This usually leads to beam sizes that would allow the beams to carry the applied gravity loads as simply supported beams.

The seismic design for areas with low seismic hazard, such as Switzerland, is not problematic. Displacement limits under wind loads control the design process, especially if brittle elements have to be accounted for. It is therefore recommended to install non-structural elements that are able to follow the frame in its deformations, so that the deformation limits are less strict (H/200 instead of H/500). Moreover, it is advised to model the connection between the column and the foundation adequately so that its stiffness can be accounted for. Pinned connections are not suitable if the frame has to be designed for horizontal loads.

The frame is able to withstand larger earthquakes than the design earthquake for Zurich. The Patti earthquake described previously is much stronger than the design earthquake for Zurich and would lead to the moments that are plotted in Figure 8.24.

The maximum connection moment of 124 kNm would lead to an exceedance in stresses perpendicular to the grain in the column without taking the 38 kNm from the gravity loads into account (Figure 8.11). However, the pushover tests described in Chapter 5 showed that these moments can be handled by the system without suffering much damage. The moments for the pushover tests were calculated by using OpenSees and are shown in Figure 8.25(a) for a horizontal force of 250 kN and in Figure 8.25(b) for a horizontal force of 300 kN. The tests with a force of 250 kN lead to a maximal moment of 136 kNm which is smaller than the one from the Patti earthquake. An unloaded frame (i.e. a frame carrying only horizontal loads) would therefore be able to withstand the Patti shock without any damage. If the gravity load has to
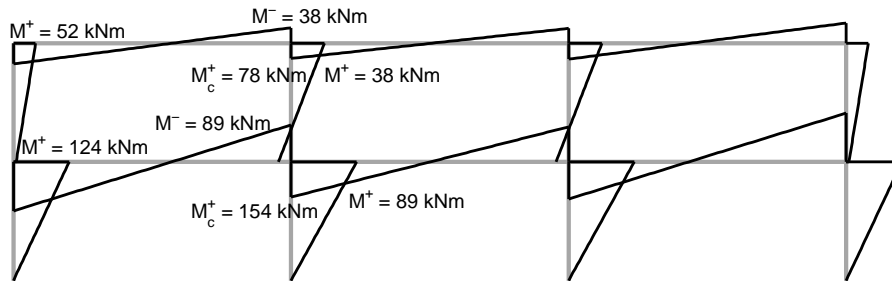
Figure 8.24: Moments due to Patti-earthquake

be accounted for, the maximum moment would add up to 162 kNm, which exceeds the moment obtained from the pushover tests by approximately 15%.

(a)

(b)
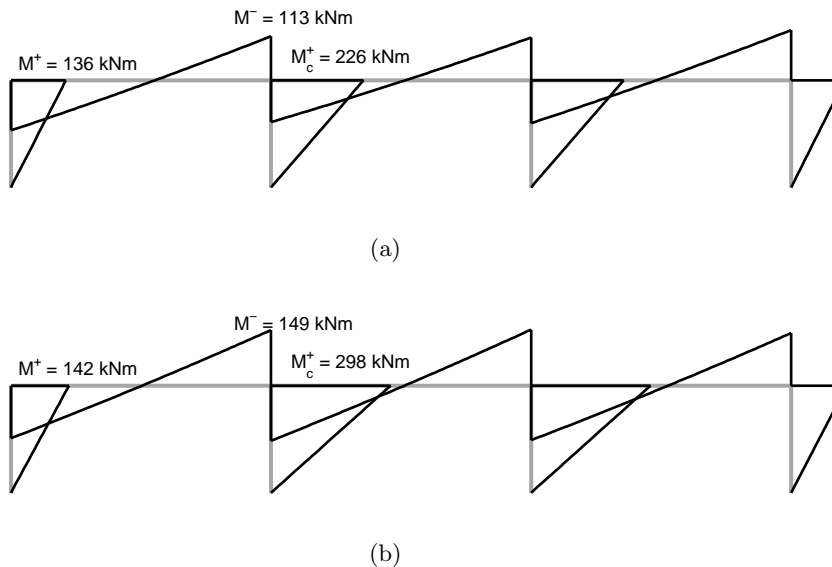
Figure 8.25: Calculated moments for the pushover-tests performed on a post-tensioned timber frame 8.25(a): For a horizontal force F = 250 kN 8.25(b): For a horizontal force F = 300 kN

The Aquila earthquake can not be handled by the frame, even if it is unloaded. The impact is too high as can be seen in Figure 8.23(b). A connection rotation of 0.015 rad has never been reached by any of the performed tests described herein (Chapter 4 and 5) and, therefore, needs to be considered unsafe.

Chapter 9

Conclusions

Analytical and numerical model

The analytical model is a simple tool which allows quantifying the structural behaviour of the proposed post-tensioned timber connection. The model is easy to understand for engineers since it is based on springs and can be solved by using the equilibrium of forces and moments. If the tendon elongation is taken into account, some iteration is required. Nevertheless, the analytical solution can easily be implemented in a Matlab code or an Excel spreadsheet especially if only gravity loads are considered. The model prediction was accurate for higher tendon forces (i.e. the initial compressive stresses due to pre-stressing was larger than 2 MPa) but showed a too soft behaviour for smaller tendon forces. Therefore, using the analytical model requires a certain tendon force in the system.

The input parameters for the model are all available in codes, since only the Young's modulus perpendicular to the grain is needed apart from the geometry of the joint. Good results were generated by using the following equation for the modulus of subgrade reaction:

$$c = \frac{2 \cdot E_{90}}{b_c}$$

The calculation in this document was based on a value of 860 MPa for the Young's modulus perpendicular to the grain. This value is - as mentioned in Chapter 3 - smaller than values found from tests. Since the model assumes rigid beams, taking a smaller value for the Young's modulus perpendicular to the grain indirectly takes into account that the system is softer than assumed by the model, since the beams are not rigid in reality.

The modulus of subgrade reaction influences the stiffness of the post-tensioned timber connection. If the value is large (i.e. by using a high value for the Young's modulus perpendicular to the grain) the stiffness increases. The parameter is however not very sensitive as can be seen in Figure 9.1, which shows different model predictions for different values of the Young's modulus perpendicular to the grain.

The influence on the design is small; a design rotation of 2 mrad would result in moments of 78 / 92 / 97 kNm for the three values of the Young's modulus perpendicular to the grain.
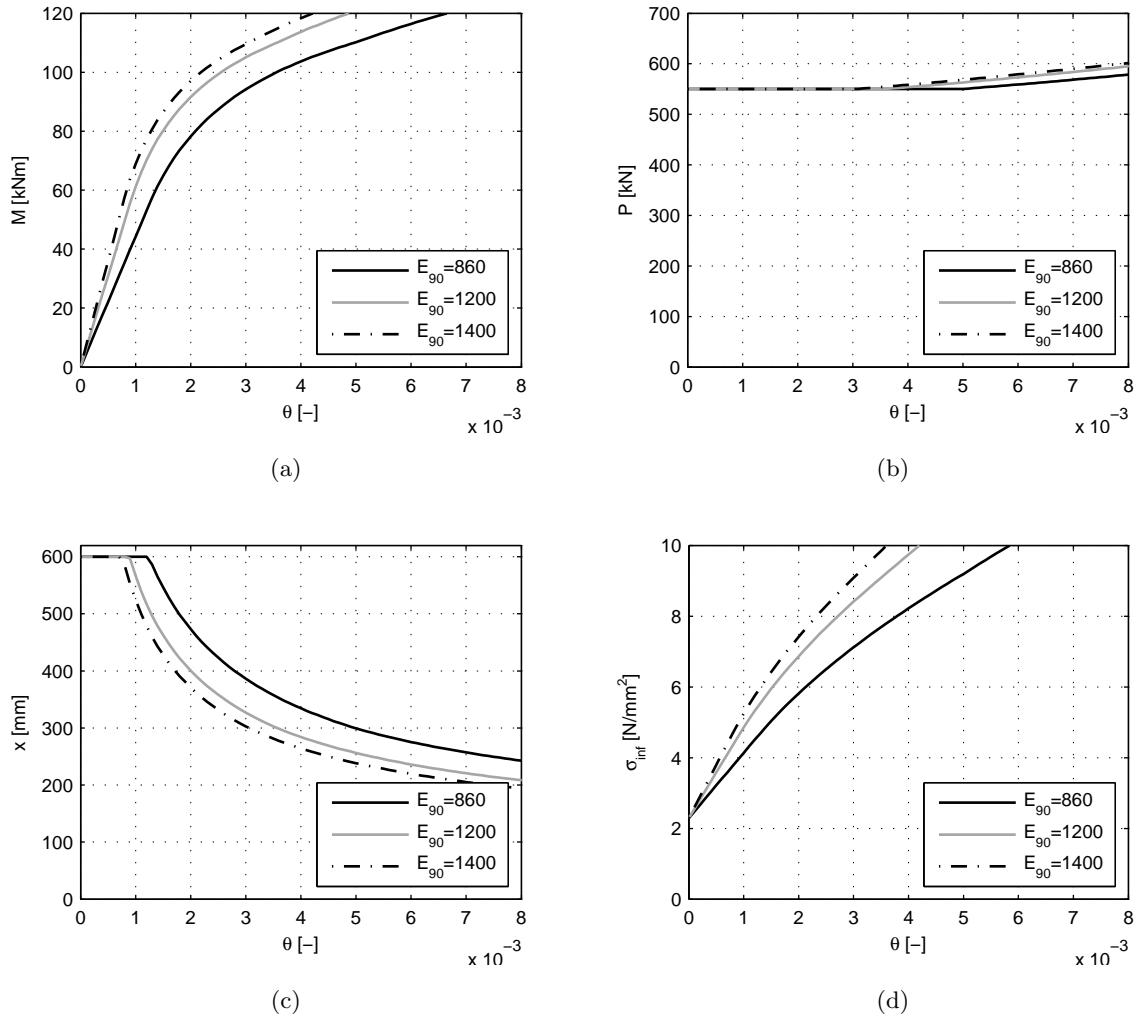
Figure 9.1: Analytical model based on different values for the Young's modulus perpendicular to the grain 9.1(a): Moment-rotation behaviour 9.1(b): Tendon force 9.1(c): Neutral axis depth 9.1(d): Stresses at the interface

Increasing the value from 860 MPa to 1200 Mpa (+40%) results in an increase in the moment from 78 to 92 kNm (+18%).

The influence on the pushover-curve is even smaller, as can be seen in Figure 9.2. An increase of the Young's modulus results only in minor changes of the pushover curve, which can easily be considered negligible.

The numerical model presented in Chapter 6 showed good results for all load cases investigated in the experimental campaign including the pushover tests. However, the orthotropic material properties in OpenSees require additional parameters which are difficult to estimate, such as the Poisson's ratio. Fortunately, this value is not critical since its influence on the pushover curve was shown to be small. The numerical model can also be used for smaller tendon forces (i.e. with initial compressive stresses due to pre-stressing smaller than 2 MPa).
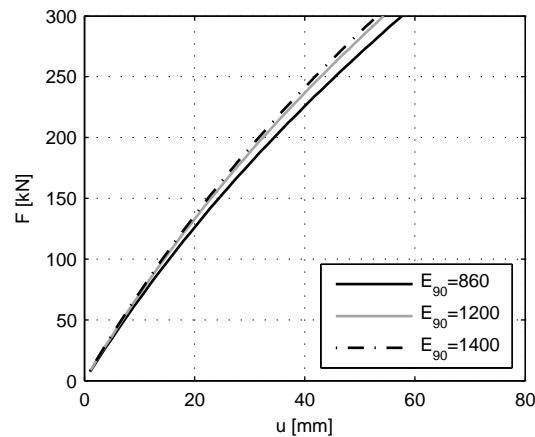
Figure 9.2: Pushover-curve generated with different values for the Young's modulus perpendicular to the grain

The combination of the analytical and numerical model creates a strong toolbox for practising engineers, providing two independent ways to design post-tensioned timber frames that are based solely on geometric properties and parameters which can be found in codes. A sensitivity analysis regarding the Young's modulus perpendicular to the grain is recommended for the analytical model for the gravity loads, especially if the entire design process is based on it.

Experimental campaign

The moment-rotation-behaviour of a post-tensioned beam-column timber joint has been analysed extensively with a series of static bending tests. The timber joint was loaded at the end of the beams in order to apply a moment to the connection. The tests were conducted with various forces in the tendon, from 300 kN up to 700 kN. The test showed that the connection stiffness increases with increasing tendon force and vice versa. Different load cases were considered for the tests; a series of tests was conducted with symmetrical loading, so that the column is only loaded in compression perpendicular to the grain. An asymmetrical load case was applied in order to load the column in compression and shear, leading to a significantly softer behaviour due to shear deformations in the column.
A final bending test was conducted in order to study the failure mode of the post-tensioned timber joint. The vertical load on the beams was increased until the tendon elongation got so high that the test had to be aborted for safety reasons. Therefore, an actual failure did not occur during the test. However, the estimated strength in the column perpendicular to the grain was exceeded at least by a factor of three but only minor damage could be observed after disassembling the specimen.
The performed tests showed that a very simple semi-rigid connection can be built with post-tensioning a timber specimen. Furthermore, the failure mode under gravity loads is not brittle but plastic. The timber fails due to embedment failure perpendicular to the grain, which only leads to very small damage in the connection as shown in Figure 9.3(a). The embedment failure

in the beam is hardly visible. However, a vertical displacement at the support is noticeable due to the large rotations of the beams during the tests. The overall damage of the system is very small though and has no consequences for the structural behaviour of the joint.

The pushover tests on the post-tensioned timber frame also showed a stiffness dependency on the tendon force as could also be observed during the test on the post-tensioned timber connection under gravity loads. The tests also showed a favourable behaviour under horizontal loading, i.e. a large deformation capacity, self centering behaviour and decreasing stiffness under increasing horizontal loading.

A failure test was not implied in the pushover-tests. Unfortunately a premature failure occurred in the tension zone of a column in a finger joint. The maximal applicable load was estimated before the test with 520 kN, whereas the failure already occurred at a load of 290 kN. The failure is shown in Figure 9.3(b), where the separated finger joints can be detected. Figure 9.3(b) also showns a large crack which already occurred before the test due to delamination. Several of these cracks could be observed during the test series. These cracks may be the result of the dry environment and the timber being used (European ash, *fraxinus excelsior*) [99].

(a)	(b)
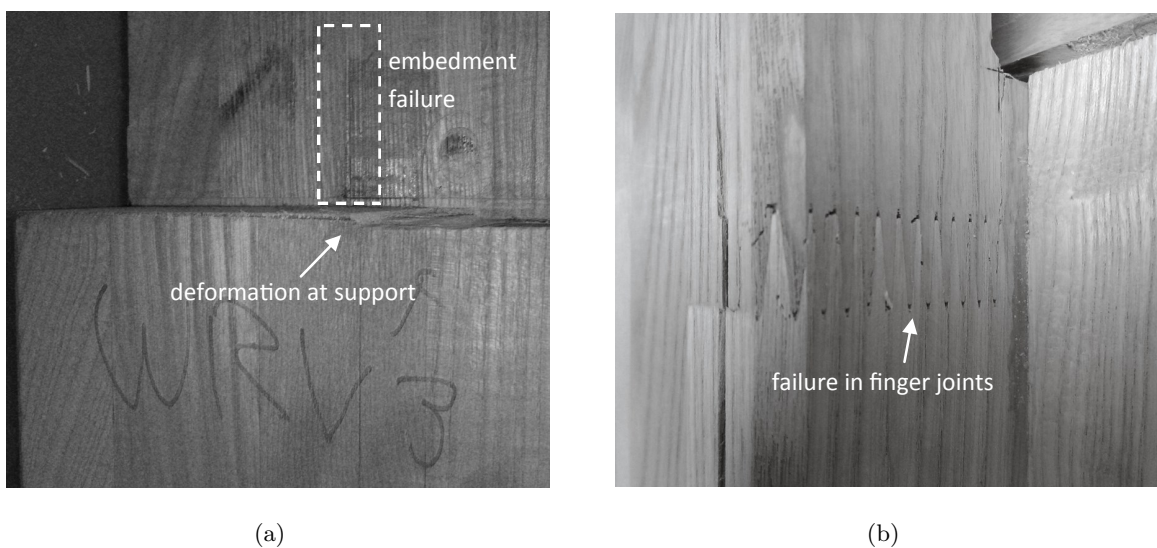
Figure 9.3: Damage occurred during the experimental campaign 9.3(a): Small deformation at the beam-column interface at the support under gravity loads 9.3(b): Premature failure at a finger-joint connection in the tensile zone of the column

Long-term behaviour

The tests on the scaled post-tensioned timber specimens indicated that more loss in tendon force has to be expected than for a pre-stressed structure made of concrete, where losses of 15% are usually accounted for. The extrapolated losses reach values of approximately 20%, whereas the losses also depend on the season. During periods with a low relative humidity more losses should

be accounted for than during periods with a high relative humidity. Based on the extrapolated data and the results obtained from the analytical model, a 30% loss in tendon force should be accounted for in the case of the proposed post-tensioned timber joint.

Since the relative humidity has a strong influence on the losses in tendon force, it is not recommended to use post-tensioned timber structures outdoors, i.e. the system should only be used for a service class 1 according the EN 1995 [100] or SIA 265 [60]. This recommendation also ensures that the tendon is protected from humidity and therefore from corrosion.

Since unbonded tendons are being used for the proposed connection, re-stressing the system is always possible if the design of the anchorage detail allows it. Moreover, the anchorage needs to be accessible in order to re-stress the system. This is important to consider when planning the details for the façade, for example.

Preliminary design

The design for gravity loads showed that the limitation of the system is given by the strength perpendicular to the grain in the column. The tests under gravity load lead to the conclusion that the joint can exceed the design limit without suffering from noticeable damage. Complying the requirements according to the standards leads to large cross sections of the beams in order to distribute the load over a larger area and therefore reduce the stresses.

If the design only has to account for gravity loads, the engineer may consider increasing the strength perpendicular to the grain in order to maintain a more economical structure. The stresses at the interface should not be higher than the ones estimated during the tests on the post-tensioned timber joint.

The design for the horizontal loads governs the size of the connection, whereas the wind loads are more critical than the seismic loads if the building is situated in an area with low seismicity (as Zurich). The deformation due to wind can be too large for brittle non-structural elements, even for buildings with only two storeys. The design should therefore not only focus on the structural elements. It is crucial that the non-structural elements are able to follow the deformations of the frame without suffering any damage. If this can be guaranteed, the drift limit may be increased and more storeys can be added to the structure.

Chapter 10

Outlook

The proposed post-tensioned timber frame showed that it is possible to construct a moment-resisting timber joint in a fast way. The system performed excellent under gravity loads, showing nearly no damage even if the loads were much higher than the design load. The performance under horizontal loading matched the prediction made with the analytical and numerical model equally well. However, the prototype design indicated that the design limits for the system is neither an earthquake nor the gravity loads. The controlling design criterion is the horizontal deformation under wind. The lateral stiffness of the system should therefore be increased. There are several possibilities to increase the stiffness:

- Change the material of the column

- Increase the connection stiffness

- Add structural elements

- Take the stiffness of the column base into account accurately

Changing the material of the column could result in a stiffer column (less elastic deformations of the column itself) if the Young's modulus perpendicular to the grain and the shear modulus are increased. It may be possible to change the material to beech LVL or even concrete, although the latter suggestion may not be accepted by the timber industry. Figure 10.1 shows pushover-curves for a single storey frame with modified connections or columns. The original model prediction was added as a reference (solid grey line). The pushover-curve for a frame made with LVL columns is plotted with the black dash dotted line. An increase in lateral stiffness is noticeable. However, the material will only improve the properties in one direction, i.e. a frame which is post-tensioned in two directions would have different stiffnesses in both direction. The material properties used for the calculations can be found on the website of the manufacturer [101].

Modifying solely the connection area may prove to be an economical sensible solution. The graphs in Figure 10.1 show that significant increase in lateral stiffness can be achieved by eliminating the shear deformation in the connection itself (black solid line). A reinforcement of

the connection area should therefore rather eliminate the shear deformations than increase the stiffness perpendicular to the grain.
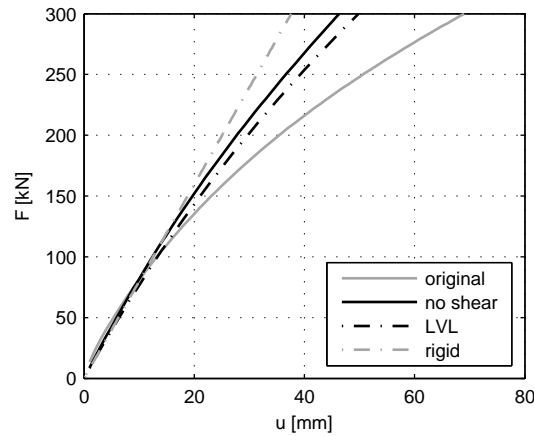
Figure 10.1: Pushover-curve generated for different systems

Adding steel elements to the connection could improve the connection behaviour. The steel elements have to reduce the shear deformations and will also increase the stiffness and strength of the column. A suggestion for such an element is presented in Figure 10.2.

(a)   (b)   (c)   (d)
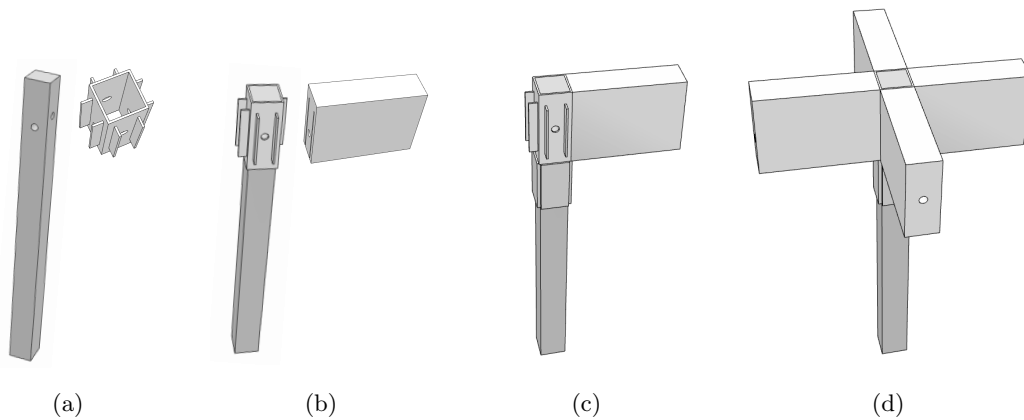
Figure 10.2: 10.2(a): Column and steel profile 10.2(b): Steel profile placed on column and adjacent beam 10.2(c): Supports attached under the beams 10.2(d): Connection with four beams attached to the column

Another solution to avoid too large deformations under wind load is to add additional structural elements. Since buildings often have a basement made of reinforced concrete, a concrete core may be added to the structure. The core would accommodate the staircase and elevator which also provides an escape way made of non-combustible material. The concrete core would be activated under horizontal loading whereas the post-tensioned timber frame would only be designed to carry the gravity loads (Figure 10.3). This would lead to a more slender structure, therefore reducing the costs in material and taking advantage of the favourable behaviour of the timber frame under gravity loads. A modified connection should be modelled numerically before being

tested under gravity loads and horizontal loads in order to estimate the structural behaviour. The analytical model may has to be altered, depending on the modification.
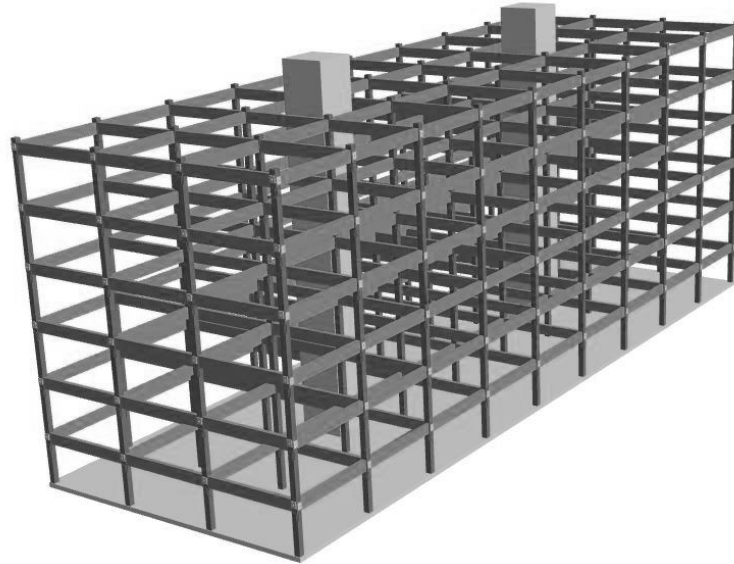
Figure 10.3: Fictitious building with post-tensioned timber frames for gravity loads and concrete cores for horizontal loads (slabs are not shown)

The pinned connections modelled at the bottom of the columns lead to a large horizontal displacement of the bottom story, which are controlling for the design (deformations under wind load). It is therefore necessary to estimate the actual stiffness of the connection at the bottom of the column. A stiffer column base would not only reduce the deformations due to wind but would also help to reduce the moments in the connections of the first storey. Tests on different kinds of connections are planned and will deliver the needed data.

By developing a modified system, two systems would be available for the market implementation; the herein presented system for areas with low seismic activity, as well as a new modified system for an area with higher seismic activity. The proposed systems should be implemented within the existing design codes, using a force based procedure. In order to capture the non-linear behaviour with a force based design method, a factor q representing ductility should be introduced. This factor is named "response factor" in SIA 261 [90] and "behaviour factor" in EN 1998 [102], and it enables an elastic linear analysis, while designing a structure for inelastic behaviour. The values for the q-factor for different structural systems are presented in the codes. However, newly developed systems, such as the proposed post-tensioned timber frame, are not adequately represented in this section of the codes.

The long-term tests will continue for at least another year in order to obtain more data regarding the losses in tendon force. In addition to the tests presented herein, another source of data will be available soon. A post-tensioned timber building - called the "ETH House of Natural Resources"- has recently been built. The building is used as an office building on the

ETH campus side but will also continuously serve for research purposes. The tendon force is measured with a load cell during the entire service life of the building, as shown in Figure 10.4.
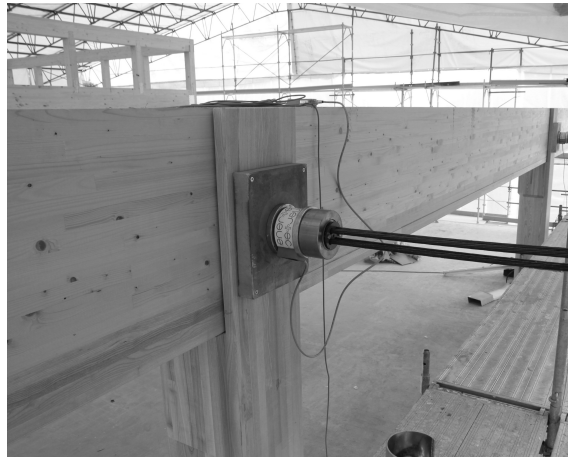
Figure 10.4: Anchorage for a tendon in the ETH House of Natural Resources with a load cell to measure the tendon force

More data will therefore be available soon for a fully sized specimen and for climatic conditions which will be representative for office spaces or apartment buildings.

Several dynamic tests with a shaker and an impulse hammer were performed during different construction phases of the building. The aim of this testing campaign is the estimation of the modal characteristics of the structure. The obtained modal data will help extending the knowledge on innovative hybrid timber structures and help predicting structural responses for the case of significant loads such as high wind loads or earthquakes, through an extended model element updating procedure.

Nomenclature

Upper-case roman letters

A	Area
A_b	Area cross section beam
A_c	Area cross section column
A_p	Area cross section tendon
$A_\parallel$	Area cross section loaded parallel to the grain
$A_\perp$	Area cross section loaded perpendicular to the grain
C	ratio of base shear normalised with the reactive weight
C^*	Strength coefficient
D	Diagonal distance shear panel
D'	Diagonal distance shear panel (deformed)
E	Young's modulus
E_b	Young's modulus beam
E_c	Young's modulus column
E_p	Young's modulus tendon
E_0	Young's modulus parallel to the grain
E_{90}	Young's modulus perpendicular to the grain
$E_\parallel$	Young's modulus parallel to the grain
$E_\perp$	Young's modulus perpendicular to the grain
F	Force
$F_{max,hor}$	Maximal horizontal force
G	Shear modulus
G_c	Shear modulus column
I	Moment of inertia

I_b	Moment of inertia beam
I_c	Moment of inertia column
K	Spring constant for rotational spring, stiffness matrix
K_i	Spring constant inner column
K_o	Spring constant outer column
$K_{hor,max}$	Maximal stiffness of a post-tensioned timber frame under horizontal load
$K_{I,left}$	Initial connection stiffness under gravity load (left interface)
$K_{I,max}$	Theoretical connection stiffness under gravity load
$K_{I,right}$	Initial connection stiffness under gravity load (right interface)
K_I	Initial connection stiffness under gravity load
K_{sys}	Combined stiffnesses of a beam-column specimen
K_{tot}	Total stiffness of all connections in a frame
L	Span of the frame
L_F	Distance interface-load application
L_p	Length tendon
M	Moment, mass matrix
M^+	Positive moment
M^-	Negative moment
M_c	Moment column
M_W	Magnitude
M_{dec}	Moment of decompression
$M_{max,i}$	Maximal moment for the inner column
$M_{max,o}$	Maximal moment for the outer column
M_{max}	Maximal moment
P	Tendon force
P_0	Initial tendon force
Q_w	Wind force
R	Resulting force
R_μ	Strength reduction factor
S_a	Acceleration of the design spectrum
S_d	Displacement of the design spectrum

T	Period
T_1	First natural period
V	Shear force
V_{base}	Base shear
W	Weight, reactive weight
W_b	Section modulus beam

Lower-case roman letters

a	Fitting parameter
a_0	Damping coefficient
a_1	Damping coefficient
a_{gd}	Ground acceleration
b	Fitting parameter
b_b	Width beam
b_c	Width column
c	Spring constant, modulus of subgrade reaction
c_{mod}	Modified spring constant, modified modulus of subgrade reaction
d	Position tendon
e	Eccentricity, mathematical constant, uniform vector
f	Eigenfrequency
f_1	First eigenfrequency
$f_{c,0,k}$	Compression strength parallel to the grain
$f_{c,0,mean}$	Compression strength parallel to the grain (mean value)
$f_{c,90,k}$	Compression strength perpendicular to the grain
$f_{c,90,mean}$	Compression strength perpendicular to the grain (mean value)
$f_{p,k}$	Tension strength tendon
f_P	Factor for activated stiffness
g	Acceleration due to gravity
g_k	Characteristic value of dead load
h_b	Height beam
h_c	Height column

k^*	Effective stiffness (effective modal SDOF sytem)
k_i	Lateral stiffness of the storey i
l	Total length of the beam-column specimen
$l_\parallel$	Length loaded parallel to the grain
$l_\perp$	Length loaded perpendicular to the grain
m^*	Effective modal mass
m_i	Mass of the storey i
n	Ratio between elastic modulus of timber parallel to the grain to perpendicular to the grain
q	Distributed load, response factor
q'_{Ed}	Design value of a uniformly distributed load
q_k	Characteristic value of live load
q_{Ed}	Design value of distributed load
$q_{k,s}$	Characteristic value of snow load
$q_{k,w}$	Characteristic value of wind load
r	Position resulting force
r_p	relaxation coefficient tendon
t	Time
u	Displacement
u_0	Initial displacement
w	Deflection, settlement
$w_{\dots}$	Displacement measured at the beam-column interface
$w_{comp,left}$	Initial compression at the left interface
$w_{comp,right}$	Initial compression at the right interface
w_{inf}	Displacement at the lower edge of the interface
x	Neutral axis depth

Upper-case greek letters

$\Delta L_{in,beam}(t)$	Variation of environmental deformations in the beam
$\Delta L_{in,column}(t)$	Variation of environmental deformations in the column
ΔL_p	Tendon elongation

ΔP	Increase in tendon force
$\Delta P(t)$	Loss in tendon force at time step t
Δ	Load distribution factor, roof displacement
$\Delta*$	Roof displacement (effective modal SDOF sytem)
$\Delta\varepsilon_{\parallel,in}(t)$	Variation of environmental strains over time parallel to the grain
$\Delta\varepsilon_{\perp,in}(t)$	Variation of environmental strains over time perpendicular to the grain
$\Delta\varepsilon_{p,in}(t)$	Variation of environmental strains over time tendon
Γ_1	Modal participation factor

Lower-case greek letters

α	Ratio between axial stiffness of timber parallel to grain and tendon
α_1	Mass participation factor
$\chi_{\parallel}(t)$	Ageing coefficient parallel to the grain
$\chi_{\perp}(t)$	Ageing coefficient perpendicular to the grain
$\chi_p(t)$	Ageing coefficient tendon
γ	Shear angle
γ_G	Load factor for permanent action
γ_Q	Load factor for variable action
κ	Spring constant for the beam-column interface under gravity load
λ	ratio $l_{\perp}$ to $(l_{perp}+l_{\parallel})$
μ	Ratio between cross-section area loaded perpendicular to the grain and parallel to the grain
ν	Poisson's ratio
ω	Angular eigenfrequency
ω_1	First angular eigenfrequency
ω_2	Second angular eigenfrequency
ω_n	Natural angular frequency
ϕ	Creep coefficient
ϕ_1	First eigenvector
$\phi_{\parallel}$	Creep coefficient parallel to the grain
$\phi_{\perp}$	Creep coefficient perpendicular to the grain

ψ_2	Reduction factor for quasi-permanent value of variable action
ρ	Damping coefficient, beam-to-column stiffness ratio
σ	Stresses, applied stress level
σ_0	Initial stresses due to pre-stressing
σ_m	Average stresses
σ_{inf}	Stresses at bottom of the interface
σ_{sup}	Stresses at top of the interface
θ	Rotation due to moment in the connection
$\theta_{col,el}$	Elastic rotation of the column
θ_{GA}	Rotation due to shear deformation
$\theta_{M=1kNm}$	Rotation at a moment of 1 kNm
θ_{max}	Allowable rotation based on column strength perpendicular to the grain
θ_{tot}	Total rotation in the beam-column interface
ζ	Damping ratio

Bibliography

[1]   M. Dehne and D. Kruse, "Brandschutz bei mehrgeschossigen Holzbauten–Praxiserfahrung und neue Entwicklungen [Fire protection in multi-storey timber buildings - practical experience and new developments]", *Bauingenieur*, vol. 81, p. 142, 2006.

[2]   D. Hopkin, J. El-Rimawi, V. Silberschmidt, and T. Lennon, "An effective thermal property framework for softwood in parametric design fires: Comparison of the eurocode 5 parametric charring approach and advanced calculation models", *Construction and Building Materials*, vol. 25, pp. 2584 –2595, 2011.

[3]   Vereinigung Kantonaler Feuerversicherungen. (2003). Brandschutznorm [fire safety standard]. German, Vereinigung Kantonaler Feuerversicherungen (VKF), [Online]. Available: `http://www.vkf.ch`.

[4]   G. P. Peters, R. M. Andrew, T. Boden, J. G. Canadell, P. Ciais, C. Le Quéré, G. Marland, M. R. Raupach, and C. Wilson, "The challenge to keep global warming below 2℃", *Nature Climate Change*, vol. 3, pp. 4–6, 2013.

[5]   L. Gustavsson, K. Pingoud, and R. Sathre, "Carbon dioxide balance of wood substitution: Comparing concrete- and wood-framed buildings", *Mitigation and adaptation strategies for global change*, vol. 11, pp. 667–691, 2006.

[6]   F. Lam, M. Gehloff, and M. Closen, "Moment-resisting bolted timber connections", *Proceedings of the ICE-Structures and Buildings*, vol. 163, pp. 267–274, 2010.

[7]   J. Kolb, *Systems in timber engineering: Loadbearing structures and component layers*, Lignum - Holzwirtschaft Schweiz, DGfH - German Society of Wood Research, Ed. Walter de Gruyter, 2008.

[8]   A. Buchanan, B. Deam, M. Fragiacomo, S. Pampanin, and A. Palermo, "Multi-storey prestressed timber buildings in New Zealand", *Structural Engineering International*, vol. 18, pp. 166–173, 2008.

[9]   R. Schneider, "Tragverhalten von vorgespannten Holzkonstruktionen [Structural behaviour of post-tensioned timber structures]", Master's thesis, ETH Zürich, 2010.

[10] G. Lantos, "Reinforced and post-tensioned glue laminated beams under development at TRADA laboratories", *Civil Engineering (London)*, vol. 59, pp. 86–87, 1964.

[11] J. Peterson, "Wood beams prestressed with bonded tension elements", *Journal of the Structural Division*, vol. 91, pp. 103–119, 1965.

[12] T. C. Triantafillou and N. Deskovic, "Prestressed FRP sheets as external reinforcement of wood members", *Journal of Structural Engineering*, vol. 118, pp. 1270–1284, 1992.

[13] J. F. Brady, A. M. Harte, and T Arima, "Prestressed FRP flexural strengthening of softwood glue-laminated timber beams", *Proceedings of the 10th World Conference on Timber Engineering WCTE, Miyazak, Japan*, 2008.

[14] G. M. Raftery and A. M. Harte, "Low-grade glued laminated timber reinforced with FRP plate", *Composites Part B: Engineering*, vol. 42, pp. 724–735, 2011.

[15] M. A. Ritter, E. A. Geske, L. Mason, W. J. McCutcheon, R. C. Moody, and J. Wacker, "Performance of stress-laminated bridges", *Wood Design Focus*, vol. 1, pp. 12–16, 1990.

[16] M. C. Oliva, A. G. Dimakis, M. Ritter, R Taylor, R. Taylor, M Ritter, K. Crews, S. Bakoss, T. R. Gentry, K. N. Brohammer, *et al.*, "Development and use of stress laminated timber deck bridges", *Proceedings of the sessions at Structures Congress 1987 related to bridges and transmission line structures; 1987 August 17-20; Orlando, Fl. New York: American Society of Civil Engineers*, 1987.

[17] M. Oliva and A. Dimakis, "Behavior of stress-laminated timber highway bridge", *Journal of Structural Engineering*, vol. 114, pp. 1850–1869, 1988.

[18] B. L. Deam, M. Fragiacomo, and L. S. Gross, "Experimental behavior of prestressed LVL-concrete composite beams", *Journal of Structural Engineering*, vol. 134, pp. 801–809, 2008.

[19] M. N. Priestley, "Overview of PRESSS research program", *PCI Journal*, vol. 36, pp. 50–57, 1991.

[20] ——, "The PRESSS Program-Current Status and Proposed Plans for Phase III", *PCI Journal*, vol. 41, pp. 22–40, 1996.

[21] S. Pampanin, M. N. Priestley, and S Sritharan, "Analytical modelling of the seismic behaviour of precast concrete frames designed with ductile connections", *Journal of Earthquake Engineering*, vol. 5, pp. 329–367, 2001.

[22] S. Pampanin, "Alternative design philosophies and seismic response of precast concrete buldings", PhD thesis, Technical University of Milan, 2000.

[23] A. Palermo, S. Pampanin, and G. M. Calvi, "The use of controlled rocking in the seismic design of bridges", *Proceedings of the 8th World Conference on Timber Engineering WCTE, Lahti, Finland*, 2004.

[24] A. Palermo, S. Pampanin, A. Buchanan, and M. Newcombe, "Seismic design of multistorey buildings using laminated veneer lumber (lvl)", *Proceedings of the 2005 NZSEE Conference, Taupo, New Zealand*, 2005.

[25] A. Palermo, S. Pampanin, and A. Buchanan, "Experimental investigations on lvl seismic resistant wall and frame subassemblies", *Proceedings of the 1st First European Conference on Earthquake Engineering and Seismology, Geneva, Switzerland*, University of Canterbury. Civil Engineering., 2006.

[26] A. Palermo, S Pampanin, M Fragiacomo, A. Buchanan, and B. Deam, "Innovative seismic solutions for multi-storey lvl timber buildings", *Proceedings of the 9th World Conference on Timber Engineering WCTE, Portland, OR, USA*, 2006.

[27] M. Newcombe, S Pampanin, A Buchanan, and A Palermo, "Section analysis and cyclic behavior of post-tensioned jointed ductile connections for multi-story timber buildings", *Journal of Earthquake Engineering*, vol. 12, pp. 83–110, 2008.

[28] ——, "Seismic design of multistorey post-tensioned timber buildings", PhD thesis, Masters Thesis, University of Pavia, Pavia, 2008.

[29] A. Iqbal, S. Pampanin, and A. Buchanan, "Seismic performance of prestressed timber beam-column sub-assemblies", *Proceedings of the New Zealand Society for Eearthquake Engineering Conference, Wellington, New Zealand*, 2010.

[30] M. Newcombe, S Pampanin, and A. Buchanan, "Global response of a two storey pres-lam timber building", *Proceedings of the New Zealand Society for Eearthquake Engineering Conference, Wellington, New Zealand*, 2010.

[31] A. Buchanan, A. Palermo, D. Carradine, and S. Pampanin, "Post-tensioned timber frame buildings", *Structural Engineer*, vol. 89, pp. 24–30, 2011.

[32] W. van Beerschoten, A. Palermo, D. Carradine, F. Sarti, and A. Buchanan, "Experimental investigation on the stiffness of beam-column connections in post-tensioned timber frames", *Proceedings of the Structural Engineering World Conference, Como, Italy*, 2011.

[33] T. Smith, S. Pampanin, D. Carradine, A. Buchanan, F. Ponzo, A Cesare, and D. Nigro, "Experimental investigations into post-tensioned timber frames with advanced damping systems", *Proceedings of Il XIV Convegno di Ingegneria Sismica, Associazione Nazionale di Ingegneria Sismica, Bari, Italy*, 2011.

[34] T. Smith, M. Fragiacomo, S. Pampanin, and A. H. Buchanan, "Construction time and cost for post-tensioned timber buildings", *Proceedings of the ICE-Construction Materials*, vol. 162, pp. 141–149, 2009.

[35] S. Pampanin, A. Palermo, A. Buchanan, M. Fragiacomo, and B. Deam, "Code provisions for seismic design of multi-storey post-tensioned timber buildings", *Proceedings of the CIB W18 Workshop on Timber Structures, Florence, Italy*, 2006.

[36] M. Newcombe, M. Cusiel, S Pampanin, A Palermo, and A. Buchanan, "Simplified design of post-tensioned timber frames", *Proceedings of theCIB W18 Workshop on Timber Structures, Nelson, New Zealand*, 2010.

[37] D. Moroder, A. Buchanan, and S. Pampanin, "Preventing seismic damage to floors in post-tensioned timber frame buildings", *Proceedings of the 2013 NZSEE Conference, Wellington, New Zealand*, 2013.

[38] D. Moroder, F. Sarti, A. Palermo, S. Pampanin, and A. Buchanan, "Experimental investigation of wall-to-floor connections in post-tensioned timber buildings", *Proceedings of the 2014 NZSEE Conference, Auckland, New Zealand*, 2014.

[39] W. van Beerschoten, A. Palermo, D. Carradine, and A. Buchanan, "Failure criteria for post-tensioned timber beams", *Conference note presented at the CIB W18 Workshop on Timber Structures, Vaxjo, Sweden*, 2012.

[40] W. van Beerschoten, "Structural performance of post-tensioned timber frames under gravity loading", PhD thesis, University of Canterbury, 2013.

[41] W. van Beerschoten, A. Palermo, and D. Carradine, "Gravity design of post-tensioned timber frames for multi-storey buildings", *Proceedings of the 43rd ASCE/SEI Structures Congress, Chicago, IL, USA.*, 2014.

[42] E. F. Sarisley Jr and M. L. Accorsi, "Prestress level in stress-laminated timber bridges", *Journal of Structural Engineering*, vol. 116, pp. 3003–3019, 1990.

[43] P. Quenneville and K. Van Dalen, "Parameters affecting stress losses in stress-laminated timber bridge decks", *Proceedings of the International Wood Engineering Conference, New Orleans, LA, USA*, 1996.

[44] D. Bond and E. Sidwell, "Prestressed timber beams", *Civil Engineering (London)*, vol. 60, pp. 547–550, 1965.

[45] M. Davies and M. Fragiacomo, "Long-term behavior of prestressed LVL members. I: Experimental tests", *Journal of Structural Engineering*, vol. 137, pp. 1553–1561, 2011.

[46] M. Fragiacomo and M. Davies, "Long-term behavior of prestressed LVL members. II: Analytical approach", *Journal of Structural Engineering*, vol. 137, pp. 1562–1572, 2011.

[47] D. Steiner and S. Pirker, *Architecture in Austria: A Survey of the 20th Century*, A. Z. W. Sasha Pirker, Ed. Springer Science & Business Media, 1999.

[48] J. Conzett, M. Mostafavi, and B. Reichlin, *Structure as space: Engineering and architecture in the works of Jürg Conzett and his partners*, M. Mostafavi, Ed. AA publications, 2006.

[49] M. Meili and M. Peter. (2014). Marcel meili, markus peter, architects zürich. English and German, Marcel Meili, Markus Petrer Architekten Zürich, [Online]. Available: `www.meilipeter.ch`.

[50] O. Kapfinger, *Zuschnitt: Zeitschrift über Holz als Werkstoff und Werke in Holz [Magazine about wood and wooden products]*, Austria, Arbeitsgemeinschaft der Österreichischen Holzwirtschaft ProHolz, Ed., 7. ProHolz Austria, 2002.

[51] C. Devereux, T. Holden, A. Buchanan, and S. Pampanin, "NMIT Arts & Media Building-damage mitigation using post-tensioned timber walls", *Proceedings of the Ninth Pacific Conference on Earthquake Engineering, Auckland, New Zealand*, 2011.

[52] B. Curtain, D. Dekker, S. Chung, and A. Palermo, "Design of Carterton Event Centre: An example of innovative collaboration between architecture and timber engineering", *Proceedings of the 12th World Conference on Timber Engineering WCTE, Auckland, New Zealand*, 2012.

[53]   F. Sarti, A. Palermo, and S. Pampanin, "Simplified design procedures for post-tensioned seismic resistant timber walls", *Proceedings of the 15th World Conference on Earthquake Engineering, Lisbon, Portugal*, 2012.

[54]   J. Harvey, *Creative Arts Building - Te Ara Hihiko*, A. N. Zealand, Ed. agm publishing, 2012, vol. 4.

[55]   J. McGar. (2014). Post-tensioned timber buildings beat earthquakes. English, Sourceable Industry News & Analysis, [Online]. Available: `http://sourceable.net/post-tensioned-timber-buildings-beat-earthquakes/`.

[56]   C. Chapman. (2014). Strength redefined. English, Architecutrenow, [Online]. Available: `http://architecturenow.co.nz/articles/strength-redefined/`.

[57]   H.-J. Lang, J. Huder, and P. Amann, *Bodenmechanik und Grundbau: das Verhalten von Böden und Fels und die wichtigsten grundbaulichen Konzepte [Soil mechanics and geotechnical engineering: the behaviour of soil and rock and the most important geotechnical concepts]*. Springer, 2003.

[58]   E. Winkler, "Die Lehre von der Elastizität und Festigkeit [The method of elasticity and strength]", *Prague: H. Dominicus*, vol. 141, pp. 182–184, 1867.

[59]   D. Fischer, "Interaktion zwischen Baugrund und Bauwerk [Soil-structure interaction]", PhD thesis, Universität Kassel, 2009.

[60]   Swiss Standards Association, "SIA 265 - timber structures", *Swiss Society of Engineers and Architects, Zurich, Switzerland*, 2003.

[61]   neue Holzbau AG. (2014). Glulam hardwood. English, neue Holzbau AG, [Online]. Available: `www.neueholzbau.ch/en/produkte/laubholz/`.

[62]   European Committee for Standardization (CEN), "EN 338 - structural timber - strength classes; german version", *DIN Deutsches Institut für Normung e. V., Berlin, Germany*, 2009.

[63]   U. Hübner, "Laubhölzer für lastabtragende Bauteile im Bauwesen [Hardwoods for load-bearing elements in construction]", *OIB aktuell*, vol. 10, pp. 12–23, 2009.

[64]   F. Wanninger and A. Frangi, "Experimental analysis of a post-tensioned timber connection", *Materials and Joints in Timber Structures*, Springer, 2014, pp. 57–66.

[65]   F. Wanninger and A. Frangi, "Experimental and analytical analysis of a post-tensioned timber connection under gravity loads", *Engineering Structures*, vol. 70, pp. 117–129, 2014.

[66]   R. Steiger and M. Arnold, "Strength grading of Norway spruce structural timber: revisiting property relationships used in EN 338 classification system", *Wood science and technology*, vol. 43, pp. 259–278, 2009.

[67]   F. Wanninger, A. Frangi, and R. Steiger, "Bearing stiffness in wood-to-wood compression joints", *Engineering Structures*, vol. 101, pp. 631–640, 2015.

[68] H. J. Blass and R. Görlacher, "Compression perpendicular to the grain", *Proceedings of the 8th World Conference on Timber Engineering WCTE, Lahti, Finland*, 2004.

[69] F. Wanninger and A. Frangi, "Investigation of a post-tensioned timber connection - test report", Institute of Structural Engineering - Timber Structures, Tech. Rep., 2014.

[70] Stahlton AG. (2012). Vorspanntechnik [post-tensioning technolgy]. German, Stahlton AG, [Online]. Available: `http://www.stahlton.ch`.

[71] JCSS, *Probabilistic Model Code - Part III*. Joint Committee on Structural Safety, 2006.

[72] L. Boccadoro and A. Frangi, "Experimental analysis on the structural behavior of timber-concrete composite slabs made of beech-laminated veneer lumber", *Journal of Performance of Constructed Facilities*, vol. 28, 2013.

[73] C. Leyder, F. Wanninger, A. Frangi, and E. Chatzi, "Field testing on innovative timber structures", *Proceedings of the 13th World Conference on Timber Engineering WCTE, Quebec City, Canada*, 2014.

[74] A. K. Chopra, *Dynamics of structures: Theory and applications to earthquake engineering*. Pearson Prentice-Hall, 2007.

[75] K.-M. Chang, "Arrhythmia ecg noise reduction by ensemble empirical mode decomposition", *Sensors*, vol. 10, pp. 6063–6080, 2010.

[76] A. K. Chopra and R. K. Goel, "A modal pushover analysis procedure for estimating seismic demands for buildings", *Earthquake Engineering & Structural Dynamics*, vol. 31, pp. 561–582, 2002.

[77] C. Leyder, F. Wanninger, A. Frangi, and E. Chatzi, "Dynamic response of an innovative hybrid structure in hardwood", *ICE - Construction Materials*, vol. 168, pp. 132–143, 2015.

[78] F. McKenna, S. Mazzoni, and G. Fenves, "Open System for Earthquake Engineering Simulation (OpenSees) Software Version 2.3.0", *University of California, Berkeley, CA. Available from http://opensees. berkeley. edu*, 2011.

[79] D. W. Green, J. E. Winandy, D. E. Kretschmann, *et al.*, "Mechanical properties of wood", *Wood Handbook*, Forest Products Laboratory, U.S. Department of Agriculture, 1999.

[80] F. Wanninger, A. Frangi, and M. Fragiacomo, "Long-term behavior of posttensioned timber connections", *Journal of Structural Engineering*, vol. 141, 2015.

[81] F. Wanninger and A. Frangi, "Post-tensioned timber connections, experimental analysis of the long term behaviour", *Proceedings of the 13th World Conference on Timber Engineering WCTE, Quebec City, Canada*, 2014.

[82] Swiss Standards Association, "SIA 260 - basis of structural design", *Swiss Society of Engineers and Architects, Zurich, Switzerland*, 2003.

[83] EMPA. (2014). Schweizerische Technische Zulassung STA - 01/010 [Swiss technical cetification STA - 01/010]. German, Stahlton AG, [Online]. Available: `http://www.stahlton-bautechnik.ch/web/images/stories/zulassungen/`.

[84] European Committee for Standardization (CEN), "EN 789 - Holzbauwerke - Prüfverfahren - Bestimmung der Mechanischen Eigenschaften von Holzwerkstoffen ; German version", *DIN Deutsches Institut für Normung e. V., Berlin, Germany*, 2004.

[85] S. Svensson and T. Toratti, "Mechanical response of wood perpendicular to grain when subjected to changes of humidity", *Wood Science and Technology*, vol. 36, pp. 145–156, 2002.

[86] JCSS Probabilistic Model, "The joint committee on structural safety", 2001. [Online]. Available: `www.jcss.ethz.ch`.

[87] Swiss Standards Association, "SIA 262 - concrete structures", *Swiss Society of Engineers and Architects, Zurich, Switzerland*, 2003.

[88] M. Fragiacomo and M. Batchelar, "Timber frame moment joints with glued-in steel rods. II: Experimental investigation of long-term performance", *Journal of Structural Engineering*, vol. 138, pp. 802–811, 2011.

[89] ETH Zurich. (2015). Eth house of natural resources. German and English, ETH Zurich, [Online]. Available: `http://www.honr.ethz.ch`.

[90] Swiss Standards Association, "SIA 261 - actions on structures", *Swiss Society of Engineers and Architects, Zurich, Switzerland*, 2003.

[91] F. McKenna, "Opensees: A framework for earthquake engineering simulation", *Computing in Science & Engineering*, vol. 13, pp. 58–66, 2011.

[92] D. Giardini, J. Woessner, L. Danciu, H. Crowley, F. Cotton, G. Grünthal, R. Pinho, G. Valensise, S. Akkar, R. Arvidsson, *et al.*, *Seismic hazard harmonization in europe (share). online data resource*, 2013.

[93] M. Priestley, "Performance based seismic design", *Bulletin of the New Zealand Society for Earthquake Engineering*, vol. 33, no. 3, pp. 325–346, 2000.

[94] A. K. Chopra and R. K. Goel, "Capacity-demand-diagram methods based on inelastic design spectrum", *Earthquake spectra*, vol. 15, pp. 637–656, 1999.

[95] P. Fajfar, "Capacity spectrum method based on inelastic demand spectra", *Earthquake Engineering & Structural Dynamics*, vol. 28, pp. 979–993, 1999.

[96] L. Eads. (2010). Dynamic analysis of 2-story moment frame. Englisch, Stanford University, [Online]. Available: `http://opensees.berkeley.edu/wiki/index.php/Dynamic_Analysis_of_2-Story_Moment_Frame`.

[97] L. Luzi, S. Hailemikael, D. Bindi, F. Pacor, F. Mele, and F. Sabetta, "ITACA (Italian Accelerometric Archive): A web portal for the dissemination of italian strong-motion data", *Seismological Research Letters*, vol. 79, pp. 716–722, 2008.

[98] F. Pacor, R. Paolucci, L. Luzi, F. Sabetta, A. Spinelli, A. Gorini, M. Nicoletti, S. Marcucci, L. Filippi, and M. Dolce, "Overview of the italian strong motion database ITACA 1.0", *Bulletin of Earthquake Engineering*, vol. 9, pp. 1723–1739, 2011.

[99] M. Knorz, M. Schmidt, S. Torno, and J.-W. van de Kuilen, "Structural bonding of ash (fraxinus excelsior l.): Resistance to delamination and performance in shearing tests", *European Journal of Wood and Wood Products*, vol. 72, pp. 297–309, 2014.

[100] European Committee for Standardization (CEN), "Eurocode 5 - design of timber structures - part 1-1: General-common rules and rules for buildings", *PrEN 1995-1-1. Bruxelles, Belgium*, 2010.

[101] Pollmeier. (2015). Ingenious hardwood baubuche information. English, Pollmeier, [Online]. Available: `www.pollmeier.com`.

[102] European Committee for Standardization (CEN), "Eurocode 8–design of structures for earthquake resistance–part 1: General rules, seismic actions and rules for buildings", *European Standard NF EN*, vol. 1, 1998.